UNIVERSITÀ DEGLI STUDI DI PADOVA

DIPARTIMENTO DI INGEGNERIA INDUSTRIALE

CORSO DI LAUREA MAGISTRALE IN CHEMICAL AND PROCESS ENGINEERING

Tesi di Laurea Magistrale in Chemical and Process Engineering

ACCELERATING PHARMACEUTICAL TABLET DEVELOPMENT BY TRANSFER OF COMPACTION EQUIPMENT ACROSS TYPES AND SCALES

Relatore: Prof. Massimiliano Barolo
Correlatore: Dr. Marv Khala

Laureando: LUCA BECCARO

ANNO ACCADEMICO 2022 – 2023

Abstract

Roller compaction is a key unit operation in a dry granulation line for pharmaceutical tablet manufacturing. However, determining the optimal settings for a roller compactor (RC) typically requires extensive material-consuming experimental campaigns. This amount of material, in particular if active pharmaceutical ingredients are involved, may not be available during development phases, or may be very expensive. For this reason, a compactor simulator (CS) is usually employed to emulate the behaviour of compacted powders at a much smaller scale, with significant savings of materials, time, and money. However, the experimental conditions at which a CS shall be run to obtain a product with assigned specifications are different from those required to obtain the same product from a full-scale RC. How to find these conditions is an open issue. In this study, historical data from both CS and RC experiments are used to develop a transfer methodology that allows the experimenter to obtain optimal RC setup from the CS experimental results solely. The developed correlation, which has been applied to six different pharmaceutical powder blends, successfully captures the differences between the two equipment scales. Implementing this transfer methodology can result in reliable prediction of RC machine settings, thus enabling significant resource, time and money savings.

This thesis is the result of a collaboration between the Process Engineering & Analytics team of GSK (Stevenage; UK) and the CAPE-Lab group at the University of Padua.

Table of Contents

Introduction

Roller compaction is a dry granulation process used to densify and enhance physical and flowability properties of pharmaceutical powder blends in the manufacturing of tablets. It is a continuous process that involves feeding powder through a pair of counter-rotating rollers, which compact it into a solid mass known as ribbon by exerting pressure. To better understand the phenomena that occur during the compaction process, Johanson (1965) developed a powder mechanics model that predicted the roll surface pressure and the ribbon solid fraction based on the physical properties of the powdered material, the operating conditions and the roller compactor (RC) geometry. To utilize the Johanson model, which presents two material-dependent parameters, it is required a calibration of the latter by performing a parameter estimation employing RC experimental results of a specific powder blend. However, performing a comprehensive experimental campaign on the RC demands significant amounts of material, including very expensive active pharmaceutical ingredients (APIs), which may not be available during the drug development phases. In this context, compaction simulators (CSs) have been developed, which mimic the roll compaction process by performing uniaxial compaction through two counter-moving punches. By employing a CS, it became possible to quantify the compaction behaviour of a specific powder blend through more resource-efficient experimental campaigns, involving material amounts on the order of grams compared to the kilograms required for the RC testing. However, the results obtained from the CS are not suitable for accurately estimating the Johanson model parameters specific to a powder mixture, owing to differences in the applied pressure for equivalent solid fraction values. In this context, Bi et al., (2014) introduced the mass correction factor theory, which improves Johanson model's one-dimensional compaction assumption by providing a correction factor that allows to account and link the different RC and CS pressures.

The objective of this Thesis is to assess the experimental results derived from both RC and CS pieces of equipment, investigating their differences across six various pharmaceutical powder blends. Following that, the analysis proceeds by developing a methodology, based on the mass correction factor theory, capable of explaining and establishing a relationship between the different CS and RC outcomes. The result, the proposed methodology allows for the characterization of the roller compaction behaviour for a specific powder blend solely by means of an experimental campaign on the CS, leading to substantial savings in terms of material, resources, and time and money.

The Thesis is structured into four chapters. The Chapter 1 introduces roll compaction, describing its operational applications and advantages in the pharmaceutical industry. The compaction simulator is examined next, explaining how this technology was developed to mimic RC.

The Chapter 2 presents the Johanson model, detailing its assumptions and benefits, as well as the physical and mathematical principles. After that, the mass correction factor theory proposed by Bi et al., (2014) is presented.

All materials investigated in this Thesis are presented in Chapter 3. The descriptions of all experimental campaigns conducted on both RC and CS and the related datasets follow. The mathematical methods utilised to carry out the parameter estimate for the Johanson model are next discussed. Finally, the proposed transfer methodology to establish the relationship between CS and RC pressures is described, presenting the development stage, with the calibration and validation procedures, and then the usage stage.

In Chapter 4, the results obtained by estimating the Johanson parameters for each powder mixture are first presented. After that, the results of the experiments derived from the two distinct pieces of equipment are compared, and an analysis of how the mass correction factor can be applied to the findings of this thesis is carried out. Consequently, a preliminary model is calibrated by utilising solely four formulations, while the remaining two are employed for the purpose of validation. The analysis of the prediction accuracy data is conducted thereafter. Following this, a comprehensive model including all six materials is developed for subsequent utilisation. A seventh powder mixture, whose CS data come from a different CS machine, is then analysed and the applicability of the transfer approach is studied. Lastly, it is examined how the composition and percentages of excipients in a powder blend affect the Johanson parameter values.

Chapter 1

Roll compaction in the pharmaceutical industry

Roller Compaction is a key unit operation of the granulation line in the manufacturing of pharmaceutical tablets. This chapter aims to present the main features of the granulation process, describing the key phenomena involved and the advantages it offers. Afterward, the roll compaction process is introduced, providing a comprehensive explanation of how powders behave during compaction. The advantages and limitations of this technology will be investigated, as well as the elementary design features of the roller compactor. Finally, the rationale and operational principles of the compactor simulator, which represents the second piece of equipment involved in this Thesis, are covered.

1.1 Introduction to the granulation process

Granulation is defined as a process whereby the smaller primary particles are bonded into larger secondary particles, also called agglomerates, in which the primary particles can still be identified. Because the process ultimately results in the production of a larger entity it is also known as size enlargement by agglomeration. The granulation can be performed through compressive pressure, a binding agent, or both (Parikh, 2005). Binders are substances that are added either before or after agglomeration that bind chemically or physically to the solid surfaces, creating a linkage between the particles.

Several different types of binding mechanisms are known that can lead to agglomeration of the primary particles: solid bridges, adhesive and cohesion forces, surface tension and capillary pressure, interlocking bonds, and attraction forces between solids. Those represent the five major groups, I to V, and within them, several subgroups of binding mechanisms can be identified, as reported in Table 1.1 (Pietsch, 2002). Pictorial representations of the aforementioned categories and subcategories are reported in Figure 1.1.

For the technologies and materials involved in this Thesis, the principal binding mechanisms are the ones involving powders without the presence of liquid and heating phenomena, hence groups IV and V. These kinds of forces occur when the primary particles get considerably closer to one another, usually as a result of applied pressure. In particular, Van der Waals forces, which are short-range ones, represent the main contribution to the bond of particles when those are close enough. Given the physical nature of the involved forces, the main factors that affect the successful processing for the agglomeration of primary particles are the powder rheology and the particle size. Decreased particle size significantly improves the surface-to-mass ratio and so increases bonding interactions (Parikh, 2005).

Table 1.1. *The binding mechanisms involved in the agglomeration processes.*

I: Solid bridges	1. Sintering
	2. Partial melting
	3. Chemical reaction
	4. Hardening binders
	5. Recrystallization
II: Adhesion and cohesion forces	1. Highly viscous binders
	2. Adsorption layers
III: Surface tension and capillary pressure	1. Liquid bridges
	2. Capillary pressure
IV: Attraction forces between solids	1. Molecular forces
	a) Van-der-Waals forces
	b) Free chemical bonds
	c) Associations; hydrogen bridges
	2. Electric forces
	3. Magnetic forces
V: Interlocking bounds	

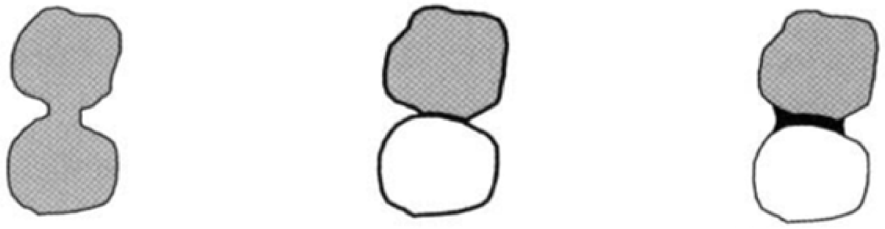

(a)
Sinter Bridges (I.1)
Partial Melting (I.2)
Crystallization of Soluble substances (I.5)

(b)
Chemical reaction (I.3)
Hardening binders (I.4)
Highly viscous binders (II.1)
Adsorption layers (II.2)

(c)
Liquid bridges (III.1)
Hardening binders (I.4)
Crystallization of dissolved substances (I.5)

(d)
Molecular Forces (IV.1)
Electrostatic Forces (IV.2)
Magnetic Forces (IV.3)

(e)
Interlocking (V)

(f)
Matrix binder (I.3, I.4, II.1)
Capillary forces (III.2)

Figure 1.1. *Pictorial representation of the binding mechanisms involved in the agglomeration processes (Pietsch, 2002).*

The granulation technique has been extensively used by a variety of industries, including pharmaceutical, coal, mining, and agrochemical. These industries use agglomeration techniques to minimize dust, make the material easier to handle, and increase its ultimate utility.

In the pharmaceutical industry, the granulation of powders to form structured products is one of the most important operations in the manufacturing of tablets. This type of solid oral drug represents the most widely prescribed dosage forms in use today since they are simpler to manufacture than capsules and have longer shelf life than most liquids (Peter Davies, 2016).

1.1.1 Rationale and benefits of granulation processes

There are numerous reasons for granulating pharmaceutical powder mixtures, the most important of which are listed below:

- Improvement of flow properties. Particle size has a distinct influence on the flowability properties of powders. The enlargement of particles by granulation improves their flowability by decreasing the specific surface area and the particle-particle interaction (Schiano et al., 2018).
- Avoiding segregation and improving content uniformity of tablets. Particle size and differences in particle density within a blend can induce segregation during the manufacturing of tablets, in particular during the die-filling process (Guo et al., 2010). This phenomenon, known as particle segregation, happens when a homogenous mixture of powder particles with varied physical attributes (such as size, density, and shape) becomes unevenly dispersed during handling and processing. Particles with identical qualities, in particular, tend to gather in a single region of the mixture, resulting in spatial non-uniformity. This can lead to false dosing of APIs dosing in the tablet. This issue is even more problematic in tablets containing low doses of API. By granulation, the mixture of the different primary particles and their percentage is fixed in the larger granules, so that an inhomogeneous distribution of the API can be prevented (Cantor et al., 2008).
- Reduction of bulk volume. A further advantage of granulation is the size enlargement of particles which leads to a decrease in interparticle void spaces, resulting in increased bulk density of the powder. Granules occupy less space compared to loosen powders, making them easier to handle, transport, and store. This represents a great advantage in direct compression, where the high bulk volumes require high die-filling height, which can cause problems when filling the die. Furthermore, the deaeration during the compaction becomes difficult, which may result in the capping/lamination of the tablets (Mazel et al., 2015). Lastly, the reduced bulk volume also allows for more efficient packaging, which can lead to cost savings in terms of materials and storage space.
- Reduction of safety hazards for operators. During the granulation process, the formation of larger, denser granules minimizes the generation of fine particles or dust, which are known

to pose respiratory hazards. This is of particular concern when dealing with highly potent drugs when accidental exposure constitutes a significant danger (Keizer, 2021).

- Capability of controlling intermediate and product quality attributes. Within limits, granulation of pharmaceutical powder offers the advantage of allowing control over porosity, density, hardness, and surface-to-volume ratio. By adjusting the granulation process parameters such as binder concentration, granule size, and dry conditions, the porosity of the granules can be tailored. These parameters have a direct impact on the dispersibility, solubility, and reactivity of the granules, as it affects the rate of dissolution and interaction with other substances. Critical quality attributes of tablets, such as disintegration time, dissolution time, and wettability can be improved if the powder blend has been correctly granulated previously (Parikh, 2005)

Other benefits of minor importance that granulation provides include improved product appearance and a lower propensity to caking.

1.1.2 Granulation in the pharmaceutical industry

The development of pharmaceutical granulation was driven by the invention of the tablet press by W. Brockedon in 1843. Since then, numerous different granulation processes and equipment have been developed, resulting in an ongoing process of efficiency and product quality improvement. The demands on the granulation properties were further enhanced in the 1970s when high-speed tablet and capsule-filling machines with automated controls were introduced. In fact, most pharmaceutical tablets cannot be manufactured by direct compression of the formulation because of poor flowability and high segregation tendency. The high-speed compression and capsule-filling machines require a uniform flow of material to the dies or filling stations that produce pharmaceutical dosage forms. Therefore, prior to the compression step, the formulation has to go through a granulation process to improve its handling properties and to assure composition homogeneity in the final dosage form, mostly in low-dose drugs (Parikh, 2005).

Granulation techniques have grown in importance in drug manufacture since the most commonly used excipients and recently created APIs have low bulk density and poor flowability due to their cohesive appearance and small particle size (Szappanos-Csordas, 2018). Agglomeration technologies have played a crucial role in enabling the production of tablet drugs with a high API content, where handling and processing issues were an obstacle.

Figure 1.2 illustrates where the granulation process integrates within the tablet manufacturing process. Two possible paths are possible according if wet or dry granulation is performed. Prior to granulation, all the components of the formulation are mixed. According to the properties of the powder mixture, they undergo two alternative granulation processes. But then in both cases, lubricating agents are added to the agglomerated product. The resulting powder mixture is suitable now to be compacted and coated to form the final tablets.

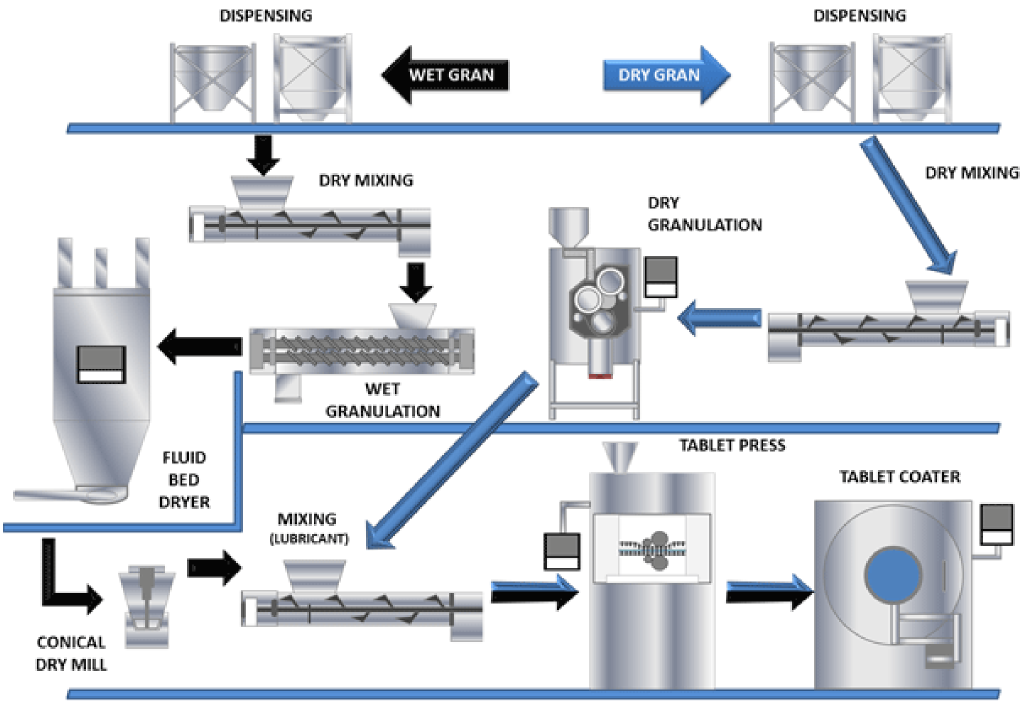

Figure 1.2.*(https://www.epmmagazine.com/opinion/understanding-the-continuous-process/). Schemes of the tablets manufacturing processes by wet granulation and dry granulation.*

The two main techniques for producing granules used in the pharmaceutical industry are wet granulation and dry granulation.

1.1.2.1 Wet granulation

Granules are formed by wetting the powder mixture with the addition of a liquid binder, such as water or organic solvents. In this case, the particles can be either directly enlarged or smaller granules formed by sieving a wet mass (Parikh, 2005). Once the granulation is performed the liquid binder is removed by means of a drying step, which aims to eliminate moisture from the granules while maintaining their integrity and desired properties. The main bonding mechanism within granules formed in wet agglomeration is liquid bridges that are formatted at the coordination points between the particles.

Three wet granulation techniques are used in the pharmaceutical industry: twin-screw granulation, high-shear wet granulation, and fluid bed granulation. Wet granulation is the most used granulation method in the pharmaceutical industry since the granules obtained by this process show good flow properties due to their smooth surface and narrow granule size distribution (Thapa et al., 2019).

Despite the benefits mentioned above, the presence of liquids (such as water or organic solvents) results in a number of drawbacks. Drying is required to remove the liquids, which uses a lot of energy. The multi-stage process is expensive and time-consuming due to the high energy consumption and solvent recycling. The granules are also subjected to heat stress, which can accelerate the degradation process and speed up reactions like decarboxylation and oxidation (Keizer, 2021).

1.1.2.2 Dry granulation

In dry granulation, the agglomeration is achieved by means of the exertion of high pressure on the powder mixture, without the addition of any liquid or meltable binder. The powder is compacted into larger intermediate compacts, which are subsequently milled into granules. In this case, the particle size enlargement is achieved by the size reduction of previously dry compacted powder.

The main bonding mechanism involved in dry granulation is due to Van der Waals forces, which become dominant when the contact area between individual powder particles increases due to the applied compaction pressure (Parikh, 2005).

Dry agglomeration processes have been deployed in the pharmaceutical industry since the 1940s, but in the last 30 years, this technology has arisen as it offers cost-effective and delicate handling for heat and or moisture-sensitive materials since no liquid binders are needed. However, it is important to note that not all powders are suitable for dry granulation. The powder mixture must possess adequate compressibility and cohesive properties for successful compaction. The selection of appropriate excipients and the optimization of process parameters is crucial for achieving desired granule properties.

There are two dry granulation processes: slugging and roll compaction. Between the 1950s-1970s slugging was the preferred method. Slugs are produced when the powder is fed into a large compression machine and compressed by tableting punches having large diameters. The slugs are milled into granules after the compression step (Parikh, 2005). Due to the lack of process control, limited economies of scale, and low manufacturing throughput associated with slugging, roll compaction developed as a preferred dry granulation method, effectively overcoming the limitations of slugging and gaining popularity in the pharmaceutical industry.

1.2 Roller Compactor

Roll compaction is a continuous dry granulation method, which first pharmaceutical application was first mentioned in 1966 by Jaminet and Hess (Kleinebudde, 2004). In agglomeration by roll compaction, mixtures of API and excipients, e.g., binders, disintegrants, diluents, and lubricants, are mixed in a blender. This powder mixture is then fed and passed through two counter-rotating rolls with the flow being induced by the friction acting at the surfaces of the rolls. In the narrow region of the gap between the rolls, the powder is subjected to high pressure, leading to the formation of a compact or briquette that is reduced in size by milling or screening, to achieve the desired granule size. The RC equipment is schematically depicted in Figure 1.3. The produced granules, with improved properties, are used in subsequent processes such as tableting or capsule filling. These granules have particle sizes in the range of 0.2 - 4.0 mm in the pharmaceutical industry, although they are mainly produced with a particle size range of 0.2 - 0.5 mm (Shanmugam, 2015).

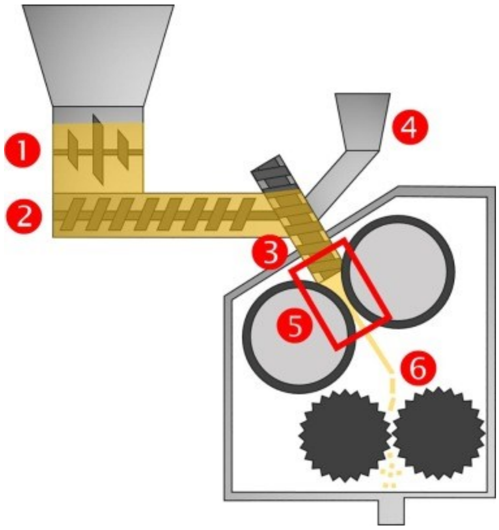

Figure 1.3. *Schematic representation of a roller compactor. (1) inlet funnel with agitator; (2) feed screw; (3) tamp screw; (4) small quantity inlet funnel; (5) rollers; and (6) rotor miller. The mechanistic model describes the region between the rollers (Toson et al., 2019).*

In order to describe, the phenomena occurring during roll compaction granulation in detail, the process is divided into three different regions (Johanson, 1965). The boundaries between the regions are defined by their angular position as reported in Figure 1.4.

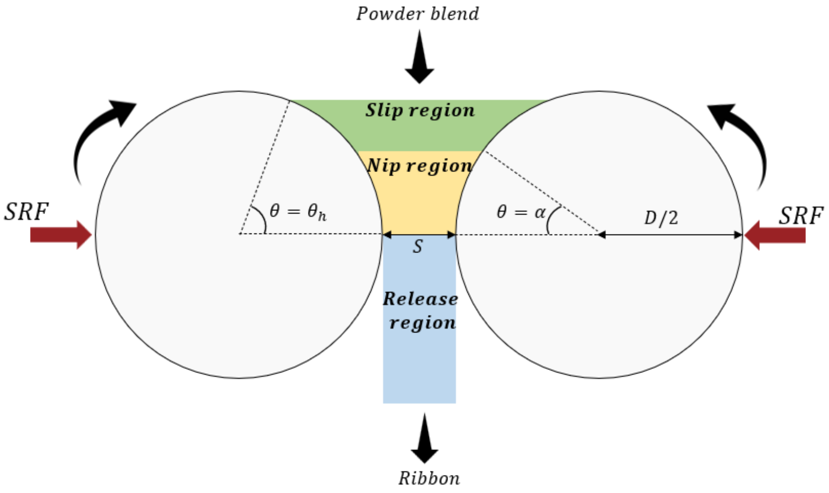

Figure 1.4. *Schematic diagram of the roller compactor process and of the three characteristic regions.*

1. The slip region: The feeding system delivers the powder mixture to the slip or feed region. The start of this region is defined by the entry angle: θ_h. In this stage the powder

particles move slower than the roll surface, and so they slip. In the slip region, the powder is pre-densified primarily due to particle rearrangement and de-aeration, as a consequence of the little stresses applied by the feeding system. The main factors affecting the powder behaviour in the feed region are the frictional properties of the particulate materials, such as wall and inter-particle friction.

2. The nip region: The nip, or compaction, region starts at the nip angle α, where the velocity of the powder blend starts to move with the same velocity as the roll surface. So, the particles are gripped between the two counter-rotating rolls and densification occurs due to the reduction in the roll gap as the powder is dragged to the closest point between rolls. This results in a substantial increase in the roll pressure. The high pressure exerted on the powder causes the breakage of brittle particles and the deformation of plastic ones. The new fractured particles, caused by the fragmentation, and the deformed ones lead to more contact points between the particulate. This induces the bonding of particles at the molecular level due to the effect of Van der Waals forces (Parikh, 2005). The maximum pressure exerted by the rolls is reached at the neutral angle, which does not necessarily occur at the smallest roll gap because of wall slip and other factors (Salman et al., 2006).

   The extent of the nip region depends on the material characteristics and operating parameters. Common values are: $5° < \alpha < 20°$.
3. The release region: Finally, the compacted ribbon is relieved in the release region, where the roll gap starts to increase again the exerted pressure ceases to exist. After the ejection, because of the absence of constraints and stresses, the compacted ribbon may increase in size due to elastic recovery (Salman et al., 2006). The enlargement concern mainly the ribbon thickness and this occurs mainly when dealing with plastic powder materials.

1.2.1 Solid Fraction

The solid fraction (SF), or relative density, is defined as the ratio between the envelope/bulk density and the true density:

$$\gamma = \frac{\rho_E}{\rho_T} . \tag{1.1}$$

It can also be defined using the porosity, ε, in fact, it results:

$$\gamma = 1 - \varepsilon . \tag{1.2}$$

Envelope density, also known as bulk density, is determined for porous materials by including the volume occupied by the pore spaces within the material in the measurement. Conversely, true density is calculated as the ratio of the mass of the solid material to the volume occupied by that mass; therefore, the volume contributions of pores or internal voids are removed in the measurement. The envelope and true density of the powder mixture are usually determined by helium and powder pycnometer.

The SF is the most important intermediate roll compaction product attribute which has a great impact on the downstream processes. Besides the equipment and process-related parameters, it has a significant influence on the granule size distribution in the milling step. Additionally, it is correlated to the flowability, stickiness, reworkability, mechanical strength, homogeneity of the content, disintegration, and dissolution of the resulting grains (Amini and Akseli, 2020). In the roll compaction process, the SF is determined by the flowability and compressibility properties of the powder blend, as well as by machine operating settings.

The term ‘compressibility’ is defined as the ability of a powder to decrease in volume under pressure, while ‘compactibility’ is defined as the ability of the powdered material to be compressed into a tablet of specified strength (i.e. radial tensile strength or deformation hardness).

1.2.2 Advantages and limitations of roll compaction

The distinctive advantage of roll compaction, over other granulation techniques, is its possibility of processing physically or chemically moisture-sensitive materials since the use of liquid binders is not required. Another benefit is that it does not require a drying stage and therefore it is suitable for compounds that either have a low melting point or degrade rapidly upon heating (Leuenberger, 1982). In addition, compared to other dry granulation techniques, such as slugging, roll compaction is a continuous process with higher productivity but less energy consumption and can produce more homogeneous products (Miguélez-Morán et al., 2008). Another key aspect of the increasing popularity of the roll compaction process is the possibility of implementation of online and automation process settings leading to an improvement in product quality, minimizing batch-to-batch variability (Salman et al., 2006).

Together with all the aforementioned advantages this granulation technology has several disadvantages that are the current subject of research and development. One of the most critical limitations is referred to the “loss of compactability”. When a powder mixture is granulated and milled using roll compaction, the resulting tables do not develop as much tensile strength as tablets produced by direct compression of the initial powder blend. For this reason, the analysis of ribbon and tablet product qualities is usually studied combined (Farber et al., 2008).

The high fraction of uncompacted material, referred to as “fines”, during the roll compaction process is another critical drawback. It is mainly caused by two mechanisms: on the one hand by powder that passes the rolls without being compacted and on the other hand by particles generated during the milling step (Reimer and Kleinebudde, 2019). The produced fines can be re-compacted in order to improve the yield, nevertheless, the recycling of fines can lead to inappropriate drug uniformity, therefore the re-compaction of fines is not an advisable manner to increase the throughput. The amount of fines can be reduced, when high compaction pressure, sealing system, and vacuum de-aeration are applied, albeit too high compaction pressure can lead to reduced compactibility of granules (Inghelbrecht and Remon, 1998).

Moreover, the roll compacted ribbon is characterized by density heterogeneity across the roll width and length. This is related to the friction between the powder and the used sealing system, which leads to density variations across the ribbon width. Additionally, the periodical pattern of the screw feeder is visible along the ribbon length in a sinusoidal curve of more densified material (Perez-Gandarillas, 2016). This variability can propagate along the downstream process and influences the tablet quality. It is also required to include a certain amount of lubricant in the powder mixture to avoid material sticking on the roll surface.

The most challenging problem in the roll compaction process is represented in the optimization of processing conditions and the scale-up. This is critical due to the complex behavior of the particulate materials that undergo compaction and also because of the diversity of formulations used in the pharmaceutical industry. This has become even more difficult considering the variety of different equipment designs (Yu, 2013). Suboptimal operation of the equipment can lead to unsatisfactory products.

1.2.3 Process variables

The process variable, i.e. machine settings, that can be adjusted, in order to obtain the desired granules, are common among all the most modern roll compactors. They can be set manually by the operators or controlled by means of the RC controlling system. They are listed, together with the acronym that will be used in this Thesis, as follows:

- Specific Roll Force (*SRF*): The specific roll force represents the force that the roll provides to the powder to be compacted between them. It is expressed in kN per cm of roll width. Among all the machine parameters, it is influencing the ribbon and granules' properties the most.
- Roll Gap (*S*): The roll gap represents the minimum value of the distance between the two counter-rotating rolls. It is usually expressed in mm.
- Roll Speed (*RS*): The counter-rotating rolls move simultaneously with the same speed. Their speed is usually expressed in rounds per minute (rpm). In the case of comparison of roll compactors with different roll diameters, the velocity is expressed as the circumferential one in m/s.
- Screw Speed: Some roller compactor uses a screw feeding system to deliver the powder blend to the slip region. By adjusting the feeding screw speed, the amount of conveyed powder can be regulated.

1.2.4 Roller compactor design

Even though the process variables are common among all industrial RC, the specific designs of the instrumentation present a large degree of variability. These different designs have the capability to affect the properties of the produced ribbons as explained below.

1.2.4.1 Feeding mechanism

The feeding system is a key element of the roller compactor because it has to provide a uniform and continuous flow of powders in order to fill the region between the rolls. If this is not achieved correctly the formed ribbon will present heterogeneity. The powder to be compacted can be fed to the slip region by gravity or by force-feeding using a screw feeder.

In a gravity feed roller compactor, a hopper contains the powder blend and it guides its delivery to the region between rolls. The hopper is usually equipped with an agitator to break powder bridges. Similarly, in the force-feeding system, a screw is placed inside a hopper and the screw is directed to the space between the rolls.

The choice between one feeding system or another is mainly driven according to the flow properties, the density of the powder, and the densification required. Gravity feed is suitable in the case of powder with good flowability, even though it presents some drawbacks due to feeding fluctuations and air escaping. Force feed fits better in the case of poor-flowing particles (Salman et al., 2006).

1.2.4.2 Rolls layout

The rotating rolls can be mounted in three different positions: horizontal, inclined, and vertical. These different layouts are shown in Figure 1.5.

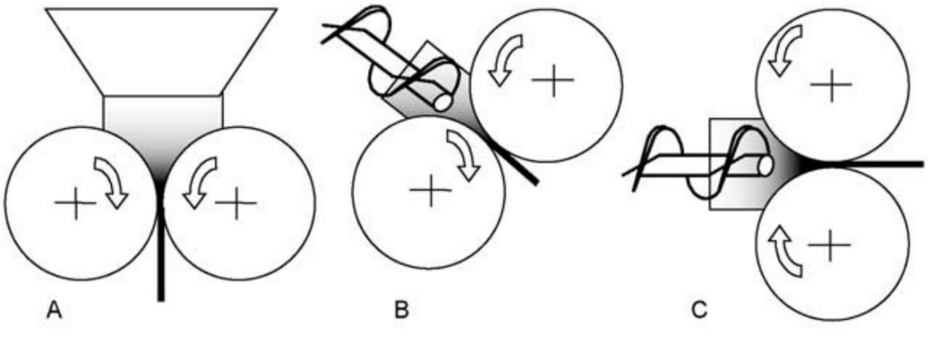

Figure 1.5. *Configuration of roll compactors (A) horizontal (B) inclined (C) vertical (Guigon and Simon, 2003).*

The firstly invented and most commonly used is the horizontal layout with the vertical feeding system. This arrangement can cause by-pass and leakage problems in the case of powder with excellent flowability properties. This issue can be solved using the combination of horizontal feeding and vertical roll layouts, in which the production of uncompacted material is reduced.

However, due to the influence of gravity on the transport of the particles, the densification may result asymmetrical. Hence, the inclined design has been developed in order to possess both advantages of the aforementioned designs (Teng et al., 2009)

1.2.4.3 Roll surface

There are several roll surface options, including smooth, knurled, serrated, and grooved surfaces, as shown in Figure 1.6. The different degrees of roughness of the roll wall impact the friction between the powder particles and the roll surfaces. This can be particularly useful when the loose powder has to be compacted (Szappanos-Csordas, 2018).

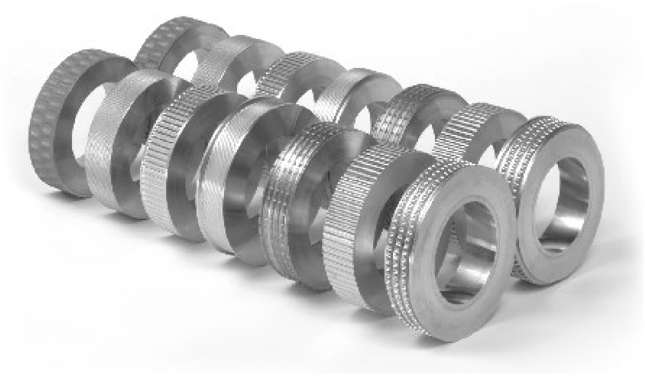

Figure 1.6. *Different roll surface types (Fitzpatrick®).*

1.2.4.4 Sealing system

An important issue to be prevented is the sideway migration of the powder outside the compaction area. For this reason, RC present either a side-sealing system or a rim-roll sealing system, as shown in Figure 1.7.

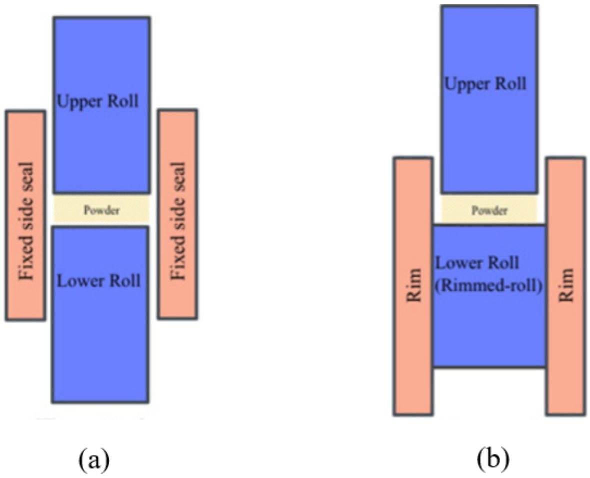

Figure 1.7. *Roller Compactor possible sealing systems: (a) side-sealing; (b) rim-roll sealing (Mazor et. Al., 2015).*

The side-sealing system consists of two plates that form a physical barrier beside the gap width. To avoid metal-metal contact and wear, the side plate is often composed of a PTFE platelet (Salman et al., 2006). The rim-roll sealing system is characterized by one single roll having edges on both sides, while the other roll fits and moves inside the cavity created by these rims. The sealing mechanism utilized has an effect on the manufactured ribbon; for example, the rim-roll sealing system produces a more homogeneous density distribution than the side-sealing system. This is due to uniform pressure distribution along the ribbon width and a reduction in uncompacted material.

1.3 Compactor simulator

The interest in simulating roll compaction processes is particularly high, especially during the early phase of new formulation development. This is primarily due to the limited availability and high cost associated with new APIs. The roll compaction process itself is both time-consuming and material intensive. However, with the aid of an accurate physical simulation, quickly identifying the appropriate process parameters in order to achieve the optimal ribbon quality attributes becomes possible. Consequently, simulations have the potential to significantly expedite the development process and result in substantial cost reductions.

Reproducing the behavior of the powder undergoing compaction by the rolls is challenging due to the complex events that take place. A technique for mimicking the roll compaction process has been developed by Zinchuk et al. (2004) utilizing a laboratory uniaxial press where the punches move with a sinusoidal profile. By utilizing this sine function, the top and bottom punches are capable of emulating the rotational movement of a given point on the roll surface. The mathematical formulation of the simulation is:

$$D = R\sin(\omega t)\,, \tag{1.3}$$

where D is the punches displacement, R is the roll radius, ω is the roll rotation frequency and t is time (Zinchuk et al., 2004). The schematic representation of the simulation transfer is shown in Figure 1.9.

Initially, the powder mixture is inserted in the die chamber of the compactor simulator. At $t = 0$, the punches start to travel towards each other, compressing the powder at the same strain as in the real roll compaction process. The apex of the sinusoidal profile corresponds to the point at which punches and points on the roll surface achieve their minimum spacing and can be used to target the thickness of the simulated ribbons. When the punches have reached their minimum separation, they retract to decompress the ribbon before it is ejected to the die surface by the bottom punch.

The compacted product of the compactor simulator is called ribblet, and its appearance, compared with the ribbon one, is shown in Figure 1.10. The shape of the ribblets is determined by the tooling size and geometry, which can be round or rectangular.

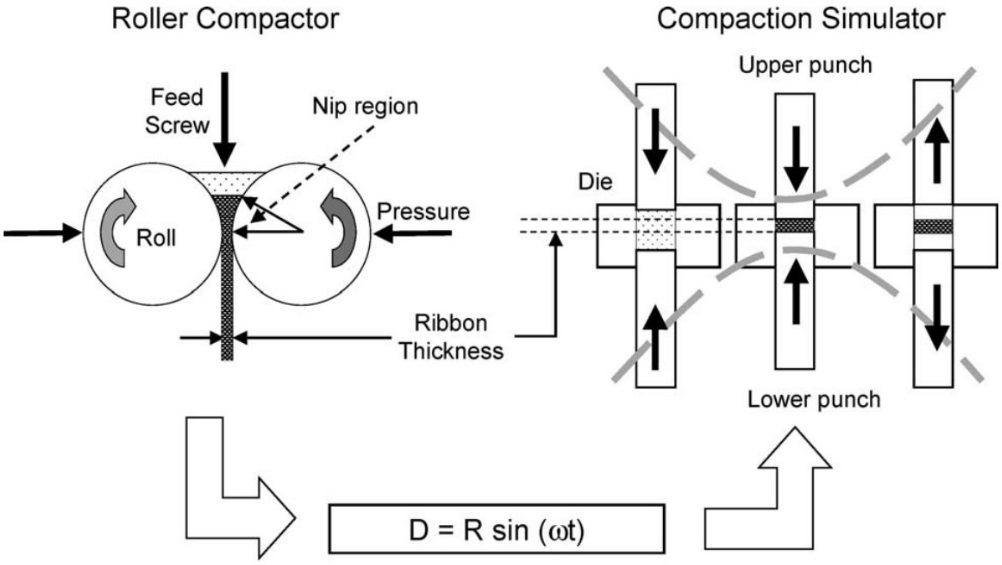

Figure 1.9. *Transfer between roller compactor and compaction simulator. In the compaction simulator representation, three different time instants of the same punches' displacement are reported (Zinchuk et al., 2004).*

To quantitatively evaluate the simulation, two key indicators of the ribblets and ribbons quality have been used and compared by Zinchuk et al., (2004): the SF and the tensile strength. The powder material in the analysis was microcrystalline cellulose. The results showed that ribbons and ribblets with similar SFs exhibit good agreement in tensile strength comparison, indicating that the method is valid for evaluating roll compaction behaviour.

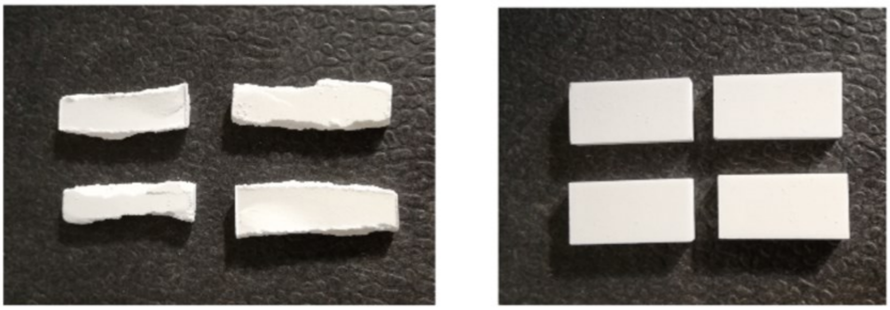

(a) (b)

Figure 1.10. *Compacted products of: (a) Roller compactor: ribbons, (b) Compactor simulator: ribblets (Keizer, 2021).*

This method, therefore, has the great advantage of allowing rapid characterization of the pharmaceutical powders with minimum consumption of material, i.e., in the order of hundreds of milligrams. However, this methodology uses a batch process, i.e., the direct punches compaction, to model a continuous process, i.e., roll compaction. As a result, the simulation is not unable to account for some roll compaction variables associated with continuous operation, such as the feeding system's inhomogeneous powder transport and shear forces on the roll surface (Zinchuk et al., 2004).

Chapter 2

Roll compaction modelling

The Johanson model, which is used in this Thesis to characterise the behaviour of pharmaceutical powders during the roll compaction process, is introduced in this chapter. The physical and mathematical theory of the model and its capability to predict the pressure exerted by the rolls are explained. After that, the theory of the mass correction factor is introduced, which is designed to account for differences between estimated roll pressures and measured simulator ones. This constitutes the base of the proposed methodology for accelerating development operations.

2.1 Johanson (1965) model

Over the years, numerous theoretical models have been developed to explore the mechanics of roll compaction and predict the quality of the resulting compacts. In 1965, Johanson introduced a rolling theory for granular solids. It was the first mathematical model for predicting the extent of the compression region and the pressure distribution after the powder are gripped by the rolls. Following this, Katashinkii (1986) utilized the slab method to analyse the nip region, enabling the prediction of pressure distribution and roll separating force, based on an analysis of metal rolling operations (Reynolds et al., 2010). Both the Johanson model and the slab model are one-dimensional models. In pursuit of more comprehensive insights, researchers have proposed two- and three-dimensional models for roll compaction, focusing on finite element methods (FEM) and discrete element methods (DEM). These numerical approaches offer the advantage of providing detailed and realistic representations of the roll compaction process by considering various material properties, geometries, and particle-particle interactions. However, both FEM and DEM come with inherent limitations, including computational complexity, challenges in calibration, numerical issues, and the requirement for accurate material properties to implement the simulations (Salman et al., 2006).

The Johanson model's ongoing popularity in roll compaction modelling can be ascribed to a number of factors. Firstly, it provides valuable insights into the compaction process, considering density packing and stress relaxation mechanisms, thereby offering a comprehensive understanding of the phenomenon. Secondly, the model delivers reasonably accurate predictions of critical process parameters, further enhancing its appeal for practical applications. Furthermore, the Johanson model has demonstrated strong agreement with experimental data across a wide range of pharmaceutical materials and settings. Because of its broad use, it has become an extremely useful tool for process control and scale-up research. Additionally, its relatively straightforward implementation makes it accessible to researchers and engineers without extensive computational expertise, setting it apart from more complex numerical methods like FEM or DEM.

The Johanson model provides predictions of the roll normal stress distribution, roll torque and force, nip angle, i.e., the angular location along the roll surface at which powder begins to move at the velocity of the rolls and ribbon density at the roll gap. Its predictive capability reduces costs and time, minimizing experimental trials, thus, enabling one to focus on promising process conditions. It aids in the design of robust procedures and high-quality pharmaceutical products by improving understanding of roll compaction mechanics. Furthermore, the model predicts ribbon density and porosity, allowing for better process control and uniformity during production.

In his paper, Johanson divided the zone between the rolls into two regions, as shown in Figure 1.4:

i) the slip region, where the slip occurs along the roll surface
ii) the nip region, where a no-slip boundary condition applies.

The transition from slip to nonslip region defines the nip angle α. The zone beyond the minimum roll gap is usually defined as the release region in which the stresses are relieved and the compacts were extruded from the system.

2.1.1 Pressure distribution in the slip region

To describe the powder behaviour in the slip region, Johanson developed its model on the basis of the Jenike and Shield (1959) criterion for steady-state particle flow in silo and hopper. The roll compacted material is assumed to be isotropic, frictional, cohesive and compressible and also to obey the effective yield function proposed by Jenike and Shield (1959) (Salman et al., 2006). The latter was used by Johanson to represent the plane-strain and plane stress condition of the granular solid between the rolls. The effective yield function for plane strain and plane stress condition of the powder material between the rolls can be represented in Figure 2.1, where δ_E is the effective angle of friction, ϕ_W is the angle of wall friction and ν is the acute angle between the tangent to the roll surface and the direction of the major principal stress σ_1 (Mansa, 2006). The effective angle of friction $\delta_E$and the angle of wall friction ϕ_W are material properties that can be experimentally measured by means of a ring shear test.

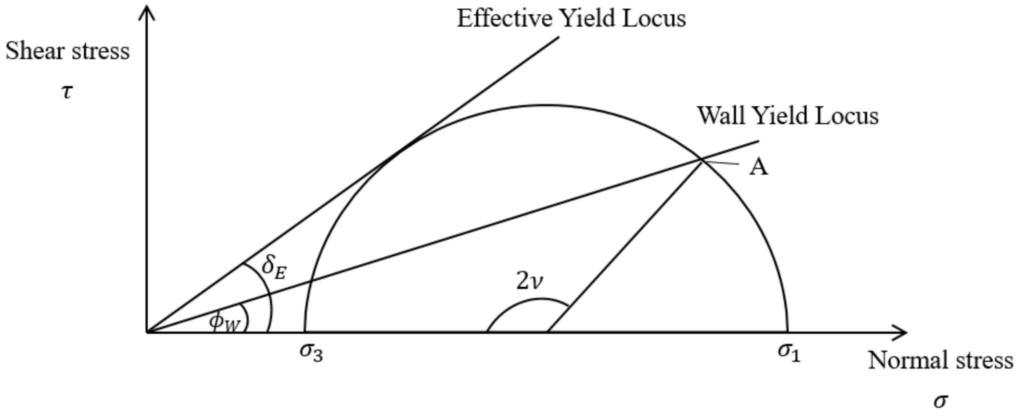

Figure 2.1. *Jenike–Shield yield criterion for the slip region, with the effective and wall yield loci.*

The circle represents the Mohr's circle, which is a method for representing the steady state stress in a material as function of that material. Every point on the circle represents a combination of normal stress σ and shear stress τ on some plane. The two planes of most interest are the planes on which the shear stress is zero, which are known as the major principal plane and the minor principal plane. The stresses acting on these planes are known as the major principal stress σ_1 and the minor principal stress σ_3. By means of these two stresses the effective yield equation can be written as (Mansa, 2006):

$$\sin \delta_E = \frac{\sigma_1 - \sigma_3}{\sigma_1 + \sigma_3} \tag{2.1}$$

At the roll surface, the relationship between the tangential and the normal forces is given by the wall yield locus, as reported in Figure 2.1, where the shear stress and the normal stress at the surface of the rollers are described by Point A. The angle of wall friction ϕ_W describes this locus but, for calculation purposes, it is more convenient to use the acute angle ν (Mansa, 2006):

$$2\nu = \pi - \arcsin\left[\frac{\sin \phi_W}{\sin \delta_E}\right] - \phi_W \tag{2.2}$$

Considering now the pressure gradient $d\sigma/dx$, where x is the vertical axis, as shown in Figure. 2.2. Assuming slip occurs along the roll face, $d\sigma/dx$ would be determined by (2.2) and the Jenike-Shield yield criterion. A first-order approximation for $d\sigma/dx$ is (Johanson, 1965) :

$$\left.\frac{d\sigma}{dx}\right|_{Slip} = \frac{4\sigma\left(\frac{\pi}{2} - \theta - \nu\right)\tan \delta_E}{\frac{D}{2}\left[1 + \frac{S}{D} - \cos\theta\right]\left[\cot(A-\mu) - \cot(A+\mu)\right]}\ , \tag{2.3}$$

where: θ is the angular position in radians at the surface of a roll, such that θ = 0 corresponds to the minimum gap, D represent the rolls diameter expressed in meters, x is the distance upstream from the roll gap and the parameter A is given by:

$$A = \frac{\theta + \nu + \frac{\pi}{2}}{2} \ . \tag{2.4}$$

In (2.3) μ represents the friction coefficient of the material and it is given by:

$$\mu = \frac{\pi}{4} - \frac{\delta_E}{2} \ . \tag{2.5}$$

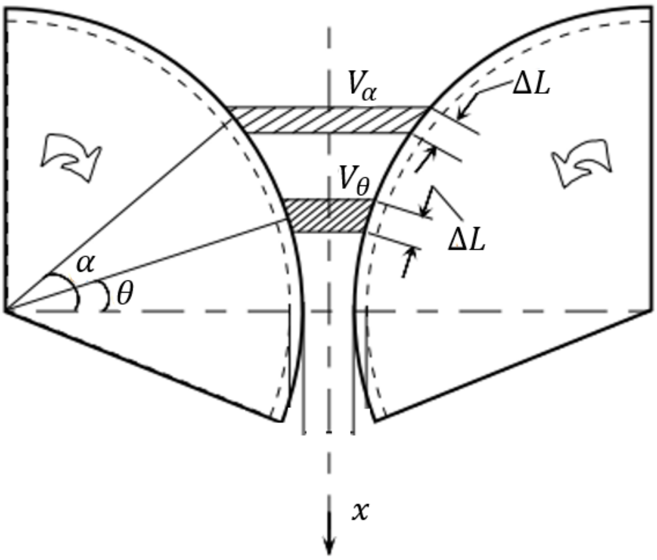

Figure 2.2. *Region of nip in the roller compactor, where the element of volume V undergo compaction (Mansa, 2006).*

2.1.2 Pressure distribution in the nip region

For angles smaller than the nip angle, i.e., the no-slip region, Johanson argues that the Jenike-Shield yield behaviour no longer applies (Nagy and El Hagrasy, 2020). Because there is no slip along the roll surface in the nip zone, the powder must be compressed to the final roll gap dimension. This means that a volume V_α, as reported in Figure 2.2, must be compressed to a volume V_θ between the same arc-length segments. Continuity requires that the bulk densities ρ_α and ρ_θ in the volumes V_α and V_θ be related by:

$$V_\theta \rho_\theta = V_\alpha \rho_\alpha \implies \frac{\rho_\alpha}{\rho_\theta} = \frac{V_\theta}{V_\alpha} \ . \tag{2.6}$$

The pressure σ_θ at any angle $\theta < \alpha$ can be determined as a function of σ_α, that corresponds to the pressure at an angle $\theta = \alpha$, by adopting the pressure-density relationship. Based on empirical evidence, Johanson stated that for increasing pressures the log density is a linear function of log pressure:

$$\frac{\sigma_\alpha}{\sigma_\theta} = \left(\frac{\rho_\alpha}{\rho_\theta}\right)^K , \tag{2.7}$$

where K is the compressibility constant, which is a property of the material where small K values indicate very compressible materials and large K values indicate incompressible materials (Mansa, 2006). The powder compressibility K is defined as the reciprocal of the slope of the linear trend of the pressure profile in a double-log diagram, as shown in Figure 2.3.

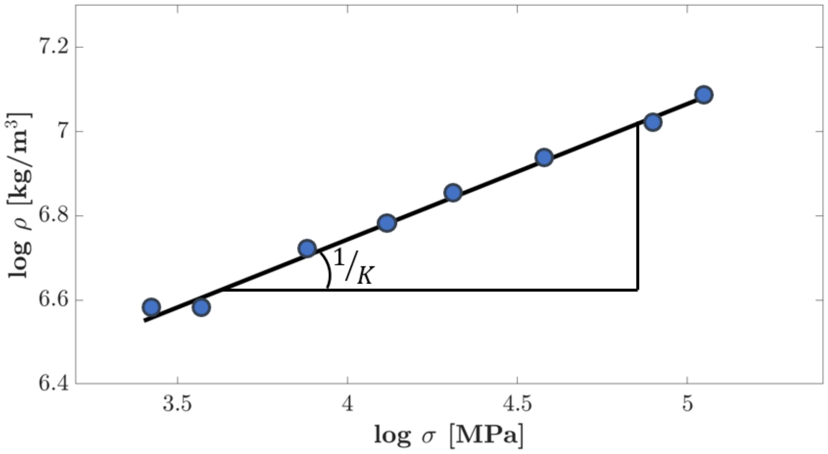

Figure 2.3. *Linear function used to describe the trend of log$_{10}$ of density against log$_{10}$ of pressure of experimental data points (blue dots).*

Substituting (2.6) into (2.7) gives a normal stress-volume relationship:

$$\frac{\sigma_\theta}{\sigma_\alpha} = \left(\frac{V_\alpha}{V_\theta}\right)^K. \tag{2.8}$$

For smooth roll surface, the volume of powder V_θ between the arc-lengths segment ΔL is:

$$V_\theta = \Delta L\, W[S + D(1 - \cos\theta)]\cos\theta\,, \tag{2.9}$$

where W is the roll width expressed in meters. Combining (2.8) and (2.9) leads to:

$$\sigma_\theta = \sigma_\alpha \left[\frac{\left(1 + \frac{S}{D} - \cos\alpha\right)\cos\alpha}{\left(1 + \frac{S}{D} - \cos\theta\right)\cos\theta}\right]^K. \tag{2.10}$$

As a result, if the nip angle is known, the pressure distribution between the rolls may be calculated. Eq. (2.10) is only applicable for angles $\theta < \alpha$.When slip does not occur along the roll surface, pressure σ is given by (2.9) and the pressure gradient is (Johanson, 1965):

$$\left.\frac{d\sigma}{dx}\right|_{Nip} = \frac{K\sigma\left(2\cos\theta - 1 - \frac{S}{D}\right)\tan\theta}{\frac{D}{2}\left[(1 + \frac{S}{D} - \cos\theta)\cos\theta\right]}. \tag{2.11}$$

This pressure gradient is zero for angles $\theta = 0°$ and for $\theta = 60°$.

2.1.3 Determination of the nip angle

Johanson (1965) proposed that the nip angle can be determined by finding the angle at which the pressure gradients for the slip and no-slip conditions were equal. Hence, the nip angle can be determined by equating (2.3) and (2.11) and solving for $\theta = \alpha$:

$$\frac{4\sigma\left(\frac{\pi}{2}-\theta-\nu\right)\tan\delta_E}{\frac{D}{2}\left[1+\frac{S}{D}-\cos\theta\right]\left[\cot(A-\mu)-\cot(A+\mu)\right]}=\frac{K\sigma\left(2\cos\theta-1-\frac{S}{D}\right)\tan\theta}{\frac{D}{2}\left[\left(1+\frac{S}{D}-\cos\theta\right)\cos\theta\right]}. \qquad (2.12)$$

The nonlinear equation (2.12) must be solved numerically. The intersection of the two vertical pressure gradients, which coincide with the angular position equal to α, is shown in Figure 2.4.

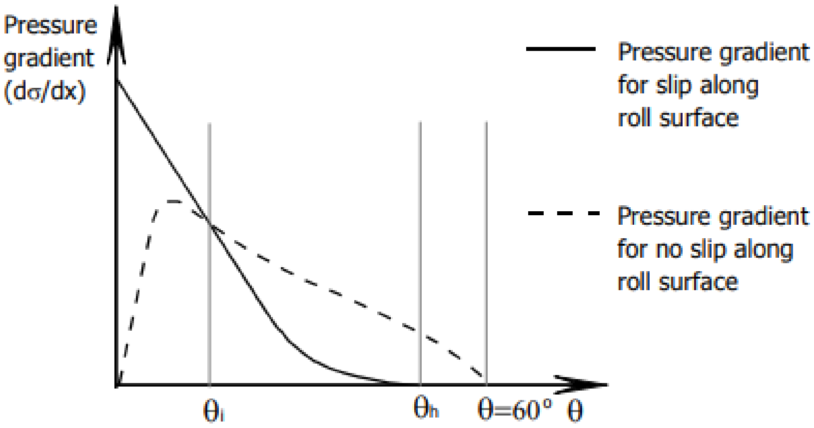

Figure 2.4. *Vertical pressure gradient versus angular position for both slip and no slip condition (Mansa, 2006).*

The solid line in the Figure 2.4 represents a typical pressure gradient profile given by (2.3) for the condition of slip along the roll surface. When $\theta = \theta_h$, which represents the upper boundary of the slip region, as shown in Figure 1.4, the pressure gradient $d\sigma/dx$ is zero. On the other hand, when slip does not occur along the roll surface, the pressure gradient is provided by (2.11), which is depicted in Figure 2.4 as a dashed line.

Considering how (2.12) is expressed, it results that the nip angle value depends on the compressibility constant K, on the material flowability properties, δ_E and ϕ_W, and on the roller compactor machine settings D and S. However, the impact of the geometry parameters on the value of α is almost negligible, provided that $S/D \ll 1$. The effect of material properties on the value of the nip angle is shown by means of surface plots in Figure 2.5.

It can be seen that δ_E has a lower effect, while ϕ_W and K have a strong impact on the determination of the value of α. Greater ϕ_W and K, wider will be the nip region and so the angle from which the powder mixture will start to be compacted by the rolls.

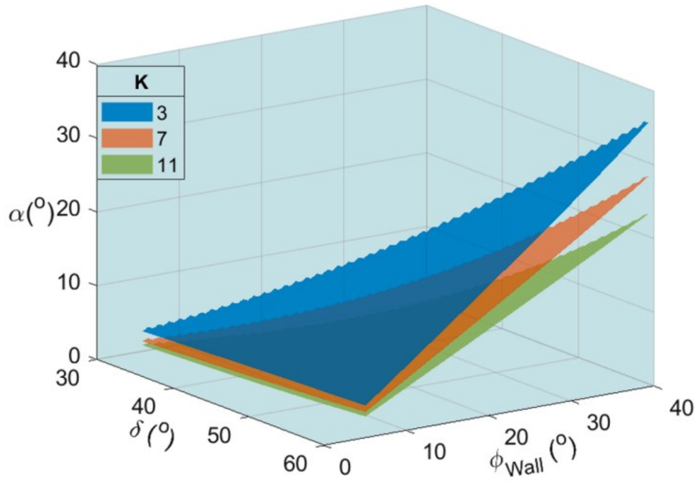

Figure 2.5. *Change of the nip angle (α) as the function of varying compressibility, wall friction angle, and effective angle of internal friction (So et al., 2021).*

2.1.4 Peak pressure and ribbon solid fraction

Once the nip angle has been determined, the pressure distribution between the rolls can be calculated from (2.10). The resulting SF of the ribbon obtained from the roll compaction process is determined by the maximum pressure applied to the powder material during compression. In practical applications, the peak pressure, denoted as P_{max}, corresponds to the maximum pressure exerted on the powder at the minimum roll gap S when $\theta = 0$, and it can be related to the roller force, represented as R_f [kN], according to the Johanson model:

$$P_{max} = \frac{2R_f}{WDF} \;, \tag{2.13}$$

where F is the force factor and it is defined as:

$$F = \int_{\theta=0}^{\theta=\alpha(\delta_E,\phi_W,K)} \left[\frac{\left(\frac{S}{D}\right)}{\left(1+\frac{S}{D}-\cos\theta\right)\cos\theta} \right]^K \cos\theta \, d\theta \,. \tag{2.14}$$

This represents a relationship between process parameters (roll force R_f, roll separation distance S), geometric parameters (roll diameter D, roll width W) and material properties (effective angle of internal friction δ_E, angle of wall friction ϕ_W and compressibility K (Reynolds et al., 2010). Eq. (2.14) implicitly assumes the contributions of the pressure on the rolls in the slip region and the release region are negligible. According to (2.14) the peak pressure increases as the specific roll force increase while it decreases as the roll gap increases. The trend of the peak pressure as function of the two adjustable machine setting parameters is shown in Figure 2.6, where data are generated using (2.13) and (2.14):

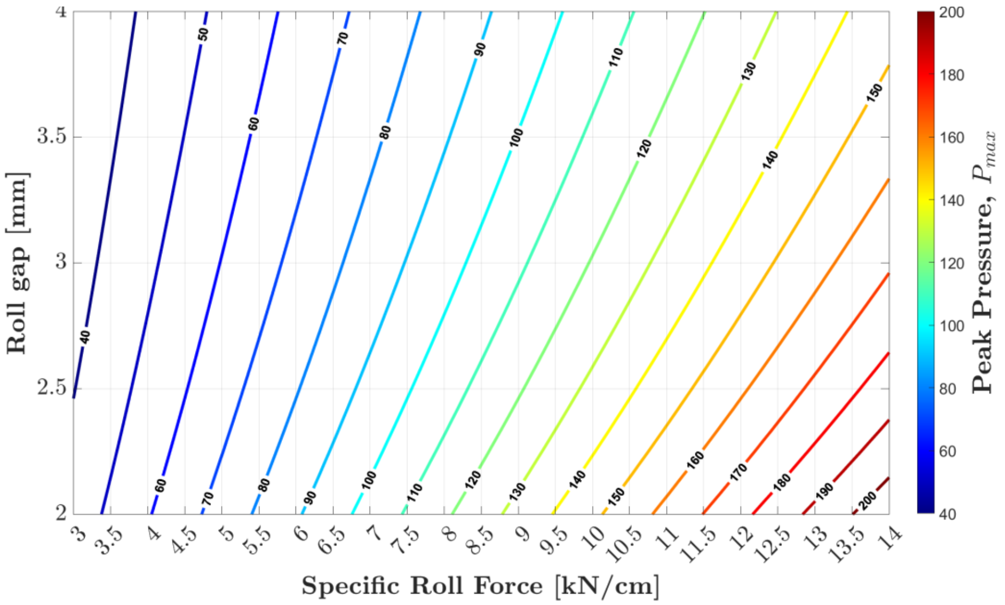

Figure 2.6. *Contour plot showing the changes of the peak pressure as function of the specific roll force SRF* (R_f/W)*, and the minimum roll gap* S.

Bindhumadhavan et al. (2005) used an instrumented roll compactor fitted with a miniature piezoelectric transducer in order to measure the pressure profile normal to the roll surface. They found that the pressure distribution is reasonably predicted from Eq. (2.10), although the measured pressure increased more strongly than the predicted as the material enters the nip region. They also found that the peak pressure applied was very accurately predicted (Bindhumadhavan et al., 2005).

Once the peak pressure is known it can be used to determine the relative density that results from the applied pressure of the rolls. Eq. (2.10) is based on a power law relationship between material density and pressure. Following this, the relative density or SF of the ribbon γ_R, can be estimated from the peak pressure as follows:

$$\gamma_R = \gamma_0 P_{max}^{\frac{1}{K}} \;, \tag{2.15}$$

where γ_0 is referred to as the pre-consolidation relative density or pre-consolidation solid fraction, which is, similarly to K, a compaction parameter depending on the material. γ_0 and K represent the two model parameters of the Johanson model, whose values have to be calibrated using experimental data from roller compactor experiments. Typically, the pre-consolidation density γ_0 corresponds to the relative density at a reference pressure of 1 MPa (Moroney et al., 2020).

After determining the values of γ_0 and K, it becomes possible to construct the compression profile that describes the trend of the ribbon SF and the predicted peak pressure, according to (2.15). An illustrative example of the roller compactor compression profile is depicted in Figure 2.7.

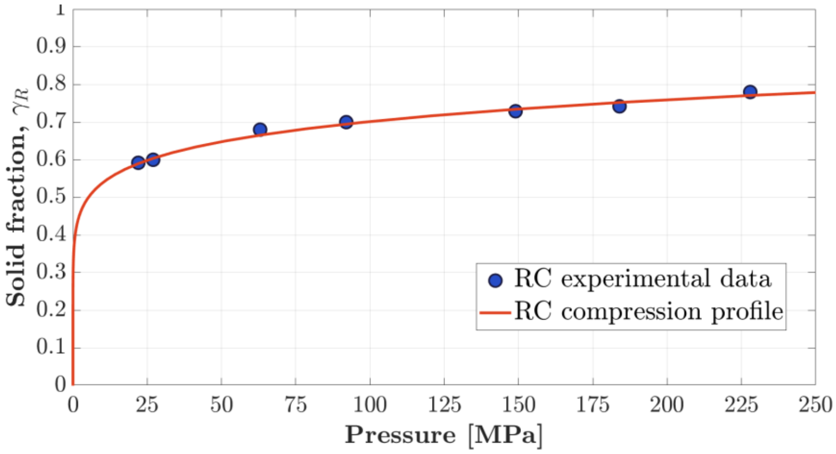

Figure 2.7. *Example of a roller compactor compression profile built according to the Johanson model.*

Incorporating (2.13) and (2.14) into (2.15) expresses the relationship between process output γ_R, and process parameters R_f, S, D and W, as follows:

$$\gamma_R = \gamma_0 \left(\frac{2R_f}{WD \int_{\theta=0}^{\theta=\alpha(\delta_E, \phi_W, K)} \left[\frac{\left(\frac{S}{D}\right)}{\left(1 + \frac{S}{D} - \cos\theta\right)\cos\theta} \right]^K \cos\theta \, d\theta} \right)^{\frac{1}{K}}. \qquad (2.16)$$

Note that the equation in this form requires the units of the bracketed term to be in MPa (Moroney et al., 2020).

2.1.5 Assumptions and limits of the Johanson model

As described in the previous section, the Johanson model comes with certain limitations due to its underlying assumptions. Firstly, the material is assumed to be isotropic, frictional, cohesive, compressible and to obey the effective yield function proposed by Jenike and Shield (1959). When deriving (2.6), it is assumed that: i) the plane strain of the element of volume V_θ remains perfectly plane, ii) mass continuity theory holds true, or iii) there is no velocity gradient through the ribbon thickness as the element of material moves to minimum gap between the rolls (Bi et al., 2014). Additional powder properties used in the model include the effective angle of internal friction and the powder-roll friction angle, both of which are assumed constant with relative density, which is reasonable at the large stresses expected in a RC (Liu and Wassgren, 2016). Moreover, the Johanson model assumes negligible elastic recovery of the ribbon formed during the compaction process, thus simplifying the material behaviour by considering minimal or no rebound of the particles after compression. This assumption can lead to a discrepancy between the predicted SF at the minimum roll gap and the measured one due to the increase in ribbon volume resulting from elastic recovery. Additionally, the model assumes the roll gap to be fully filled with powder, neglecting the possibility of air entrapment. In practice, air entrapment can occur, significantly affecting the overall densification process and leading to ribbon density and porosity variations.

2.2 Mass correction factor theory

Despite the fact that the Johanson model is widely and consistently used to characterise roll compaction, various investigations have demonstrated that it tends to result in disparities between predicted and actual pressure values (Reynolds et al., 2010; Bi et al., 2014; Toson et al., 2019; So et al., 2021). In the attempt to validate the Johanson model, especially regarding the estimation of peak pressure applied by the rollers, predicted pressure values were compared with measurements obtained from uniaxial compaction equipment. Such comparisons, however, regularly resulted in disagreements, mainly because of the inaccurate assumption of one-dimensional flow of the powder particles within the nip region. According to Bi et al. (2014), this assumption is erroneous because the material close to the roll surface moves quicker than the material further away from the roll surface in the nip region. The velocity gradient gradually decreases as the powder particles move from the nip angle toward the minimum gap, as illustrated in Figure 2.8, where particles velocities between the rollers are represented by a contour plot from a FEM simulation.

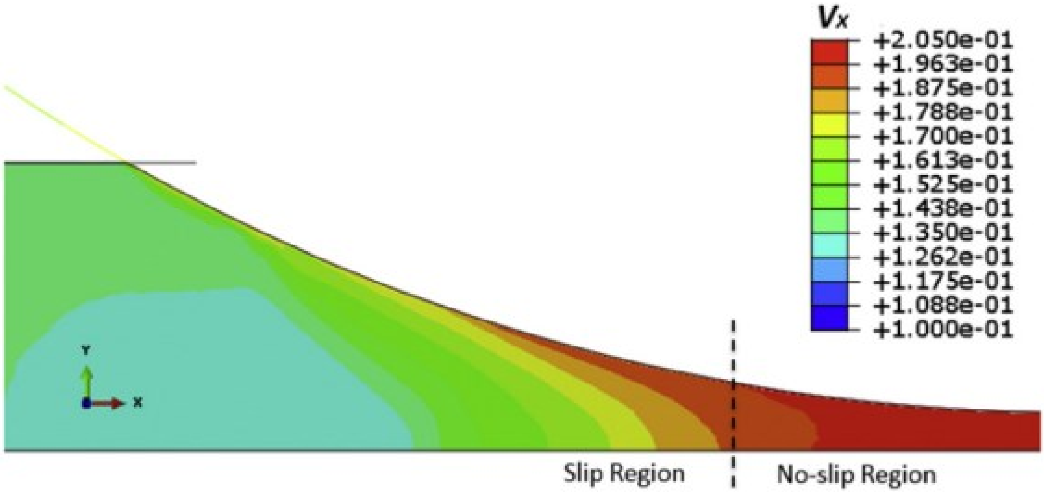

Figure 2.8. *Streamwise component of the powder velocity generated from an FEM simulation (Liu and Wassgren, 2016).*

The Johanson model assumes that the entire element of powder material moves at the same speed as the roll. Consequently, Johanson's rolling theory overestimates the amount of material delivered to the minimum roll gap, leading to an overprediction of the maximum roll pressure.

In their study, Bi et al. (2014) introduced a mass correction factor f_θ into the mass conservation equation in the nip region (2.6). This correction factor was incorporated to address the variation in mass within each element caused by multi-dimensional flow:

$$V_\theta \rho'_\theta = f_\theta V_\alpha \rho_\alpha \, . \tag{2.17}$$

The variable that has been corrected using the mass correction factor is represented by the symbol with the apex. The introduction of the mass correction factor in (2.17) changes not only the stress-density connection but also the stress-volume relationship (Bi et al., 2014):

$$\frac{\sigma_\alpha}{\sigma'_\theta} = \left(\frac{f_\theta \rho_\alpha}{\rho'_\theta}\right)^K = \left(\frac{V_\theta}{f_\theta V_\alpha}\right)^K . \tag{2.18}$$

Combining now (2.18) with (2.10), the resulting pressure in the no-slip region is:

$$\sigma'_\theta = \sigma_\alpha \left[\frac{f_\theta\left(1+\frac{S}{D}-\cos\alpha\right)\cos\alpha}{\left(1+\frac{S}{D}-\cos\theta\right)\cos\theta}\right]^K . \tag{2.19}$$

Following the same derivation line, the force factor becomes:

$$F' = \int_{\theta=0}^{\theta=\alpha(\delta_E,\phi_W,K)} \left[\frac{f_0\left(\frac{S}{D}\right)}{\left(1+\frac{S}{D}-\cos\theta\right)\cos\theta}\right]^K \cos\theta \, d\theta \, , \tag{2.20}$$

where f_0 is the actual fraction of powder delivered from nip angle α to angle $\theta = 0$, so that the force factor from (2.21) can be written as (Bi et al., 2014):

$$F' = f_0^K \int_{\theta=0}^{\theta=\alpha(\delta_E,\phi_W,K)} \left[\frac{\left(\frac{S}{D}\right)}{\left(1+\frac{S}{D}-\cos\theta\right)\cos\theta}\right]^K \cos\theta \, d\theta \ . \tag{2.21}$$

Moving f_0 outside the integral from (2.20) to (2.21), it implicitly assumes that the mass correction factor is θ-independent. This assumption has been shown to be incorrect by Liu et al. (2016), who performed a roll compaction FEM simulation in which they demonstrate the dependence of the mass correction factor on position θ within the roll compactor. Nevertheless, despite the lack of mathematical rigor, the equation proposed by Bi et al. (2014), where the correction was presented as a multiplier outside the integral, demonstrated acceptable predictive capabilities without necessitating additional simulation efforts, thus enhancing its practical applicability (So et al., 2021).

From (2.21) the peak pressure exerted by the rolls at $\theta = 0$ can be rewritten as:

$$P_{max} = \frac{2R_f}{f_0^K WDF} \, , \tag{2.22}$$

Rearranging (2.22) maximum roll surface pressure after mass correction P_{max} is derived as follow (Bi et al., 2014):

$$P'_{max} = f_0^K P_{max} \ . \tag{2.23}$$

The pressures predicted by the Johanson model P_{max} model and the pressures experimentally measured by a uniaxial compactor P'_{max} for the same SF obtained in the compacted product can now be related through (2.23). This correction, in fact, accounts for the overprediction of the exerted roll pressure for the same values of SF. In this Thesis, (2.23) is revised to explicitly state the CS pressure as:

$$P_{CS} = f_0^K P_{max} \ . \tag{2.24}$$

To account for pressure overprediction f_0 has to assumed values lower than 1. In their case study, Bi et al. (2014) employed the mass correction factor theory, investigating three different active pharmaceutical powder mixtures on both the roller compactor and the uniaxial compactor. The mass correction factor f_0 was used to explain the differences in pressure for the experimental obtained data. The absolute values of f_0 linking the different pressures of each roller compactor experimental data ranged between 0.86 and 0.89. This indicated that only 86% to 89% of the powder material, as claimed by the Johanson model, was delivered at the angle $\theta = 0$. Additionally, their research revealed that the mean values of the factor f_0 derived for the three powder mixtures were similar.

This Thesis aims to analyse the pressure differences between experimental results obtained from the RC and the CS. The bridging element that will allow a relationship between the two pressures to be created is the mass correction factor. Initially, an exploratory analysis will be made to examine the values of f_0 required to link the different pressures for each analysed powder mixture, as done in previous literature work. Based on this analysis, a methodology, based on the mass correction factor, for predicting roller compactor pressures based purely on simulator data will be proposed.

Chapter 3

Materials and methods

In this chapter, a comprehensive presentation of the pharmaceutical powder mixtures used in this project will be provided, along with their specific compositions and characterizations. Subsequently, the experimental procedures conducted by the partner company on the RC and on the CS will be described in detail. The available datasets will be presented, together with the methods employed to obtain the data. Finally, the methodologies used to estimate the parameters, as well as the confidence intervals associated with them, will be thoroughly examined in relation to the models describing powder compaction on both the RC and the simulator.

3.1 Powder mixture

In this Thesis, seven different pharmaceutical powder mixtures were considered. Four of them were placebo formulations, i.e., they did not contain any APIs. They were designed to resemble a real drug in appearance, but had no therapeutic effects on the body. The use of placebo formulations has relevance in clinical studies since it allows for the assessment of the effectiveness of new drugs. The remaining three powder combinations, on the other hand, contained APIs amounts. However, while the precise weight compositions were known, the specific mixture components themselves were not.

Placebo formulations were made of different excipients, which are inert or inactive powder materials added to ease the tabletting operation and to improve the quality of the tablet. However, the term excipient includes multiple kinds of particle components with distinct functions: diluent, binders, lubricants, disintegrants, and glidants. The four placebo formulations in the analysis contained four different commonly used excipients:

- Microcrystalline cellulose (MCC): Microcrystalline cellulose is a purified, partially depolymerised cellulose that occurs as a white, odourless, tasteless, crystalline powder composed of porous particles. MCC is widely used in the pharmaceutical industry as an ideal binder, due to its excellent compactability under a wide range of compaction pressures, and its resistance to organic and non-organic contaminants (Yu, 2013). Microcrystalline cellulose, like the following excipients, is commercially available with different grades according to its method of manufacture, particle size, moisture content, flow, and other physical properties (Rowe et al., 2009). MCC Avicel® PH 102 was the specific grade used in this Thesis, and it is characterized by a nominal mean particle size of 100 µm. Because of its deformation behaviour under compaction pressure, microcrystalline cellulose is considered a plastic material.

- Anhydrous lactose: Anhydrous lactose is a disaccharide sugar, that occurs as white to off-white crystalline particles or powder. It is widely used in tablet manufacturing for its filler and binder properties and also because of its low moisture content. Lactose anhydrous Supertab® AN 21 was the specific grade of this excipient used in this Thesis. It presents a nominal mean particle size equal to ≈ 150 µm (Rowe et al., 2009). Differently from MCC, lactose is considered a brittle material because of its fragile deformation.
- Mannitol: Mannitol is a naturally occurring sugar alcohol that occurs as a white, odourless, crystalline powder. It is mostly utilised in the pharmaceutical industry as a diluent for tablet drugs, where it is particularly advantageous because it is not hygroscopic and therefore may be used with moisture-sensitive APIs. In this work, Mannitol Pearlitol® 200SD was used. Being a spray-dried grade of mannitol, it presents a larger surface and better compactability compared to unprocessed mannitol. Similarly to lactose, the mean particle size of mannitol 200 SD is equal to ≈ 170 µm (Perez-Gandarillas, 2016). Similarly to anhydrous lactose, spry-dried mannitol possesses a brittle behaviour.
- Magnesium stearate (MgSt): Magnesium stearate is primarily used in tablet manufacture as a lubricant. Its concentration in the formulation is kept usually between 0.25% and 5.0% (Rowe et al., 2009).

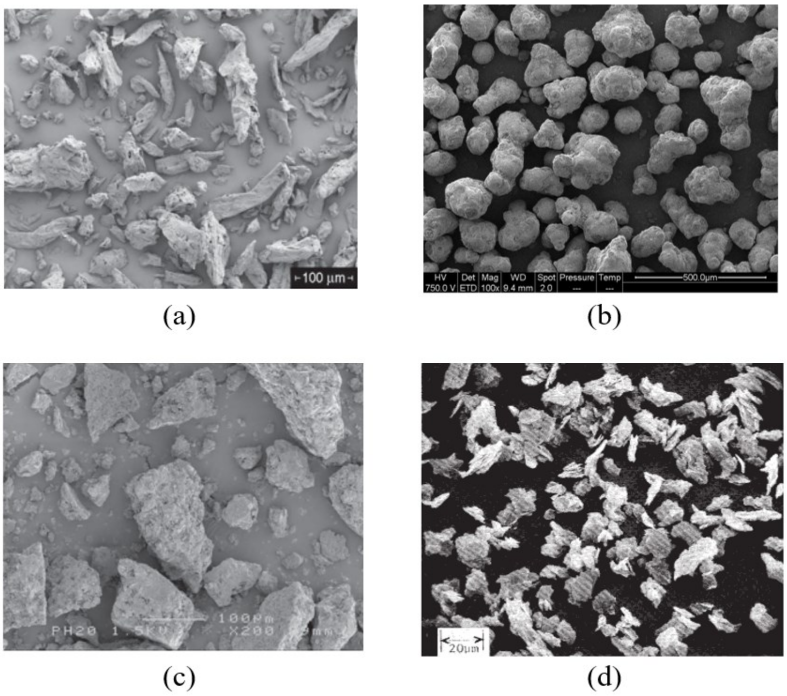

(a) (b)

(c) (d)

Figure 3.1. *SEM imagines the four excipients: (a) microcrystalline cellulose, Avicel PH 102; (b) mannitol, Pearlitol 200 DS; (c) Lactose anhydrous SuperTab 21AN; (d) Magnesium Stearate (Rowe et al., 2009; https://www.roquette.com/innovation-hub/pharma/product-profile-pages/pearlitol-200sd-mannitol).*

The scanning electron microscope (SEM) imagines of all the aforementioned excipients are shown in Figure 3.1.

All the seven pharmaceutical blends that were used in this Thesis are reported, with their composition, in Table 3.1. The term "formulation" is used to refer to the placebo powder mixture, while the term "compound" refers to powder blends containing APIs.

Table 3.1. *List of materials and their compositions.*

Material	Composition (w/w%)
Formulation 1	70% Lactose 29% MCC 1% MgSt
Formulation 2	50% Lactose 49% MCC 1% MgSt
Formulation 3	30% Lactose 69% MCC 1% MgSt
Formulation 4	50% Mannitol 49% MCC 1% MgSt
Compound A	25.4% API_1 74.6% Excipients
Compound B	25% API_2 75% Excipients
Compound C	87.5% API_3 12.5% Excipients

The excipients in the first three formulations were the same; however, their weight percentages differed. Formulation 4, on the other hand, was the only placebo formulation that contained Mannitol. Compound C stood out among the active mixes when compared to the others, mainly because of the amount of API it contained. To distinguish the different APIs contained in the three Compound powder blends, a numerical subscript is used in Table 3.1 (API_1, API_2, API_3). The composition and pharmaceutical grade of excipients in the active compounds may differ from those contained in the four placebo formulations.

3.1.1 Powder characterization

For the specific scopes of this Thesis, the powder blends were characterized for material properties like true density, the effective angle of internal friction, and the wall friction angle. This information was strictly required in order to solve the Johanson model, as in (2.16), and to calculate the SF, eq. (1.1), of the compacted products.

- True density: Prior to compaction the true density of the powder blends was obtained using a helium pycnometer (AccuPyc® II 1340, Micromeritics, Norcross, GA, USA).
- Wall friction angle: The wall friction angle was measured using a ring shear tester, where the type of steel and the surface of the disc were the same as those of the roll surface of the RC.
- Effective angle of internal friction: Effective angle of internal friction of the powder blends was also measured using the ring shear tester.

Table 3.2 reports all the results of the material characterization analysis.

Table 3.2. *Results of powder blends characterisation.*

Material	True density [g/cm^3]	Wall friction angle, ϕ_w [°]	Effective angle of internal friction, δ_E [°]
Formulation 1	1.553	12.5	38.0
Formulation 2	1.562	9.0	37.5
Formulation 3	1.571	11.0	44.0
Formulation 4	1.547	16.0	51.0
Compound A	1.470	39.0	44.0
Compound B	1.529	23.2	46.8
Compound C	1.390	39.8	44.6

3.2 Roller compactor

3.2.1 Gerteis Mini-Pactor®

In the present Thesis, the experimental results regarding the roll compaction were performed using the Gerties Mini-Pactor® (Gerteis Machinen + Processengineering AG, Jona, Switzerland). Due to its dimension and the powder quantity that it can work, Mini-Pactor is a RC used for mainly for laboratory development and pilot projects. The theoretical maximum throughput declared by the company is 100 kg/h, however, the maximum throughput that can be achieved during operation is typically in the range of 50–70 kg/h (Bano et al., 2022). Full-scale production RC can reach throughput capacity up to 400 kg/h. The equipment is shown in Figure 3.2.

The Gerteis Mini-Pactor® was equipped with a horizontally positioned feeding screw and an inclined tamping screw. The rim-roll sealing system, as illustrated in Section §1.2.4.4, has been adopted for the experimental campaigns. As for the specific choice of roll surface, the knurled type was selected. These specific layouts are shown in Figure 3.3.

The rolls presented a diameter equal to 250 mm and a width of 25 mm; and they were set up with the inclined layout, specifically with an angle of 30° corresponding to the horizontal plane.

Figure 3.2. ***(https://www.pharmaceutical-networking.com/gerteis-mini-pactor/)*** *Gerteis Mini-Pactor®.*

The three machine settings that can be adjusted are the roll gap, which has a range of 1 to 6 mm, the specific roll force, which has a range of 1 to 20 kN/cm, and the roller speed, which has a range of 1 to 30 rpm.

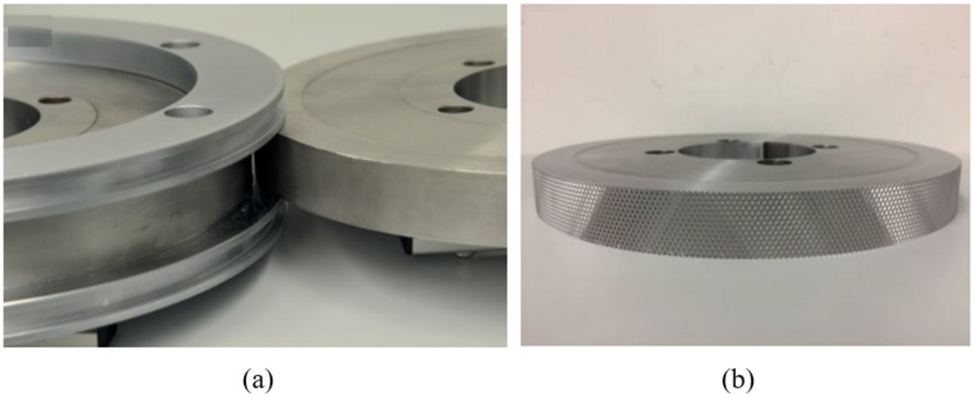

(a) (b)

Figure 3.3. *Roller compactor specific design: (a) rim roll sealing system;(b) knurdel rolls (Szappanos-Csordas, 2018).*

Multiple runs were carried out at various combinations of machine settings in order to investigate the behaviour of the compacted powder at various pressures exerted. The roll speed was kept constant at 2 rpm, while the specific roll force and the roll gap were adjusted depending on the run. Typically, for conducting an experimental campaign involving four different conditions, i.e., four runs, at least of 2.5 kg of material is required. The summary of all roller compactor experimental campaigns is reported in Table 3.3.

Table 3.3. *Roll compaction experiments conducted for each material.*

Material	Dataset ID	Specific roll force [kN/cm]	Roll gap [mm]	Run repetition
Formulation 1	RC-F1	3.0	2	1
		6.0	2	1
		9.0	2	1
		12.0	2	1
		4.2	4	1
Formulation 2 Formulation 3 Formulation 4	RC-F2 RC-F3 RC-F4	3.0	2	1
		6.0	2	1
		9.0	2	1
		12.0	2	1
		4.2	4	1
		8.5	4	1
		3.0	4	1
		6.0	4	1
Compound A	RC-CA	4.0	2	2
		6.0	2	11
		8.0	2	8
		5.0	3	2
		7.5	3	2
		10.0	3	2
		14.0	3	2
Compound B	RC-CB	3.5	2	1
		5.5	2	7
		10.0	2	1
		6.5	3	1
Compound C	RC-CC	1.0	2	1
		1.5	2	2
		2.0	2	3
		2.5	2	2
		3.0	2	3
		3.5	2	2
		3.8	2	3
		4.0	2	2
		4.5	2	4
		4.5	3	1

Formulations 2,3 and 4 were tested with the same total number of runs and with the same machine setting combinations. Formulation 1, on the other hand, had a slightly different testing process, as it was evaluated using only the first five machine setting combinations of the other formulations. Moreover, Compounds A, B and C were investigated using completely different experimental protocols, in terms of machine parameter pairings that were adjusted during their experimental campaign. A total of 27 runs were done for Compound A, adjusting 8 distinct combinations of machine settings, with at least two runs performed for each. As a result, six ribbon samples were available for each combination of machine settings. Regarding Compound B, four combinations of machine parameters were used, but, in only one of them, multiple repetitions were performed. Finally, 23 runs were carried out for compound C, with up to 10 distinct combinations of machine parameters being adjusted. It should be noted that these combinations showed specific roller force values that were close to one another. The addition of multiple repetitions within a single run also provides the opportunity to investigate and analyse the process variability.

3.2.2 Ribbon solid fraction

Three samples were obtained from the compacted ribbon for each run to determine the envelope density and hence the SF of the ribbon. Rectangular samples with dimensions of 25 by 10 mm were extracted from the ribbon for the envelope density measurement. The three independent samples were taken at different segments of the ribbon to account for the potential variability of SF over the width and length of the ribbon. The envelope density of each sample was measured using a powder pycnometer (GeoPyc® 1365, Micromeritics, Norcross, GA, USA) to calculate the SF of the ribbon, as indicated in (1.1). Because the sample were extracted from the ribbon after compaction, this measurement is referred to as "out-of-die." This term is used to distinguish between SF samples obtained at the precise moment of maximum compaction and those obtained after compaction. Because of the influence of elastic recovery in out-of-die samples, distinguishing between the two measurements is critical. When pressure is released, the compacted material expands, resulting in an increase in volume and, as a result, a decrease in bulk density and SF. To ensure reliable comparisons, it is important to consistently specify whether measurements are performed in-die or out-of-die.

By having three samples available for each run, it becomes possible to calculate the corresponding standard deviation, which enables the analysis of intra-run variability. The RC dataset for Compound C only contains the average values corresponding to each run.

All the measured values of the ribbon SF for each RC dataset are reported in the Tables in Section §A.1 of the Appendix.

3.3 Compactor simulator

During this project, the compaction behaviour of powder mixtures was studied by running more than a single experimental campaign for each of them on the CS. As will be elucidated in this section, the experimental campaigns also differed in the diameters of the punches used for the simulator. Furthermore, Compound C was investigated using a distinct CS, which employed a different modality for moving the punches compared to the method utilized for other powder mixtures. For this reason, the results concerning this specific powder blend will be treated separately from those tested on the same piece of equipment. The two different CS are shown in Figure 3.4.


(a) (b)

Figure 3.4. *(https://www.medelpharm.com/instruments/instruments-products.html#styl_one_evolution ; https://www.merlin-pc.com/) Compactor simulators used during the experimental part: (a) Styl'One®;(b) Phoenix®.*

3.3.1 Phoenix®

The initial CS datasets came from an experimental campaign carried out by a third-party company (Merlin Powder Characterisation, Brierley Hill, UK). The reason behind this was an initial mechanical issue with the GSK® simulator, which required the use of equipment from a third-party company. The equipment used was the Phoenix® (Phoenix Calibration & Services Ltd, Bobbington, UK) compactor simulator equipped with round punches with tooling diameters equal to 18 mm. In each test, an automated process filled the CS die with a specific amount of the powder mixture. The pressure was applied through a sinusoidal profile using two counter-moving punches, as illustrated in Section §1.3. In this experimental campaign, only Formulations 2,3 and 4 were tested. The summary of the 18mm Phoenix® CS experimental campaign is reported in Table 3.4.

Table 3.4. *Summary table of the CS experimental campaign performed on the Phoenix® with 18mm tooling diameters.*

Material	Dataset ID	Pressure range [MPa]	Solid fraction range [-]	No. of experiments
Formulation 2	CS18-F2	19-122	0.58-0.83	10
Formulation 3	CS18-F3	19-145	0.54-0.85	25
Formulation 4	CS18-F4	18-117	0.56-0.79	25

Formulation 2 was tested at only two treatment levels, where five repetitions were performed for each. Formulations 3 and 4, instead, were investigated at three treatment levels, where ten repetitions were performed at the edge levels and 5 at the central level.

A second experimental using the Phoenix® CS was performed internally in GSK®. Through this experimental campaign, all powder mixtures, except Compound C, were tested using round punches with a diameter of 10 mm. Because of the smaller diameter diameters, this configuration has an additional advantage in that it requires fewer materials during the experimental phase. Approximately 250 mg of powder mixture is required for a single test using this setup. The summary of the 10mm Styl'One® CS experimental campaign is reported in Table 3.5.

Table 3.5. *Summary table of the CS experimental campaign performed on the Phoenix® with 10mm tooling diameter.*

Material	Dataset ID	Pressure range [MPa]	Solid fraction range [-]	No. of experiments
Formulation 1	CS10-F1	18-192	0.61-0.85	40
Formulation 2	CS10-F2	22-220	0.58-0.90	35
Formulation 3	CS10-F3	22-195	0.56-0.87	35
Formulation 4	CS10-F4	23-193	0.56-0.85	35
Compound A	CS10-CA	18-163	0.57-0.82	30
Compound B	CS10-CB	28-249	0.62-0.87	40

For each powder blend, the total number of experiments were performed among various treatment levels. Within each treatment level, five experiments were carried out. The number of experiments and pressure ranges evaluated for all formulations is substantially larger than in the 18 mm CS datasets, enabling the best description of the behaviour of the powder being compressed. Given that an experimental campaign on CS normally includes 35 tests, each of which consumes roughly 250 mg of material, the total material consumption on a simulator with a punch diameter of 10 mm is approximately 9 grams. In comparison, as pointed out in the previous section, an experimental campaign on RC requires a minimum of 8 runs, with an average of 2.5 kg of material utilized per 4 runs. Consequently, a complete experimental campaign on the RC necessitates at least about 5 kg of material. This implies that the material used for a full experimental campaign on the RC is approximately 550 times greater than what is needed to complete an experimental campaign on the CS.

Compound A and B were again tested using the Phoenix® CS but with a further size of tooling diameter, i.e., 21.85 mm. With this setup, more material, compared to the 10 mm punches diameter layout, is required for a single test; in fact, 700 mg of powder is required. These datasets are summarized in Table 3.6.

The pressure range explored in the 21.85mm simulator datasets is substantially narrower than the pressure range investigated in the 10 and 18 mm datasets, resulting in much smaller intervals of the produced SF. Consequently, these datasets, as they are, do not provide an adequate understanding of the compressibility behaviour of a specific powder.

Table 3.6. *Summary table of the CS experimental campaign performed on the Phoenix® with 21.85mm tooling diameter.*

Material	Dataset ID	Pressure range [MPa]	Solid fraction range [-]	No. of experiments
Compound A	CS21-CA	25-67	0.63-0.75	34
Compound B	CS21-CB	34-67	0.64-0.70	38

3.3.2 Styl'One®

Lastly, Compound C was investigated using a Styl'One® (Medelpharm, France) compactor simulator, equipped with 11.29 mm tooling diameters. In contrast to previous campaigns on the Phoenix® CS, where pressure was applied with a sinusoidal profile utilising two counter-moving punches, in this instance a single axial arrangement was used. This indicated that one punch was moving and compacting the powder mixtures while the other remained still. Due to its experimental campaign with a distinct piece of equipment and a different modality, Compound C was treated separately from all the other results obtained from the Phoenix® simulator. The Summary of the 11.29 mm Styl'One® CS experimental campaign is reported in Table 3.7.

Table 3.7. *Summary table of the CS experimental campaign performed on the Styl'One® with 11.29mm tooling diameters.*

Material	Dataset ID	Pressure range [MPa]	Solid fraction range [-]	No. of experiments
Compound C	CS11-CC	28-176	0.73-0.94	105

As can be seen, for Compound C, a large number of experiments were conducted, and nearly all of these were distributed throughout 7 distinct treatment levels.

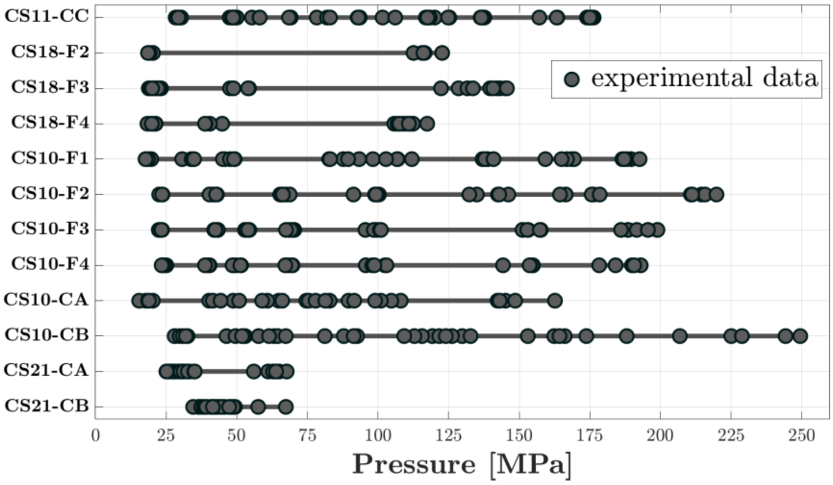

Figure 3.5. *Graphical representation of the pressure range and experiment distribution of the various compactor simulator datasets.*

Figure 3.5 shows a graphical representation of all the CS experimental campaigns to help with visualization and highlight the differences in pressure range between the various experimented blends. The pressure range explored by the experimental campaign varies between the different powder mixtures and between treatment levels.

3.3.3 Ribblet solid fraction

Once the powder blends were compacted by the CS, the samples were ejected from the die by the lower punch. The envelope density of the produced ribblets was measured using the GeoPyc® 1365 powder pycnometer. Similarly to the density measurement in the RC, this measurement was also conducted out-of-die. Consequently, the impact of elastic recovery, which was consistent across both equipment, can be disregarded. All the measured values of the ribblets SF for each CS dataset are reported in the Tables in Section §A.2 of the Appendix.

3.4 Johanson model parameters estimation

The estimation of the pressure exerted by the rolls required the values of the two Johanson model parameter, ${\gamma_0}_{RC}$ and K_{RC}, as reported in (2.13) and (2.14). ${\gamma_0}_{RC}$ and K_{RC} are material-dependent parameters, so they are different for each powder mixture. The introduction of subscripts associated with the γ_0 and K allows for distinction based on the equipment from which these parameters have been estimated. Estimation of these parameters required utilizing experimental data on the SF of the ribbon. By employing these results, along with the corresponding machine settings used to obtain them, the model parameters were adjusted to better align with the experimental outcomes. A challenging aspect of estimating the Johanson model parameters was that it did not involve simply fitting a curve or model to given experimental points in the SF-pressure coordinates. In fact, being involved also in the computation of the nip angle and of the peak pressure, the x-coordinates of the experimental points on the SF-pressure diagram changed as K_{RC} changed. A customized parameter estimation algorithm was necessary to estimate the Johanson model parameters. The iterative computational procedure depicted in Figure 3.6 was employed for this purpose.

The input data that the computational procedure required were the following:

- Equipment geometry information: roll diameter D, and rolls width W.
- Flowability properties of the powder mixture: effective angle of internal friction δ_E, and wall angle of friction ϕ_W.
- RC experimental data: experimental ribbon solid fraction γ_R^{exp} , roll gap S and roll force SRF.

- First guess of the Johanson model parameters: $\gamma_{0_{RC}}$ and K_{RC}. The initial parameter values for $\gamma_{0_{RC}}$ and K_{RC} were chosen based on their physical interpretation and literature results. Specifically, the guess values were set at $\gamma_{0_{RC}}$ = 0.3 and K_{RC} = 5.0.

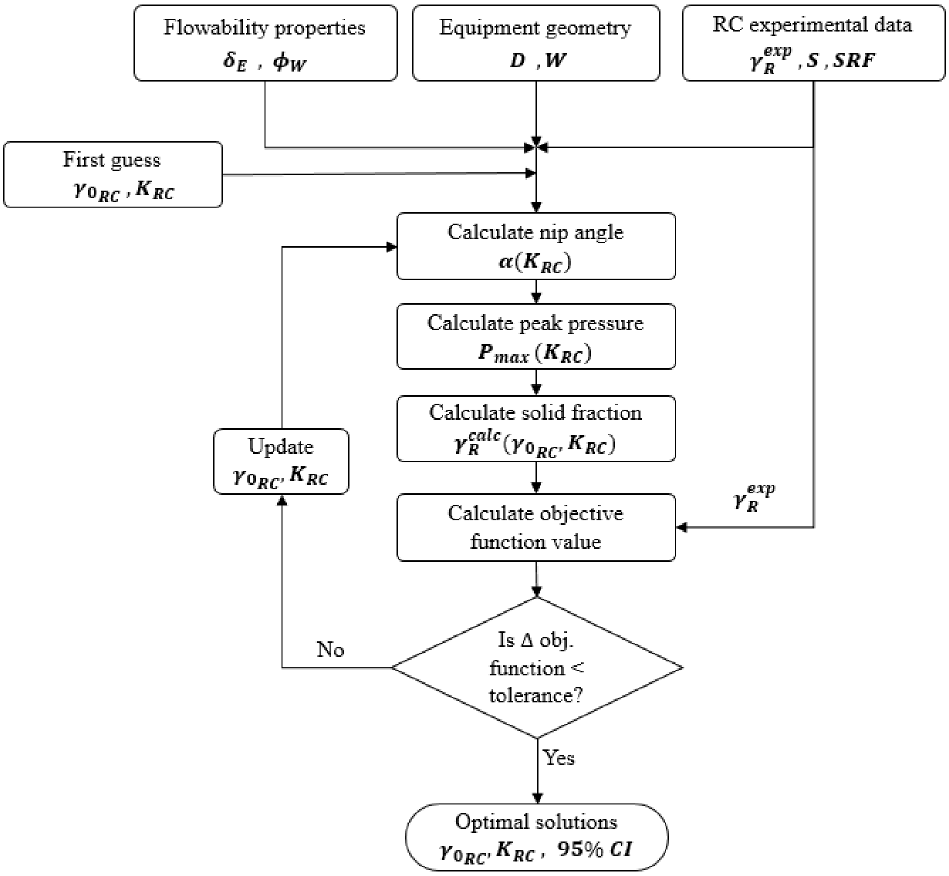

Figure 3.6. *Flow chart of the Johanson model parameter estimation procedure.*

Once all this information was available, the iterative computational procedure worked as follows:

i. For each RC experimental run, the values of the nip angles α, were determined by estimating them using the nonlinear equation (2.12). This was necessary because the nip angle is a function of the set roll gap. At the first iteration, the compressibility values used is the one on the initial guess. Eq. (2.12) was solved using the *fsolved* Matlab® function.

ii. Utilizing the estimated nip angle values obtained at step (i.), the peak pressure values for each experimental run, hence each machine setting combination were calculated using (2.13) and (2.14). Also, at this stage, the compressibility constant used at the first iteration was the initially guessed one. The integral function of (2.14) was solved using the *int* Matlab® function.

iii. At this step, an estimation of the peak pressure was obtained for each run, which was associated with the experimental ribbon SFs. By utilizing the values of the Johanson model parameters, the calculated ribbon SFs were computed for each exerted pressure according to equation (2.15).

iv. By utilizing the obtained values of the calculated ribbon SF and the experimental ones, the objective function at this iteration was computed. The specific formulation of the objective function will be presented in Section §3.4.1. Essentially, the objective function aimed to find the values of ${\gamma_0}_{RC}$ and K_{RC} that resulted in the best fit between the calculated and experimental ribbon SFs.

v. The objective function values from the current iteration were compared to those from the previous iteration to calculate the difference. This difference indicates how close the objective function was to reach a minimum. Finding the objective function minimum means identifying the parameter values that resulted in the most precise calculation of the ribbon SF in relation to the experimental data. This computation only took place from the second iteration since no comparison was possible in the first iteration.

vi. The objective function difference, between the present iteration and the previous one, was compared to the tolerance, which value was set to 10^{-6}. If the objective function difference was greater than the tolerance, the values of ${\gamma_0}_{RC}$ and K_{RC} were modified and the computational procedure restarted from step (i.). The value of ${\gamma_0}_{RC}$ and K_{RC} of the subsequent iteration were adjusted based on the gradient of the objective function. Specifically, the new parameter values were chosen to ensure a decrease in the objective function, as indicated by the computed gradient. This adjustment aimed at minimizing the objective function, thus improving the overall optimization process.

vii. The values of the Johanson model parameters were estimated and the Hessian matrix at the final iteration was computed. The Hessian matrix is the second-order gradient matrix and it contains information about the variability of the objective function with respect to the two parameters. In fact, from the Hessian matrix, as will be presented in Section §3.4.2, the confidence intervals of the retrieved parameters were computed.

The whole minimization iterative procedure was performed using the *fminunc* Matlab® solver. The *fminunc* function is a local minimizer, which means that starting from an initial point, it seeks to finds the minimum of a function using local information derived from the function's partial derivatives. However, the output of this solver may not necessarily represent the desired global minimum, as it is sensitive to the starting point, hence to the guess parameter values. To verify if the obtained results correspond to the optimal set of parameter values, the iterative computational procedure was also performed using a global minimizer, that was the *GlobalSearch* Matlab® function. Results obtained from the local and the global optimizers do coincide. However, given the global minimizer's substantially longer convergence time, which is on the order of minutes, the local optimizer is sufficient for this task, given its faster convergence time, which is on the order of seconds.

3.4.1 Maximum likelihood objective function

The objective function chosen to perform the estimation of the Johanson model parameters was the maximum likelihood objective function. Maximum likelihood estimation (MLE) is a method used to determine the values of model parameters, in such a way that they maximise the likelihood that the data-generating process, described by the model, produced the experiments that were actually observed (Ruud, 2000).

The formulation of the maximum likelihood objective function relies on the concept of likelihood. Consider a set of independent and identically distributed random variables $\{Z_1, Z_2, \dots, Z_n\}$, where each Z_i follows a proability distribution characterized by the parameter vector $\boldsymbol{\theta} = \theta_1, \theta_2, \dots, \theta_k$. The likelihood function is defined as the joint probability of observing the data points $z_1, z_2, \dots, z_n$ given the parameters values $\boldsymbol{\theta}$**.**

Mathematically, the likelihood function can be expressed as the product of the individual probabilities (Ruud, 2000):

$$\mathcal{L}(\boldsymbol{\theta}|z_1, z_2, \dots, z_n) = \Pr(z_1, z_2, \dots, z_n|\boldsymbol{\theta}) = \prod_{i=1}^{n} \Pr(Z_i = z_i)\,. \tag{3.1}$$

Independence between datapoint is assumed, which allow to express of the joint probability as the product of individual probabilities. For continuous distributions, the likelihood function corresponds to the probability density function associated to the joint distribution of independent and identically distributed variables $Z_1, Z_2, \dots, Z_n$ evaluated at the poiny $\{z_1, z_2, \dots, z_n\}$ (Ruud, 2000):

$$\mathcal{L}(\boldsymbol{\theta}|z_1, z_2, \dots, z_n) = \prod_{i=1}^{n} f_Z\,(z_i|\boldsymbol{\theta})\,, \tag{3.2}$$

where $f_Z\,(z_i|\boldsymbol{\theta})$ denotes the probability density function of the single *Z*.

The values of the parameters that maximize $\mathcal{L}(\boldsymbol{\theta}|z_1, z_2, \dots, z_n)$ are the maximum likelihood estimates, denoted by $\widehat{\boldsymbol{\theta}}$, which are therefore obtained by the maximization of (Ruud, 2000):

$$\widehat{\boldsymbol{\theta}} = \arg\max_{\boldsymbol{\theta}} \mathcal{L}(\boldsymbol{\theta}|z_1, z_2, \dots, z_n)\,. \tag{3.3}$$

where the *arg max* function returns the points of the domain of the given function, at which the function values are maximized. The obtained set of the parameters value are the ones that make the observed data most probable.

Allowing to deal with summation instead that with the product, the log-likelihood function, $\ell(\boldsymbol{\theta}|z_1, z_2, \dots, z_n)$, which is the natural logarithm of the likelihood function, is used in the optimization process. This is possible because, since the logarithm function is a continuous and strictly increasing function over the range of likelihood, the values that maximize the likelihood also maximize its logarithm (Ruud, 2000):

$$\widehat{\boldsymbol{\theta}} = \arg\max_{\boldsymbol{\theta}} \ell(\boldsymbol{\theta}|z_1, z_2, \dots, z_n)\,. \tag{3.4}$$

If $Z_1, Z_2, \dots, Z_n$ are normally and independent distributed variables, with mean μ and variance σ^2, hence $\boldsymbol{\theta} = [\mu, \sigma^2]$, and the realization is denoted with $z_1, z_2, \dots, z_n$, the log likelihood function is expressed by (Ruud, 2000):

$$\ell(\boldsymbol{\theta}|z_1, z_2, \dots, z_n) = -\frac{n}{2}\ln 2\pi\,\sigma^2 - \frac{1}{2\sigma^2}\sum_{i=1}^{n}(z_i - \mu)^2\,. \tag{3.5}$$

All the above mathematical background of the MLE can also be used to estimate the parameters of a model such as:

$$y = g(\boldsymbol{x}, \boldsymbol{\beta}) + \varepsilon\,, \tag{3.6}$$

where g is the model function, $\boldsymbol{x}$ is the vector containing the independent variebles, i.e., model input, y is instead the dependent variable, $\boldsymbol{\beta}$ is the vector of the model parameters, and ε is the error. For our specific application, $g(\boldsymbol{x}, \boldsymbol{\beta})$ was represented the Johanson model, where the independent variables $\boldsymbol{x}$ were represented by the material properties, the roller geometry and the machine settings, while the parameter vector $\boldsymbol{\beta}$ was made by $\gamma_{0_{\mathrm{RC}}}$ and K_{RC}.
If two continuous variables Y and X are considered, and Y is assumed to have a conditional distribution given X, the probability density function, denoted by $f_{Y|X}(y|z, \boldsymbol{\theta})$, the conditional log-likelihood function is defined as:

$$\ell(\boldsymbol{\theta}; y|x) = \sum_{i=1}^{n}\ln f_{Y|X}(y|z, \boldsymbol{\theta})\,. \tag{3.7}$$

If the errors ε_i are assumed to be independently and identically distributed with a normal distribution with mean equal to 0 and variance equalt to; the conditional distribution of Y given X is a Gaussian distribution with mean $g(\boldsymbol{x_i}, \boldsymbol{\beta})$ and variance σ^2 (Ruud, 2000).
The log-likelihood function hence become:

$$\ell(\boldsymbol{\theta}; y|x) = -\frac{n}{2}\ln 2\pi\,\sigma^2 - \frac{1}{2\sigma^2}\sum_{i=1}^{n}(y_i - g(\boldsymbol{x_i}, \boldsymbol{\beta}))^2\,. \tag{3.8}$$

The errors from which the variance σ^2 is computed are defined considering the residuals:

$$\varepsilon_i = y_i^{exp} - y_i^{calc}\,, \tag{3.9}$$

that must be normally distributed with mean equal to 0. Therefore, the log-likelihood function fits a normal distribution to the residual, assuming the form:

$$\ell(\boldsymbol{\theta}, \boldsymbol{\beta}, \varepsilon_1, \dots, \varepsilon_n) = -\frac{n}{2}\ln 2\pi\,\sigma^2 - \frac{1}{2\sigma^2}\sum_{i=1}^{n}(y_i^{exp} - y_i^{calc})^2\,, \tag{3.10}$$

where n is the number of experimental observations, y_i^{exp} is the experimental value of the i^{th} observation and y_i^{calc} is the corresponding output of the model calculated using the corresponding model inuts and the model parameters:

$$y_i^{calc} = g\left(\boldsymbol{x_i^{exp}}, \boldsymbol{\beta}\right). \tag{3.11}$$

The objective of the MLE is to find the values of parameters which maximize the log-likelihood function (3.10), and this is equivalent to minimize the negative log-likelihood function:

$$-\ell(\boldsymbol{\theta}, \boldsymbol{\beta}, \varepsilon_1, \dots, \varepsilon_n) = +\frac{n}{2}\ln 2\pi\,\sigma^2 + \frac{1}{2\sigma^2}\sum_{i=1}^{n}(y_i^{exp} - y_i^{calc})^2 . \tag{3.12}$$

Eq. (3.12) is the general form of the MLE objective function, for the Johanson model parameters it can be rewritten as:

$$-\ell(\boldsymbol{\theta}, \gamma_0, K, \varepsilon_1, \dots, \varepsilon_n) = +\frac{n}{2}\ln 2\pi\,\sigma^2 + \frac{1}{2\sigma^2}\sum_{i=1}^{n}(\gamma_{R,i}^{exp} - \gamma_{R,i}^{calc})^2 . \tag{3.13}$$

Eq. (3.13) is the exact objective function that must be minimised in order to estimate the Johanson model parameter for each powder blend according on its experimental data. The value of $\gamma_{0_{\mathrm{RC}}}$ and K_{RC} are hence find accordingly to:

$$\widehat{\boldsymbol{\beta}} = \arg \min_{\gamma_{0_{RC}}, K_{RC}} \left(-\ell\left(\boldsymbol{\theta}, \gamma_{0_{RC}}, K_{RC}, \varepsilon_1, \dots, \varepsilon_n\right)\right). \tag{3.14}$$

The *arg min* function return the points of the domain of the given function, at which the values are minimized; and it is implemented in the computational procedure iterative presented in section by means of the *fminunc* Matlab® solver.

3.4.2 Confidence intervals

A crucial component of statistical inference is confidence interval estimation, as it provides a measure of uncertainty in parameter estimates. In fact, confidence intervals provide a range of possible values within which the true parameter value can be expected to lie with a certain level of confidence.

Once the values of the Johanson model parameter were estimated as the iterative computational procedure comes to an end, their associated confidence interval must be computed. For this scope the Hessian matrix was used. This matrix was given as an output of the *fminunc* Matlab® solver once the function reaches an end. The Hessian matrix is a square matrix of second-order partial derivatives of the objective function, f :

$$\left(\mathbf{H}_f\right)_{i,j} = \frac{\partial^2 f}{\partial x_i \partial x_j}. \tag{3.15}$$

Applied to our parameter estimation and objective function it results:

$$\mathbf{H} = \begin{bmatrix} \frac{\partial^2(-\ell)}{\partial {\gamma_0}^2} & \frac{\partial^2(-\ell)}{\partial \gamma_0 \partial K} \\ \frac{\partial^2(-\ell)}{\partial \gamma_0 \partial K} & \frac{\partial^2(-\ell)}{\partial K^2} \end{bmatrix}. \tag{3.16}$$

The Hessian matrix provides important information about the behaviour of a function at a given point, and the Hessian matrix computed at the last iteration, that corresponded to the found minimum, was used to compute the standard errors. The inverse of this matrix, in fact, provides an estimate of the variance-covariance matrix, which contains the variance of the estimated parameters on the diagonal and their covariances off-diagonal (Greene, 2012). Taking the square root of the variances, the standard error *SE* of the parameters estimates was obtained:

$$SE = \sqrt{\mathrm{diag}\,(\mathbf{H}^{-1})}\,. \tag{3.17}$$

Once the standard errors were obtained, confidence intervals can be constructed using a chosen significance level, α. For all this Thesis, the significance level of 95% was chosen, being this value commonly chosen as a default value in most statistical analyses. Once the significance level is selected, the critical value, $t_{\alpha,n-2}$, was derived considering also the assumption of the specific distribution of the parameters. Not having large sample sizes from the RC experimental datasets, a *t*-student distribution whit *n-2* degree of freedom was adopted, where *n* is the number of observations and 2 represent the number of estimated parameters:

The 95% confidence intervals of the Johanson model parameters resulted:

$$\hat{\gamma}_0 - t_{\alpha,n-2}\, SE(\gamma_0) \leq \gamma_0 \leq \hat{\gamma}_0 + t_{\alpha,n-2}\, SE(\gamma_0)\,, \tag{3.18}$$

$$\hat{K} - t_{\alpha,n-2}\, SE(K) \leq K \leq \hat{K} + t_{\alpha,n-2}\, SE(K)\,. \tag{3.19}$$

3.5 Compactor simulator compression profile parameters

The relationship used to describe the behaviour of the ribblets SF as function of the exerted pressure was a power law function (2.15), like the approach suggested by Johanson (1964) to describe the compacted ribbons in the roller compactor. In this equation, two material-dependent parameters, ${\gamma_0}_{CS}$, K_{CS}, are present. To determine their values, calibration was necessary for each powder mixture based on experimental data obtained from the CS

The CS compression profile parameters were estimated using a method similar to that used for the Johanson model parameter. However, because the applied pressure was readily available, the calculating technique is simplified in this instance. As a result, parameter estimation required a simple fitting operation on a SF-pressure diagram. Figure 3.7 depicts the iterative computational technique used to estimate the CS compression profile parameters.

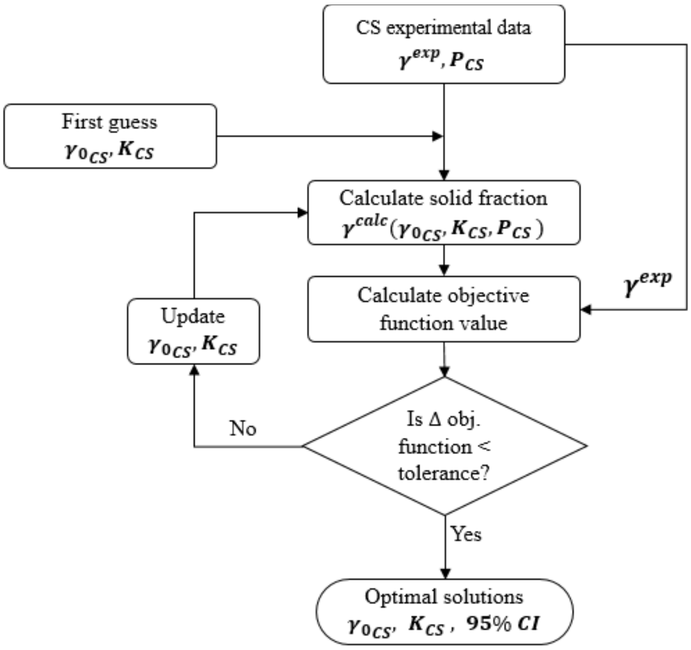

Figure 3.7. *Flow chart of the computational procedure for the estimation of the compactor simulator compression profile parameters.*

To start the iterative computational procedure, the experimental data of the SF and the corresponding applied pressure from the simulator were used as input. The procedure required an initial estimate of $\gamma_{0_{CS}}$ and K_{CS} to perform the first iteration. The objective function employed for the convergence of the iterative process was the same of the one used for estimating the Johanson model parameter, utilizing a MLE approach. The minimization function used is again the *fminunc* Matlab® solver, where the tolerance was set equal to 10^{-6}. Once the optimal value of $\gamma_{0_{CS}}$ and K_{CS} were estimated, their 95% confidence intervals were computed as described in Section §3.4.2, hence using the Hessian matrix that the *fminunc* Matlab® solver gave as output.

3.6 Proposed transfer methodology using mass correction factor

This section represents the core of this Thesis, in which the proposed transfer methodology is explained in detail. The term "transfer" refers to the process of establishing a relation between the two distinct compression profiles, allowing for the conversion of one into the other. The proposed method is based on the mass correction factor methodology, which effectively explains the differences between the pressure exerted by the compactor simulator and the one estimated for the roller compactor, as presented in Section §2.2.

The identified methodology consists of two major stages. Initially, during the development stage, the methodology was formulated and refined using historical datasets coming from RC and CS experimental campaigns, as depicted in Figure 3.8.

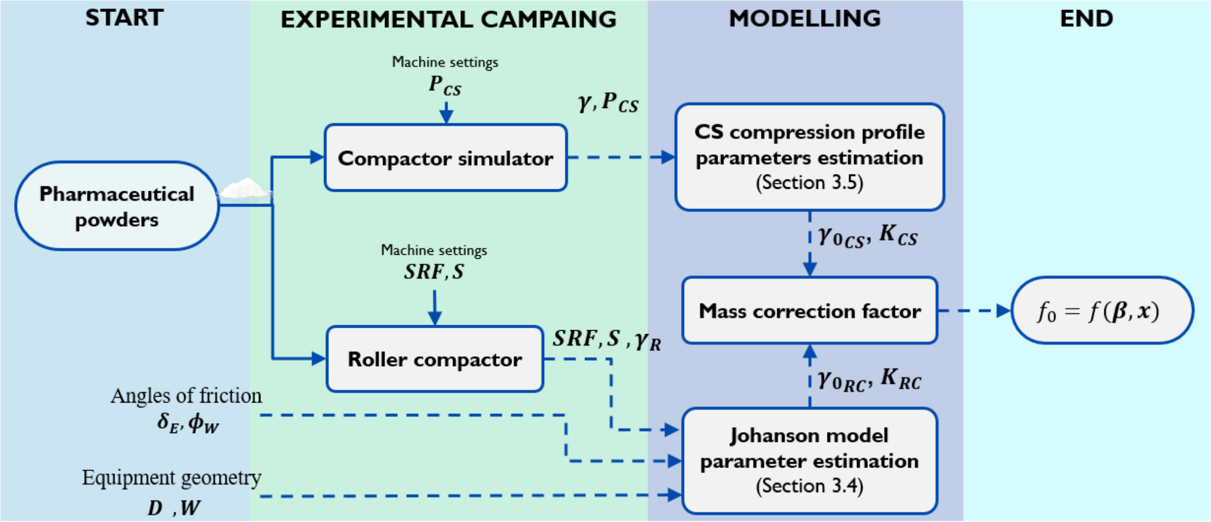

Figure 3.8. *Block flow diagram of the development procedure of the proposed transfer methodology.*

In this stage, which also includes a preliminary compression profile analysis, an understanding was achieved regarding how the pressure differences between the RC and CS compression profiles can be explained by the mass correction factor theory. Then, the proposed approach is built using the available experimental data, ensuring the development of a model that faithfully and comprehensively explains the observed phenomena. The development phase is composed by the calibration process and subsequent validation of the calibrated methodology. The execution of these two steps is explained in the following sections.

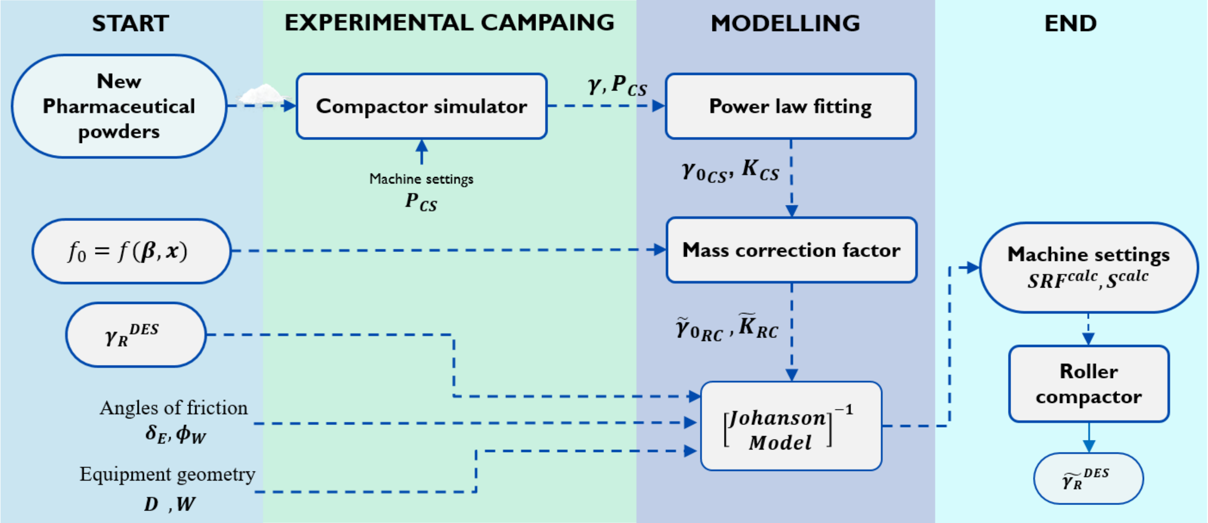

Figure 3.9. *Block flow diagram of the usage procedure of the transfer methodology for new pharmaceutical powder mixtures during development operations.*

Once the methodology has been developed, its application during the usage phase for new pharmaceutical powder mixtures under development, is depicted in Figure 3.9. In this scenario, conducting an experimental campaign solely on the CS is sufficient. Thanks to the previously developed transfer methodology, all the necessary information is obtained to characterize the material's compaction behaviour on the RC without requiring direct experiments on it. Through the information obtained, it is then possible to set the RC in the most optimal way to obtain the desired product.

3.6.1 Development stage

The development phase is visually represented through a block diagram in Figure 3.8. The available powder mixtures were tested on both the RC and the CS to develop the transfer methodology. On the CS, different SF values of the ribblets were obtained at various adjusted pressures to estimate the two compression profile parameters, ${\gamma_0}_{CS}$ and K_{CS}, for each powder blend, as described in Section §3.5. Similarly, the same materials were tested on the RC to obtain various SF values at various combinations of specific roller force and roll gap. The Johanson model parameter values, as explained in Section §3.4, were then determined for each material. With the ${\gamma_0}_{RC}$ and K_{RC} parameters available, the pressures exerted for each combination of machine parameters P_{max} were estimated, enabling the construction of RC compression profiles.

The mass correction factor theory, as explained in Section §2.2, can now be applied. This theory allows linking the different pressures of the two equipment to the same SF values. Specifically, the study was focused on determining the values of f_0 required to equalize the different pressures for each ribbon SF obtained during the experimental campaign on the RC. The objective was to develop a relation that utilizes the mass correction factor to explain the differences between the two compression profiles for all powder mixtures during calibration. Subsequently, the relation could be applied when only the CS compression profile will be available at the usage stage, thereby enabling the construction of a virtual RC compression profile. The term "virtual" is employed to denote the Johanson model constructed using the CS experimental data and the mass correction factor transfer methodology, rather than relying on the RC experimental results. As a result, a model describing the behaviour of this material on roll compaction can be established without the need for an experimental campaign on the RC. The final step of the development phase was to derive an algebraic expression for f_0 that established the relationship between P_{CS} and P_{max}. This expression was obtained through calibration using available datasets, and the remaining datasets was used for validation purposes.

3.6.2 Calibration

The starting point of the analysis is the construction of the compression profiles for all the powder mixtures for both RC and CS. These will be built after the parameters of the models, describing the behaviour of the powders compacted by different pieces of equipment, have been estimated, accordingly to Section §3.4 and §3.5. The obtained values of $\gamma_{0_{CS}}$, K_{CS} and P_{max}, together with the RC experimental ribbon SF measurements γ_R^{exp}, are used to perform the calibration of the mass correction factor transfer methodology. The flow diagram of the iterative procedure used for the calibration is reported in Figure 3.10.

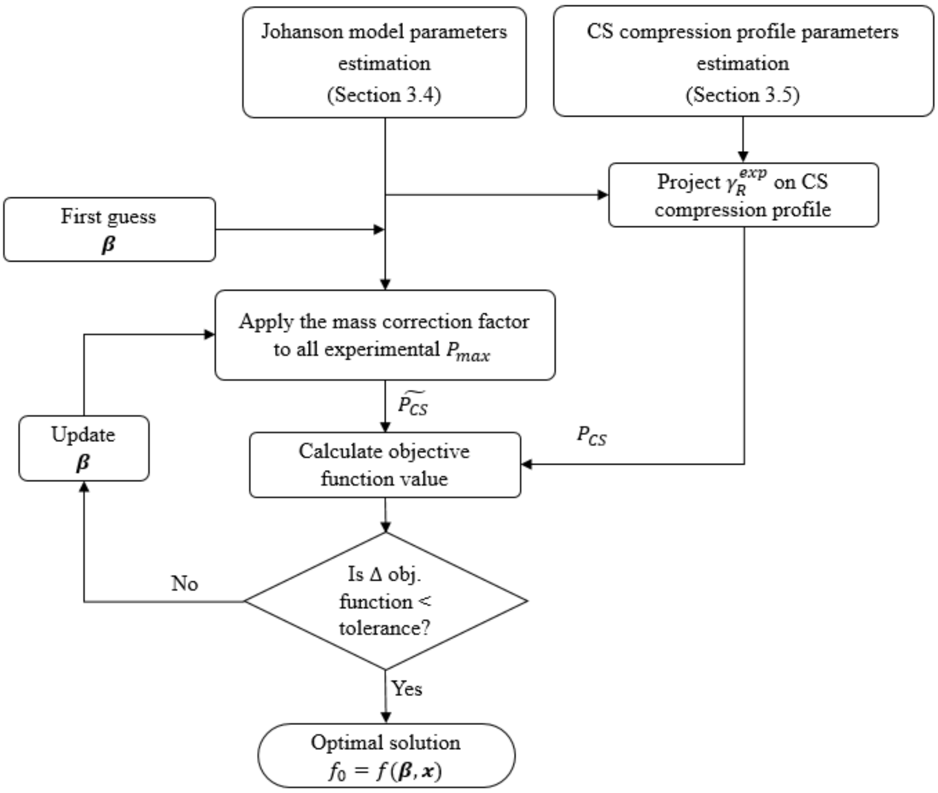

Figure 3.10. *Flow chart of the calibration iterative procedure to determine the optimal values of the parameters of transferring expression* $f_0 = f(\boldsymbol{\beta}, \boldsymbol{x})$

The calibration requires the definition of a function expressing f_0. In existing literature, f_0 have been expressed as a constant function $f_0 = const.$, which is independent of powder blend compositions, material properties and machine operating variables (Bi et al., 2014; So et al., 2021). The most suitable expression for f_0 will be designed based on the experimental results of this Thesis. At this stage, the expression will be represented just as $f_0 = f(\boldsymbol{\beta}, \boldsymbol{x})$, where $\boldsymbol{\beta}$ represents the vector of numerical parameters to be estimated during calibration, and $\boldsymbol{x}$ denotes the input variables, such as machine settings, that f_0 may depend on. To determine the pressure required for the CS to achieve the same relative densities for each measured ribbon SF, the values of $\gamma_{R,i}^{exp}$ are projected onto the CS compression profile by inverting (2.15):

$$P_{CS,i} = \left(\frac{\gamma_{R,i}^{exp}}{\gamma_{0_{CS}}}\right)^{K_{CS}} . \tag{3.20}$$

These represent the values of pressure on the simulator that the correction, using f_0 and starting from P_{max} , must achieve to obtain a perfect transfer. After that, the estimated pressure values exerted by the rolls P_{max} are corrected using the definition of f_0, (2.24):

$$\tilde{P}_{CS,i} = {f_0}^{K_{CS}}\, P_{max} \ . \qquad (3.21)$$

A visual representation of $\tilde{P}_{CS,i}$ and $P_{CS,i}$ is presented in Figure 3.11.

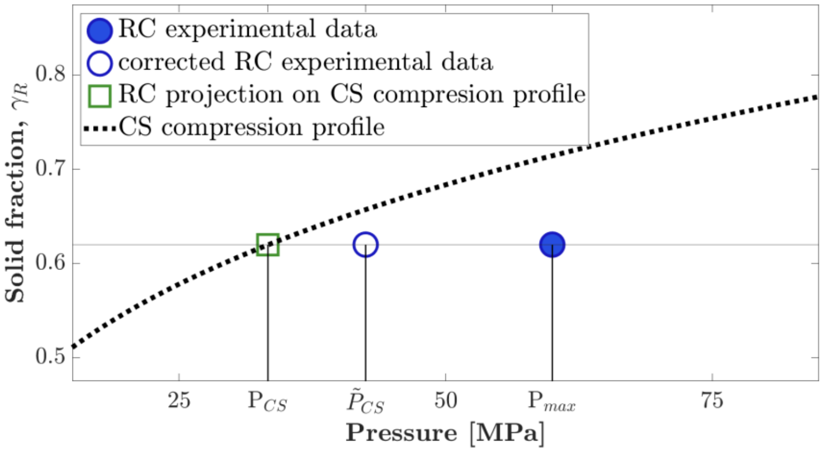

Figure 3.11. *Graphical representation of the pressure values used to perform the calibration.*

The objective is to achieve a transfer that results in the closest possible values of the calculated $\tilde{P}_{CS,i}$ to those of $P_{CS,i}$, thereby obtaining the closer overlapping between the corrected RC and CS compression profiles. An optimisation computational procedure is used to accomplish this, with the objective function, based on the MLE approach, that must be minimised:

$$-\ell(\boldsymbol{\theta}, \boldsymbol{\beta}, \varepsilon_1, \dots, \varepsilon_n) = +\frac{n}{2}\ln 2\pi\,\sigma^2 + \frac{1}{2\sigma^2}\sum_{i=1}^{n}(P_{CS,i} - \tilde{P}_{CS,i})^2 \ . \qquad (3.22)$$

The values of $\boldsymbol{\beta}$ obtained from this process represent the optimal expression of $f_0 = f(\boldsymbol{\beta}, \boldsymbol{x})$ for effectively transferring the RC and CS compression profiles of the calibration datasets. The optimization iterative procedure has been solved using the *fminunc* Matlab® solver.

3.6.3 Validation

Once the model has been calibrated and thus the function of f_0 has been numerically defined, the methodology can be validated using new datasets that were not part of the calibration datasets. Similarly to the calibration stage, also for the validation both RC and CS are required. The aim of the validation is to prove if and how effectively the calibrated methodology performs the transfer between the CS an RC compression profile for a new powder mixture. The validation procedures that have been adopted is depicted in Figure 3.12.

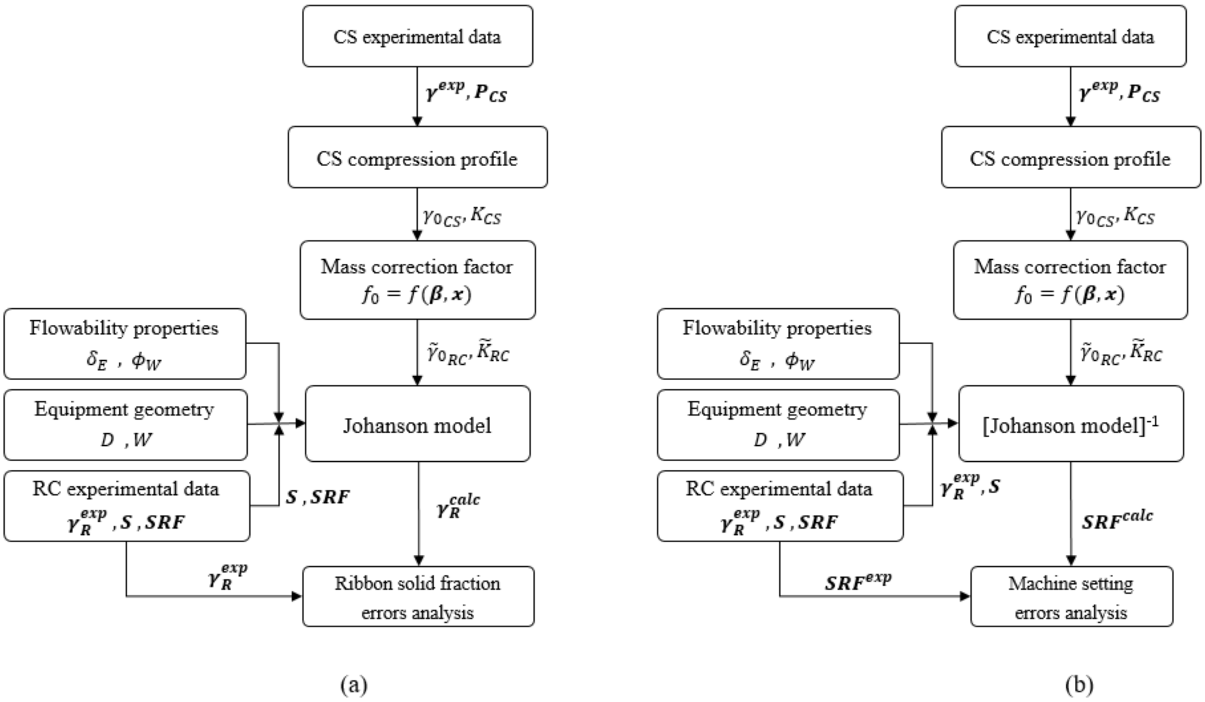

Figure 3.12. *Flow chart of validation procedures performed with respect to: (a) solid fraction; (b) machine settings.*

The initial step involves utilizing the dataset acquired during the experimental campaign on the CS to estimate the values of $\gamma_{0_{CS}}$ and K_{CS}. Using the calibrated expression of the mass correction factor and incorporating the obtained values of $\gamma_{0_{CS}}$ and K_{CS}, the virtual Johanson model parameters, namely $\tilde{\gamma}_{0_{RC}}$ and $\tilde{K}_{RC}$, are derived. Once the values of $\tilde{\gamma}_{0_{RC}}$ and $\tilde{K}_{RC}$ are obtained they can be utilized in two ways for validation purposes:

1. Ribbon solid fraction prediction: The machine setting combinations applied during the experimental campaign using the available RC dataset are incorporated into the Johanson model to calculate the predicted ribbon SFs γ_R^{calc}. Then these computed values are compared with the corresponding experimental values of γ_R^{exp} obtained using the same combinations of machine settings.
2. Machine settings prediction: The Johanson model is inverted and, using the γ_R^{exp} values, the values of the machine settings to be set to obtain the same SF are determined, according to the model with the $\tilde{\gamma}_{0_{RC}}$ and $\tilde{K}_{RC}$ parameters. As multiple combinations of specific roll forces and roll gaps can lead to same values of the ribbon SF, the roll gaps have been fixed to the experimentally implemented ones. Additionally, specific roller fractions are typically set to values with one decimal place. Therefore, the calculated values are rounded to the first significant figure to fit this practical constraint. Then, a comparison is made between the specific roll forces used in the experimental setup and the calculated ones.

3.6.4 Usage stage

If the developed model consistently demonstrates satisfactory and reliable performance across various powder mixtures, it can make a significant contribution to accelerating pharmaceutical tablet development. The application of the proposed transfer methodology during its usage stage is illustrated by the block flow diagram of Figure 3.9.

The investigation of a new pharmaceutical powder mixture will involve conducting an experimental campaign solely on the CS. The resulting experimental data will then be used to compute the values of ${\gamma_0}_{CS}$ and K_{CS}. The latter will be used in conjunction with the correlation of the mass correction factor developed during the development stage to obtain the virtual Johanson model parameter values. These estimated parameters will be incorporated into the inverted Johanson model to determine the optimal RC machine settings SRF^{calc}, S^{calc}, to be implemented to obtain the desired ribbon SF, as desired by the operators.

If the transfer methodology demonstrates its effectiveness and reliability, it has the potential to completely replace the need to conduct experimental campaigns on the roller compactor. This would lead to significant savings in terms of materials and costs required for these experimental campaigns, while also accelerating the overall characterisation and process modelling timeline.

Chapter 4

Results and discussion

4.1 Compression profile preliminary analysis

4.1.1 Roller compactor compression profiles

The Johanson model parameters were estimated for each powder mixture using the iterative computational procedure described in Section §3.4. All the measured ribbon SF samples of each roller compactor dataset were used for the estimation of the parameters.

Once the values of $\gamma_{0_{RC}}$ and K_{RC} are obtained, the pressure can be estimated for each experimental combination of roll gap and specific roll force, thereby linking it to the measured SF of the experimental ribbon. The estimated values of the Johanson model parameters for all powder blends in this case study, along with their associated 95% confidence intervals, are reported in Table 4.1. The values of the confidence intervals were computed following the procedure described in Section §3.4.2.

Table 4.1. *Johanson model parameters values and 95% confidence intervals of all the powder mixtures.*

Material	Pre-consolidation relative density, $\gamma_{0_{RC}}$ [-]		Compressibility constant, K_{RC} [-]	
	Value	**95% CI**	**Value**	**95% CI**
Formulation 1	0.345	0.039	6.054	0.992
Formulation 2	0.242	0.022	4.199	0.411
Formulation 3	0.198	0.016	3.475	0.250
Formulation 4	0.233	0.016	4.120	0.299
Compound A	0.267	0.026	4.599	0.523
Compound B	0.414	0.115	8.736	5.067
Compound C	0.410	0.066	6.314	1.904

Among the powder mixtures analyzed, Formulation 3, which is the placebo mixture with the highest MCC content, appears to be the most compressible, having the lowest K_{RC} value. In contrast, Formulation 1, which has a lower MCC content than the other placebo mixtures, shows the highest values among the placebo formulations. The estimated confidence intervals for placebo formulations and compounds A and C are narrow, hence the values of the associated Johanson parameter values can be considered attainable.

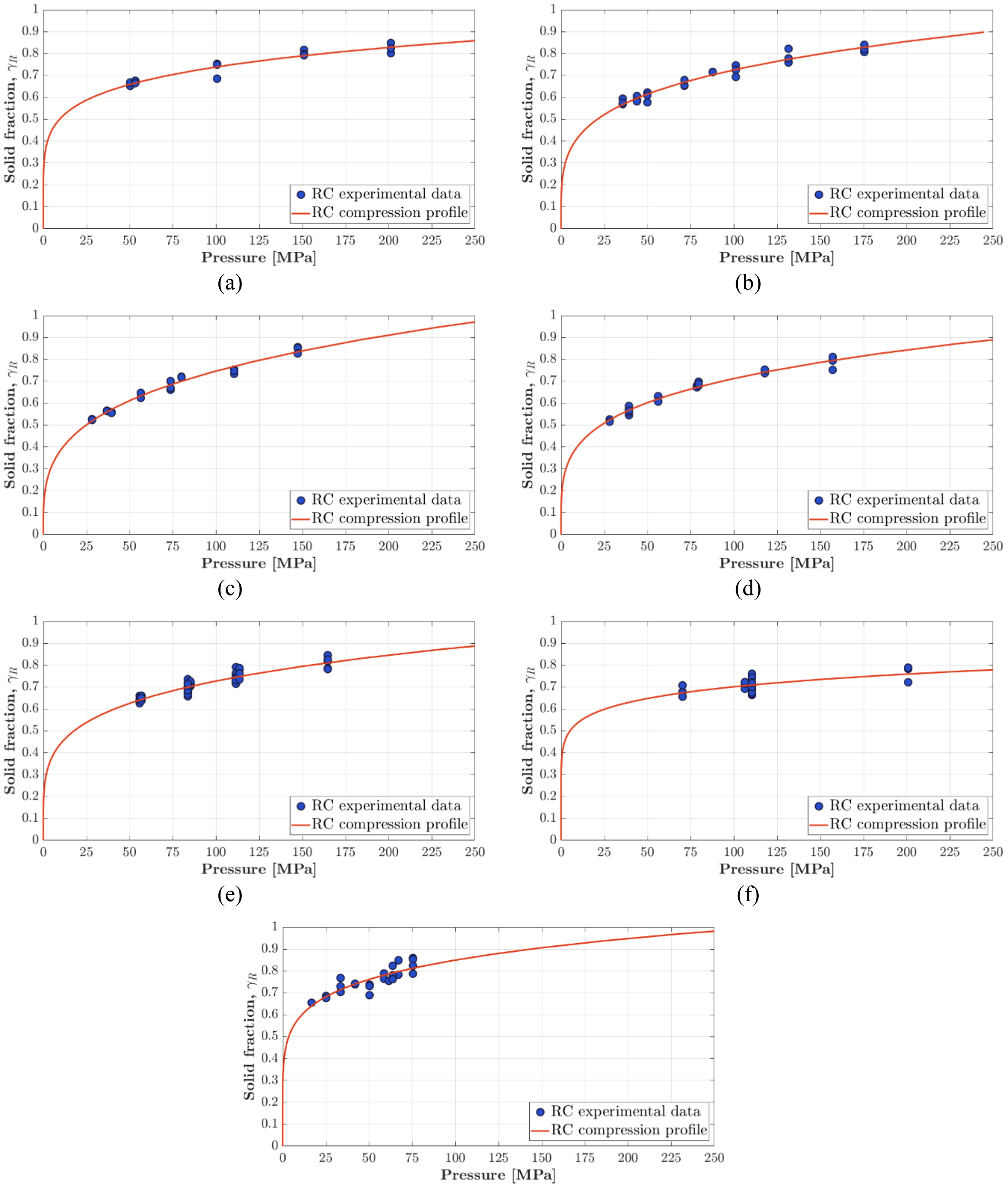

(a) (b) (c) (d) (e) (f) (g)

Figure 4.1. *Roller compactor compression profile (solid red line) built from experimental data (blue dots) for: (a) Formulation 1, (b) Formulation 2, (c) Formulation 3, (d) Formulation 4, (e) Compound A, (f) Compound B, (g) Compound C.*

Conversely, Compound B exhibits significantly wider confidence intervals in relation to the absolute values of the associated parameters. This indicates that the true value of the Johanson parameters for this powder blend is expected to lie in a broader range of values, making the estimated values of $\gamma_{0_{RC}}$ and K_{RC} affected by a stringer uncertainty.

Figure 4.1 illustrates the RC compression profiles for each powder mixture analyzed in this thesis, built utilizing the results presented in Table 4.1. The compression profiles of the analyzed powder mixtures exhibit significant differences. Among them, Formulation 3, which resulted to be the most compressible material, shows a steep curve describing the relationship between SF and applied pressure. On the other hand, Compound B, which presents the highest compressibility constant (always considering the confidence intervals), displays a flatter curve. This suggests that, for Compound B, achieving higher ribbon SFs requires higher pressures, resulting in the need for either higher specific roll forces or narrower roll gaps to be adjusted during roll compaction operations. A distinctive characteristic of compound C is its ability to achieve high ribbon SF even at low pressures, obtainable by setting low specific roller forces and high roll gaps. This phenomenon is mathematically represented by the higher values observed for its pre-exponential parameter $\gamma_{0_{RC}}$, as presented in Table 4.1.

Using the three SF measurements values associated with each experimental run, the intra-run sample variability values, in terms of SF standard deviation $\sigma_{intra-run}$, were calculated. Three samples were collected from distinct sections of the ribbon in order to consider SF gradients along the ribbon. The average values $\bar{\sigma}_{intra-run}$ were then computed for each powder mixture, except for Compound C for which the three intra-run sample missed. The results are shown in Table 4.2.

Table 4.2. *Intra-run sample variability.*

Material	$\bar{\sigma}_{intra-run}$ [−]
Formulation 1	0.018
Formulation 2	0.017
Formulation 3	0.008
Formulation 4	0.012
Compound A	0.011
Compound B	0.023
Compound C	N/A

Among the powder mixes, Compound B has the highest average intra-run variability value. This, coupled with the extremely high intra-run variability of the edge treatment levels, as shown in Figure 4.1.f, contributes to the significant uncertainty in estimating its parameters.

Finally, the goodness of fit of the Johanson model was assessed by estimating the R^2 values in calibration for each powder mixture. In addition, the mean absolute error (*MAE*) and mean relative error (*MRE*) in calibration, between the calculated and experimental ribbon SFs, were examined to assess the model capability to represent the roll compaction process. The maximum relative error, *max(RE)*, is another metric used in this Thesis to evaluate the performance of the models. This metric represents the highest value between the relative errors of measured and calculated values of the SF. Its relevance is heightened by GSK's setting of a critical threshold of 10%. Model diagnostic results are reported in Table 4.3

Table 4.3. *Johanson model diagnostic in calibration.*

Material	***MAE***	***MRE***	***max(RE)***	R^2
Formulation 1	0.013	1.8 %	7.9 %	92.6 %
Formulation 2	0.015	2.2 %	6.6 %	95.4 %
Formulation 3	0.014	2.1 %	4.7 %	97.6 %
Formulation 4	0.011	1.6 %	5.8 %	97.4 %
Compound A	0.016	2.2 %	6.4 %	83.1 %
Compound B	0.021	3.0 %	6.9 %	36.8 %
Compound C	0.024	3.1 %	10.6 %	70.6 %

The Johanson model demonstrates excellent results of the diagnostic parameter for the four placebo formulations. However, for the active powder blends, these values decrease due to the significant intra-run and process variability observed in the datasets from sample runs conducted at the same machine settings. This conclusion is also visible in Figure 4.1.e, 4.1.f and 4.1.g, where vertical clusters of experimental data at the same pressure values are present. Nevertheless, the relative and absolute errors of the SF still remain within acceptable values.

With the compressibility constant values established, the nip angle values for each powder mixture can be derived using (2.12). The resulting values, computed across different roll gaps, are reported in Table 4.4.

Table 4.4. *Computed values of the nip angles for each material at different values of the minimum roll gap.*

Material	α [°]		
	$S = 2\,mm$	$S = 3\,mm$	$S\ = 4\,mm$
Formulation 1	5.72	5.73	5.75
Formulation 2	5.10	5.11	5.13
Formulation 3	7.66	7.68	7.69
Formulation 4	11.61	11.63	11.65
Compound A	25.76	25.84	25.92
Compound B	10.48	10.51	10.54
Compound C	21.99	22.06	22.13

Additionally, the design space of each powder mixture can be explored when both Johanson model parameters have been retrieved. This allows understanding of how the SF varies with modifications across every potential combination of adjustable machine setting combinations. As a result, identifying the machine parameters required to produce a specified and desired ribbon relative density in accordance with the model becomes practicable. Figure 4.2 displays a visual representation of expected operating spaces for each powder blend using contour plots and surfaces plot.

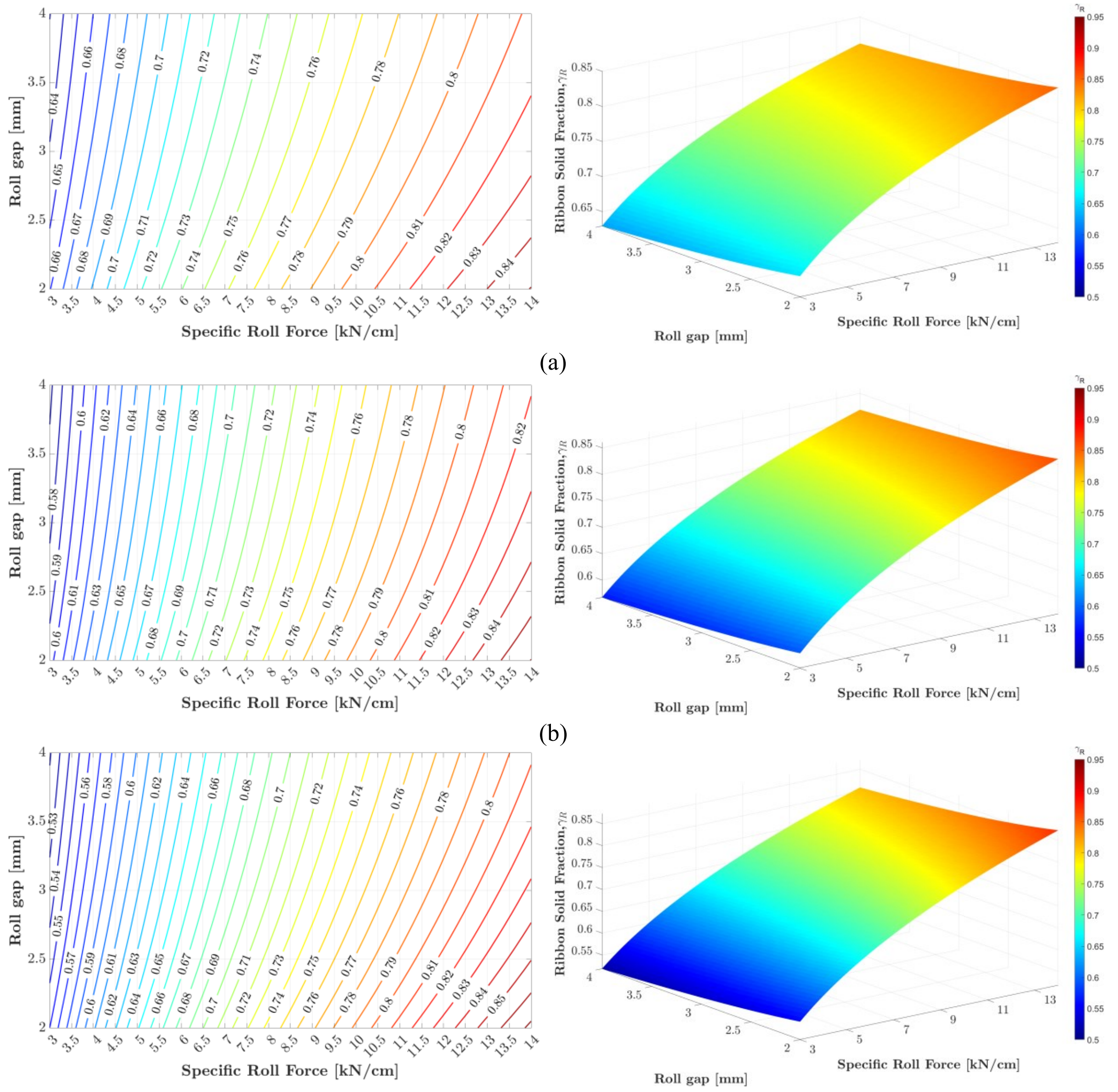

(a)

(b)

(c)

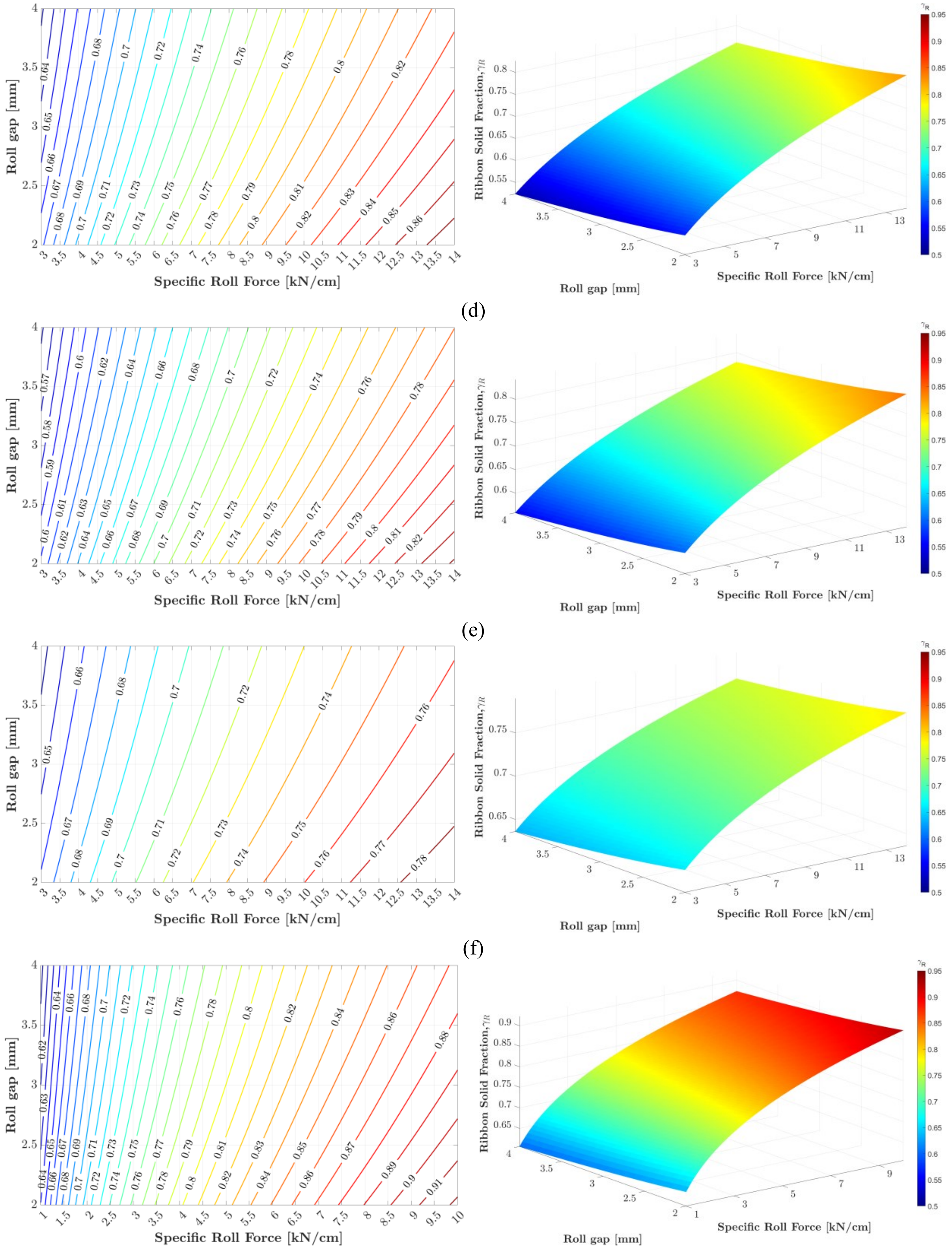

(d)

(e)

(f)

(g)

Figure 4.2. *Contour plots (left side) and 3D surface plots (right side) reporting predicted values of the ribbon solid fraction at different combinations of specific roll forces and minimum roll gap for: (a) Formulation 1, (b) Formulation 2, (c) Formulation 3, (d) Formulation 4, (e) Compound A, (f) Compound B, (g) Compound C.*

4.1.2 Compactor simulator compression profile

The values of $\gamma_{0_{CS}}$ and K_{CS} were estimated for all powder mixtures used in this Thesis by applying the iterative computational procedure described in Section §3.5. To assess potential variations caused by different pieces of equipment and diameter sizes, parameter estimation was conducted for each material CS dataset presented in Section §3.3. It is important to keep in mind that the initial two number digits within the dataset ID correspond to the diameter of the punches in millimetres. The resulting parameter values and 95% confidence intervals are reported in Table 4.5.

Table 4.5. *Compactor simulator compression profile parameters values and 95% confidence intervals of all the powder mixtures.*

Material	**Dataset ID**	**Pre-consolidation relative density, $\gamma_{0_{CS}}$ [-]**		**Compressibility constant, K_{CS} [-]**	
		Value	**95% CI**	**Value**	**95% CI**
Formulation 1	CS10-F1	0.422	0.017	7.449	0.495
Formulation 2	CS18-F2	0.358	0.015	5.973	0.325
	CS10-F2	0.335	0.007	5.250	0.136
Formulation 3	CS18-F3	0.326	0.013	5.340	0.262
	CS10-F3	0.286	0.007	4.547	0.118
Formulation 4	CS18-F4	0.336	0.014	5.611	0.286
	CS10-F4	0.325	0.011	5.295	0.229
Compound A	CS10-CA	0.363	0.014	6.090	0.322
	CS21-CA	0.343	0.017	5.354	0.397
Compound B	CS10-CB	0.389	0.018	6.632	0.445
	CS21-CB	0.370	0.178	6.239	4.965
Compound C	CS11-CC	0.486	0.009	7.835	0.263

Overall, the estimation of the $\gamma_{0_{CS}}$ and K_{CS} parameters is more accurate than those of the RC. In fact, the SF data more closely follow the empirical power law trend of the SF with respect the applied pressure. Furthermore, when different punch sizes are considered, the estimated parameter values of the same powder blend show small deviations. These discrepancies may arise from the differences in geometry, where different punches and filling chamber diameter, leads to distinct ratios between volumes and contact surfaces. Consequently, such differences could result in different wall effects between the two configurations. Also, such differences may be determined by different experimental pressure ranges taken into consideration. In fact, as the applied pressure approaches very high levels, the SF values tend to converge towards the value of 1, resulting in a flattened compression profile, hence an increase in the value of the compressibility constant. Figure 4.3 shows the compression profiles for each powder mixture dataset analyzed in this Thesis, built utilizing the results presented in Table 4.5.

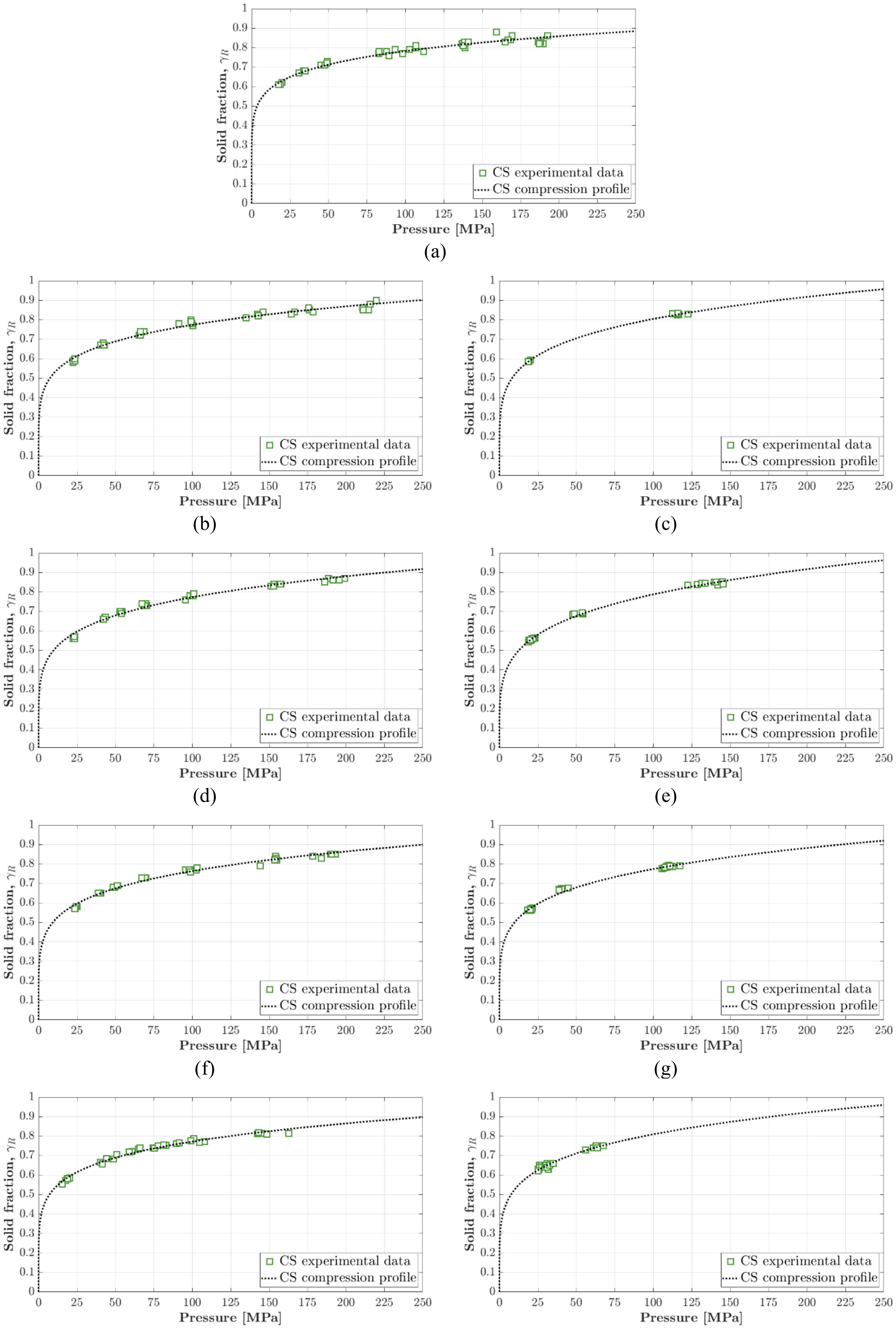
Solid fraction, γ_R
Pressure [MPa]
0
0.1
0.2
0.3
0.4
0.5
0.6
0.7
0.8
0.9
1
0
25
50
75
100
125
150
175
200
225
250
CS experimental data
CS compression profile

(a)

(b)

(c)

(d)

(e)

(f)

(g)

(h)

(i)

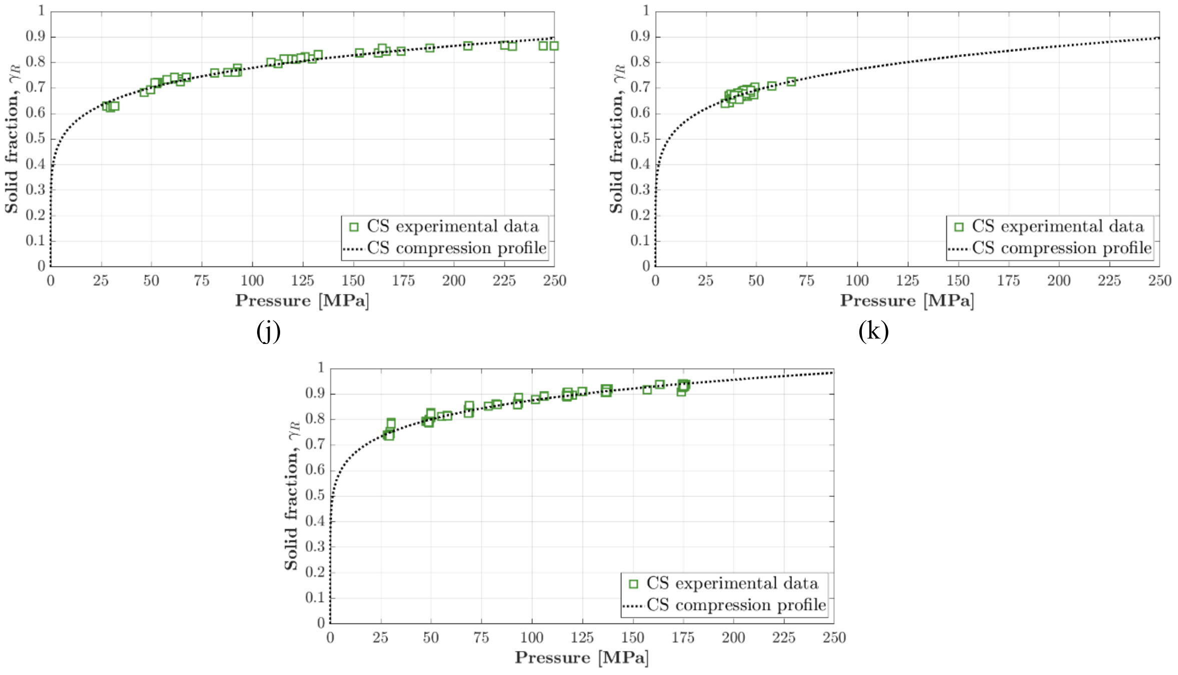

(j)

(k)

(l)

Figure 4.3. *Compactor simulator compression profile (dashed black line) and confidence built from experimental data (green empty dots) for all the dataset: (a) CS10-F1; (b) CS10-F2; (c) CS18-F2; (d) CS10-F3; (e) CS18-F3; (f) CS10-F4; (g) CS18-F4; (h) CS10-CA; (i) CS21-CA; (j) CS10-CB; (k) CS21-CB; (l) CS11-CC.*

Also, in the case of the CS compression profiles, the reported curves present significant differences among the different powder blends. However, it is worth to notice that the empirical relationship, i.e., the power law function, proposed by Johanson (1964) describes accurately the behaviour of the pharmaceutical powders that undergo compression. The estimation of $\gamma_{0_{CS}}$ and K_{CS} from the CS21-CB dataset yields a wide 95% confidence intervals, and this is because of the datapoint clustering due to the narrow pressure range explored during its experimental campaign.

4.1.3 Compression profiles comparison

The current objective is to investigate the differences between compression profiles derived from the CS and those obtained from the RC. From a mathematical perspective, this means comparing the different values of the values of γ_0 and K obtained from distinct pieces of equipment. To ensure consistency and comparability in this analysis, the CS dataset utilized in this comparison analysis were the ones obtained from the experimental campaigns performed on the Phoenix® with the 10mm tooling diameter. This specific piece of equipment was employed to investigate all the materials examined in this case study, with the exception of compound C. This approach enables us to make meaningful comparisons of compaction profiles, as we are considering datasets generated using the same piece of equipment, similar treatment levels, and identical punch sizes. Compound C is not taken into account at this stage because its CS dataset was obtained with a different piece of equipment and with different punches profile. Figure 4.4 shows the differences in the compression profiles observed for each of the powder mixtures.

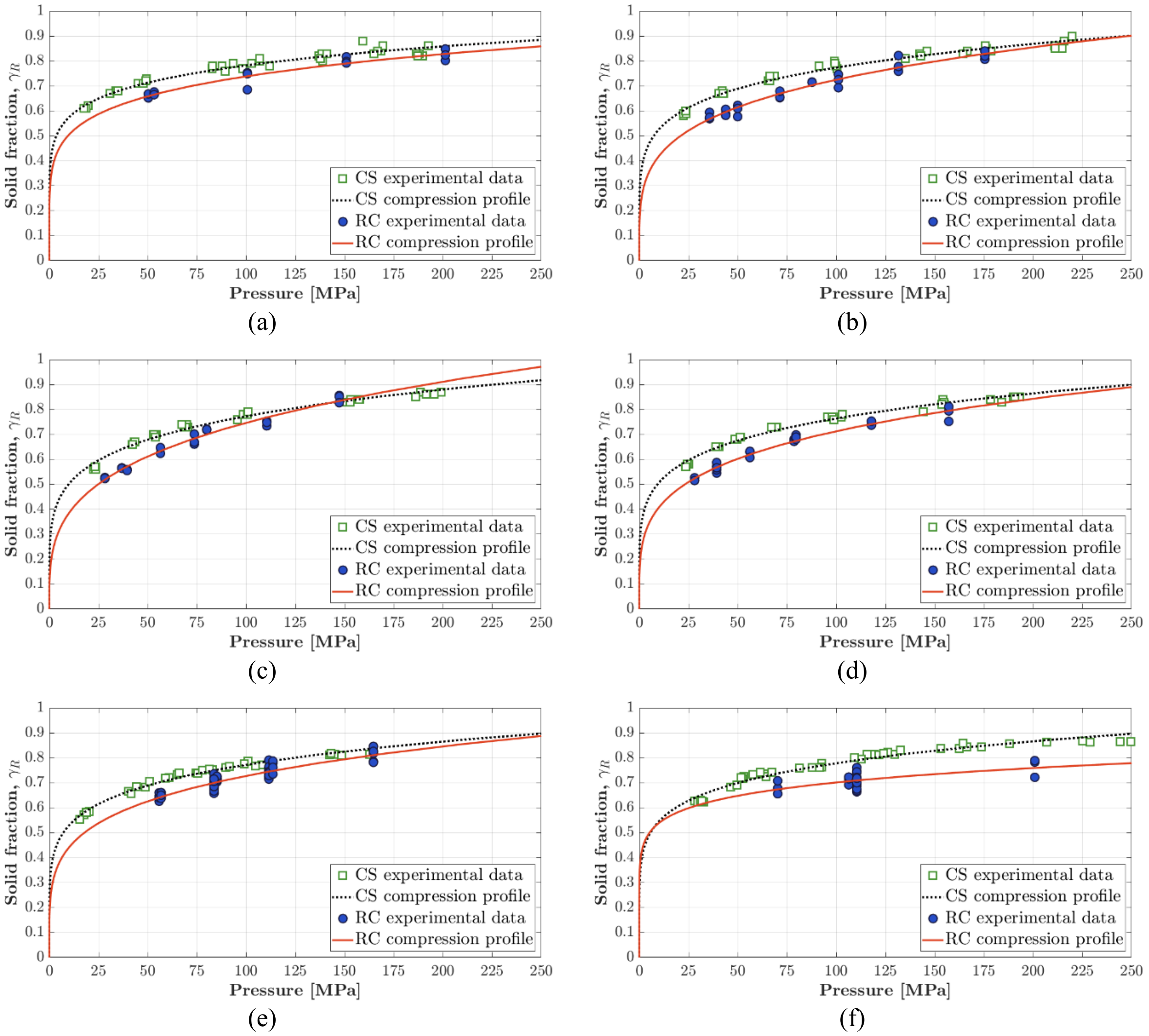

(a) (b)

(c) (d)

(e) (f)

Figure 4.4. *Comparison between RC and CS compression profiles for: (a) Formulation 1, (b) Formulation 2, (c) Formulation 3, (d) Formulation 4, (e) Compound A, (f) Compound B.*

The results show a consistent pattern across all seven powder blends: whatever the ribbon SF value, the compression profile constructed from the simulator consistently underestimates the pressure required for the same SF, in the RC. This finding aligns with the existing literature, which shows similar results (Reynolds et al., 2010; Toson et al., 2019). These differences can be mathematically explained by differences in the γ_0 and K values used to characterize the same powder mixture on the two pieces of equipment. To better visualize the numerical differences in the parameters, their values, along with the 95% confidence intervals, are graphically reported, for each powder blend, in Figure 4.5.

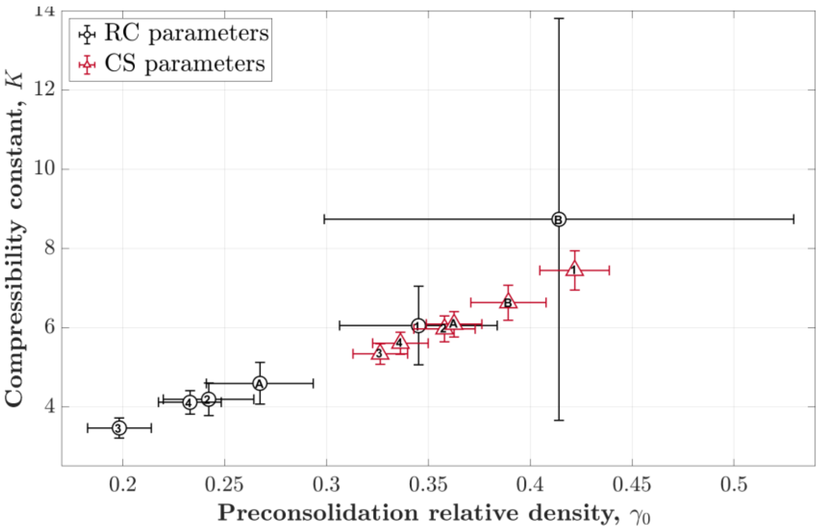

Figure 4.5. *γ_0 (x-axis) and K (y-axis) values estimated from the RC (black dots) and CS (red triangles). The number and the letter contained in the markers indicates the Formulation and the Compound ID respectively.*

The comparison of γ_0 and K values indicates that, with the exception of compound B, the compactor simulator estimates greater values for both parameters than the RC. Compound B exhibits a different behaviour in the compactor simulator where both γ_0 and K values are larger. However, it is important to highlight that compound B has extremely large confidence intervals, and most importantly much more uncertain. An interesting result from the comparative analysis of parameter values in Figure 4.4 is the particular sequence in which the parameters appear for each powder blend. Notably, if we consider a trend line that includes the data points for each piece of equipment, a significant congruence can be observed. Specifically, the sequence of parameters on the CS follows as: 3, 4, 2, A, 1, B; while the sequence of parameters on the RC is: 3, 4, 2, A, B, 1. The sole discrepancy is found in compound B; however, as previously mentioned, it exhibits criticality in the estimated parameter values.

Figures 4.4 and 4.5 show that the experimental results acquired from various pieces of compaction equipment differ significantly. Consequently, it is impractical to *directly employ* the estimated values of ${\gamma_0}_{CS}$ and K_{CS} to characterize a powder mixture *on the RC*. To support this claim, the Johanson model was applied to each powder mixture using parameters estimated by the simulator. The resulting diagnostic outcomes of these implemented models are displayed in Table 4.6.

It is evident that models calibrated with parameters estimated by the CS data are unsuitable for characterizing roll compaction operations of pharmaceutical powders. This holds true for all powder mixtures under analysis. In summary, this Section highlights that the transfer methodology that has to be employed ultimately must leads to lower values of ${\gamma_0}_{RC}$ and K_{RC} parameters compared to those obtained from the CS.

Table 4.6. *Johanson model diagnostic using values of γ_0 and K from the compactor simulator. Results are compared to the one obtained from RC experimental data in the brackets.*

Material	MEA	MRE	R^2
Formulation 1	0.057 (0.013)	7.9 % (1.8 %)	25.1 % (92.6 %)
Formulation 2	0.083 (0.015)	12.6 % (2.2 %)	0.8 % (95.4 %)
Formulation 3	0.083 (0.014)	13.5 % (2.1 %)	25.7 % (97.6 %)
Formulation 4	0.086 (0.011)	13.9 % (1.6 %)	0.5 % (97.4 %)
Compound A	0.068 (0.016)	9.7 % (2.2 %)	-137 % (83.1 %)
Compound B	0.064 (0.021)	9.1 % (3.0 %)	-367 % (36.8 %)

4.1.4 Mass correction factors analysis

Once both compression profiles from the two pieces of equipment are obtained, it becomes possible to determine the necessary mass correction factor values for transferring experimental data between them. In this process, all experimental data acquired from the RC are utilized. The pressure applied by the rollers P_{max} is available, as it was estimated during the Johanson parameter estimation. To estimate the pressure, that the simulator should apply to achieve the same SF, the data points from the RC are projected onto the compression profile of the CS. This mathematical projection involves inverting (2.24), as follow:

$$f_{0,i} = \left(\frac{P_{CS,i}}{P_{max,i}}\right)^{K_{CS}}, \tag{4.1}$$

where $f_{0,i}$ is the value of the mass correction factor of the i^{th} observation necessary to link the estimated pressure of the roll and the one projected on the simulator compression profile for the same i^{th} observation. The compressibility constant used in equation (4.1) is the one derived from the CS data. This selection is made because, when applying the transfer methodology using solely the experimental data from the CS, the compressibility constant from that specific dataset becomes the only available one. Figure 4.6 presents the diagrams where the values of $\ln(f_{0,i})$ for each powder mixture are plotted on the *y*-axis, while the *x*-axis represents the pressure exerted by the rolls, $\ln(P_{max})$.

The results shown in Figure 4.6 demonstrate that achieving a perfect transfer between the compression profiles of the RC and the CS requires applying correction values that follow an increasing trend with respect to pressure. However, this does not hold true for Compound B, as shown in Figure 4.6.f, where a decreasing trend is observed. Nevertheless, the computation of $f_{0,i}$ depends on the RC compression profile, which, in the case of Compound B, is characterised by strong uncertainty. As a result, the trends of $f_{0,i}$ are also affected by this uncertainty. Moreover, although with some differences, it seems that the straight line describing the upward trend of $f_{0,i}$ is common for all the powder mixtures under analysis.

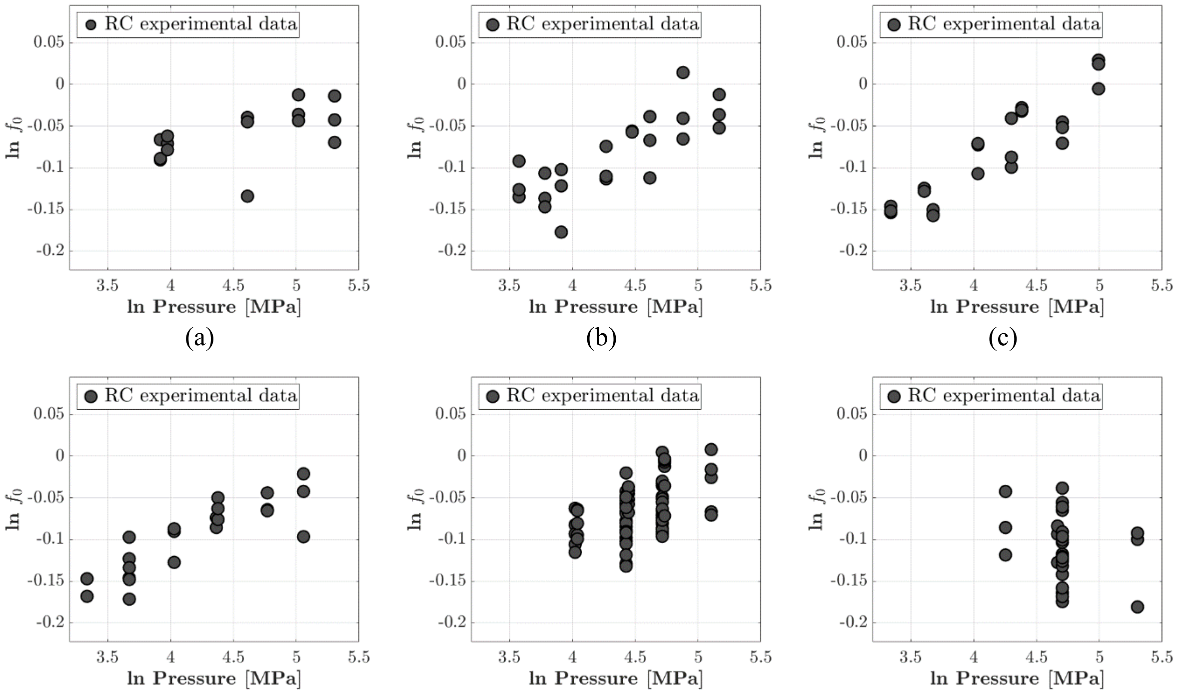

(a) (b) (c)

(d) (e) (f)

Figure 4.6. *Mass correction factor values estimated for each RC experimental data for: (a) Formulation 1; (b) Formulation 2, (c) Formulation 3, (d) Formulation 4, (e) Compound A, (f) Compound B.*

This finding contradicts the approach suggested by Bi et al. (2014) and So et al. (2021), who proposed using a *constant* value for the correction at any machine setting combinations, and hence at any pressure (Bi et al., 2014; So et al., 2021). The observed linear increase in this trend with applied pressure is physically reasonable. This is because the parameter f_0 represents the fraction of mass delivered at the minimum roll gap, which is influenced by particles velocity gradients. When higher pressure is applied by the rollers, the particles become less loose in the nip region. Consequently, a larger fraction of powder is transported from the nip angle to the minimum roll gap.

4.2 Placebo-based transfer model

4.2.1 Calibration

The initial focus on developing the proposed transfer mechanism was the identification of the specific CS and RC datasets. It was decided to create an initial model employing as calibration datasets the ones of the four placebo formulations, i.e., RC-F1, CS10-F1, RC-F2, CS10-F2, RC-F3, CS10-F3, RC-F4 and CS10-F4. or validation purposes, the datasets of the two active compounds, i.e., RC-CA, CS10-CA, RC-CB and CS10-CB, were used. This decision was made on purpose, to stress and properly test the transfer methodology limits. As explained in Section §3.1, excipients possess excellent flowability and compressibility properties, while the presence of APIs in the blends tends to compromise these properties. Therefore, if the model, calibrated based on the results from placebo formulations, manages to achieve satisfactory outcomes even for active mixtures, it would indicate an additional level of validation. As a result, the proposed methodology reliability and possible usefulness for future powder mixtures under development operations, will be strengthened.

The first stage in building the model entails choosing and creating an expression for the mass correction factor $f(\boldsymbol{\beta}, \boldsymbol{x})$, as discussed in Section §3.6.2. In light of the findings observed in Section §4.1.4, the selected methodology should formulate $\ln f_0$ as a linear function of the logarithm of the rolls pressure:

$$\ln f_0 = \beta_1 + \beta_2 \ln P_{max} \; , \tag{4.2}$$

where β_1 and β_2 represent the two coefficients to be estimated through calibration using experimental data. Their values must be determined to align the estimated pressure corrections for the RC as closely as possible with those for the CS, according to the calibration procedure discussed in Section §3.6.2. Importantly, it should be noted that the sets of experimental data points from the RC are not uniform across the four datasets. Specifically, during the experimental campaign for Formulation 1, five runs were executed, while Formulations 2, 3, and 4 each involved eight runs. each. Consequently, during calibration, the contribution of Formulation 1 to the calculation of the objective function (3.22) was weighted, i.e., multiplied by a coefficient, to make it comparable with the others. This approach guarantees that the incorporation of compression profiles from all formulations have equivalent significance in the model calibration process. Table 4.7 presents the calibrated values of the parameters of the mass correction factor expression, along with their corresponding 95% confidence intervals.

Table 4.7. *Parameters values and 95% confidence intervals of the mass correction factor linear expression for the place-based model.*

$\boldsymbol{\beta_1}$		$\boldsymbol{\beta_2}$	
Value	**95% CI**	**Value**	**95% CI**
-0.2481	0.068	0.0417	0.017

Furthermore, the correction of the RC pressure values of the experimental data, yielded using the calibrated values of β_1 and β_2, is visualized in Figure 4.7, where the corrected datapoints are represented by open dots.

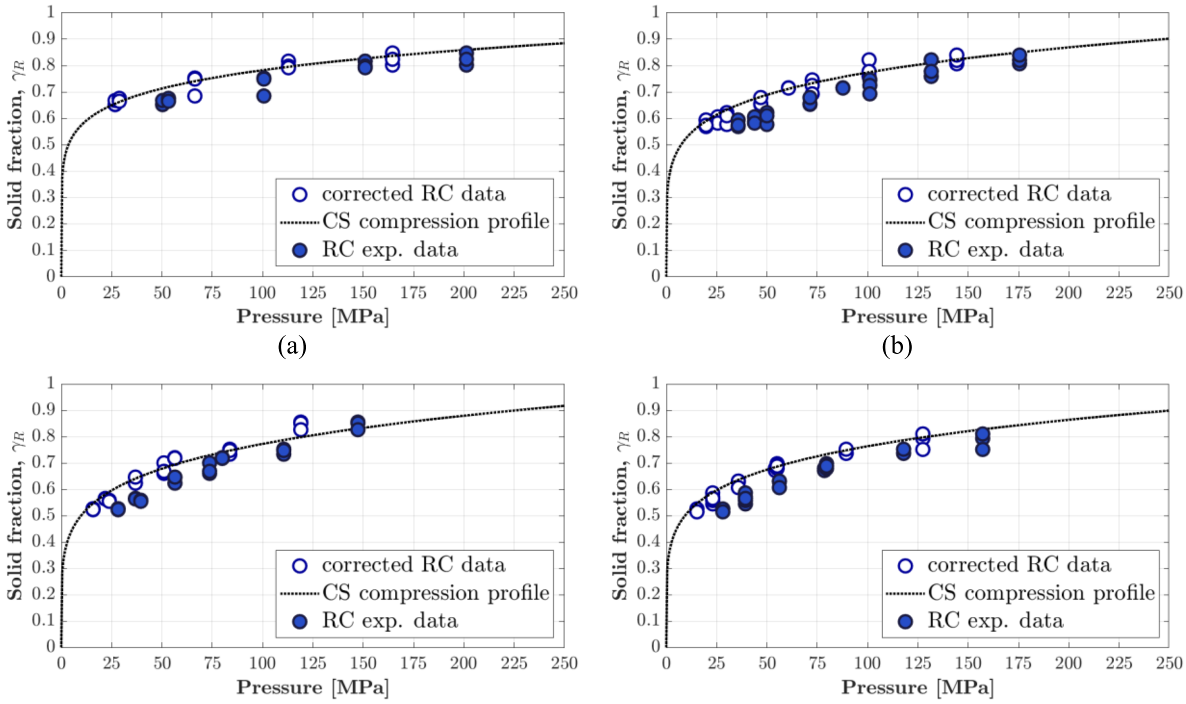

(a) (b)

(c) (d)

Figure 4.7. *Correction of the pressures of the RC experimental data resulting from the placebo-based model calibration for: (a) Formulation 1, (b) Formulation 2, (c) Formulation 3, (d) Formulation 4.*

The corrected pressure values demonstrate a remarkable similarity to the compression profiles generated by the compactor simulator. This consistency is noticeable for all four placebo formulations, highlighting the effectiveness of using a single expression for the mass correction factor. To numerically assess the differences observed during calibration, the mean absolute and relative errors, between pressures of the corrected RC data and their projection on the CS profiles, were computed for each formulation. These results are reported in Table 4.8.

Table 4.7. *Pressure mean absolute and relative errors in the placebo-based model calibration.*

Material	MAE [MPa]	MRE
Formulation 1	11.2	15.1 %
Formulation 2	8.3	18.0 %
Formulation 3	10.0	18.6 %
Formulation 4	5.9	17.6 %

Formulation 3 has larger pressure errors, which are mostly due to the negative influence of the data point at the upper treatment level. While the relative errors may appear significant, their impact on the calculation of the SF is relatively minor.

4.2.2 Validation

The validation of the calibrated model is presented, involving the use of Compounds A and B datasets. The procedure starts with the gathering of $\gamma_{0_{CS}}$ and K_{CS} values from the CS experimental data, as explained in Section §3.6.3. Their values are then employed to establish the virtual parameters of the Johanson model $\tilde{\gamma}_{0_{RC}}$ and $\widetilde{K}_{RC}$, using the calibrated relationship for the mass correction factor. Due to the formulation determined for $f_0 = f(\boldsymbol{\beta}, \boldsymbol{x})$, this step is straightforward. Starting from the relation defining the compression profile of the CS, it results:

$$\gamma = \gamma_{0_{CS}} P_{CS}^{1/K_{CS}} . \tag{4.3}$$

As discussed in Section §2.2, a relation is established between the pressure of the CS and that of the RC based on the definition of the mass factor. Combining (4.3) to (2.24), the SF can be expressed as function of the peak pressure exerted by the rolls:

$$\gamma = \gamma_{0_{CS}} \left(f_0^{K_{CS}} P_{max} \right)^{1/K_{CS}} . \tag{4.4}$$

Thanks to the linear expression formulated to express f_0, it is possible to rewrite (4.4) by integrating in it (4.2):

$$\gamma = \gamma_{0_{CS}} \left[\left(e^{\beta_1} P_{max}{}^{\beta_2} \right)^{K_{CS}} P_{max} \right]^{1/K_{CS}} . \tag{4.5}$$

Through a series of rearrangement and some algebra, it is possible to rewrite (4.5) as follows:

$$\gamma = \gamma_{0_{CS}} e^{\beta_1} \, P_{max}{}^{\frac{\beta_2 K_{CS}+1}{K_{CS}}} , \tag{4.6}$$

where the SF is described as a power law function of the peak pressure. This precisely represents the compression profile for the RC, where the pre-exponential term and the power factor are the virtual Johanson parameters, and they are as follows:

$$\tilde{\gamma}_{0_{RC}} = \gamma_{0_{CS}} e^{\beta_1} = 0.7803 \gamma_{0_{CS}} < \gamma_{0_{CS}} , \tag{4.7}$$

$$\widetilde{K}_{RC} = \frac{K_{CS}}{\beta_2 K_{CS} + 1} = \frac{K_{CS}}{0.0417 K_{CS} + 1} < K_{CS} . \tag{4.8}$$

Both (4.7) and (4.8) exhibit an important feature: the virtual Johanson model parameters that they yield are smaller than those acquired from the CS. This particular aspect is very crucial in achieving the greatest effectiveness of the compression profiles transfer. Had the relation suggested by Bi et al. (2014) (i.e., $f_0 = const.$), been utilized, and the same derivation process been followed, from (4.3) to (4.6), the resulting virtual Johanson model parameters would have been determined as follows:

$$\tilde{\gamma}_{0_{RC}} = const \cdot \gamma_{0_{CS}} , \tag{4.9}$$

$$\widetilde{K}_{RC} = K_{CS} . \tag{4.10}$$

In this instance, only the pre-consolidation relative density would be modified, while the compressibility constant of the CS would remain unchanged. However, such an approach would yield a suboptimal model, especially when dealing with highly compressible powder mixtures. The performance of the transfer methods can be evaluated throughout the validation after acquiring $\tilde{\gamma}_{0_{RC}}$ and $\tilde{K}_{RC}$ as per (4.7) and (4.8). This assessment investigates its capacity to predict both the SF and machine parameters. The predicted results will be compared to the actual outcomes obtained during the RC experimental campaigns. For a more detailed analysis of the results obtained, the validations will be presented separately for Compound A and Compound B.

4.2.2.1 Compound A

Section §4.1.2 reported the values of the 10 mm CS parameters $\gamma_{0_{CS}}$ and K_{CS} form Compound A, which yielded values of 0.280 and 4.815 for $\tilde{\gamma}_{0_{RC}}$ and $\tilde{K}_{RC}$, respectively. By utilizing these computed values along with all input data, as illustrated in Figure 3.12.a, the Johanson model is solved in its direct form. This procedure allows for the model to compute the calculated SFs γ_R^{calc}, for each combination of experimentally implemented machine parameters. The comparison between these calculated values, γ_R^{calc}, and their corresponding experimental counterparts, γ_R^{exp}, is carried out using the parity plot shown in Figure 4.8.a. The plot also includes error bands representing relative errors of 5% and 10%, enhancing the visualization of the datapoints distribution.

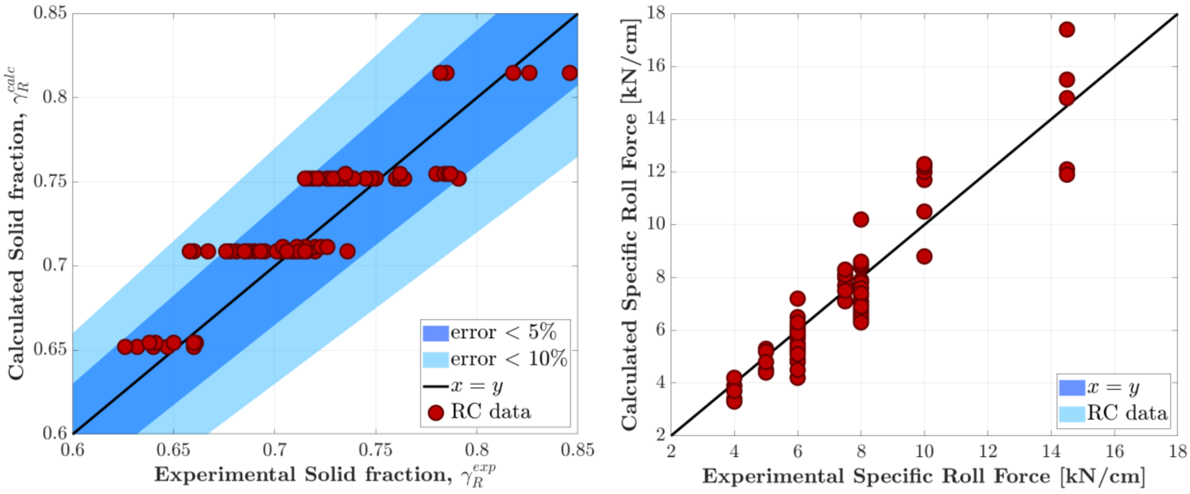

(a) (b)

Figure 4.8. *Validation parity for Compound A to evaluate differences between calculated and experimental: (a) ribbon solid fractions, (b) specific roll forces.*

The datapoints are distributed quite evenly, with positive errors counterbalanced by negative errors. Particularly, all errors are within the 10% relative error band's critical threshold. Among the eighty-seven datapoints, only five, constituting approximately 5.7% of the experimental data, display an error greater than 5%. The highest reported relative error is 7.4%. Furthermore, it is important to highlight the considerable variability observed in the measured SF values. Even when the same combination of machine parameters is used, resulting in identical calculated SFs, the measured values show significant variability. Based on these results, it can be concluded that the virtual Johanson model, which was developed primarily on the CS and transfer methods, accurately characterises the compaction behaviour of compound A on the RC. This conclusion is supported by the remarkable similarity between the diagnostic results of the virtual Johanson model and the Johanson model, as shown in Table 4.8.

Table 4.8. *Parameter values and diagnostic results of Virtual Johanson and Johanson model for Compound A.*

	Parameter values		***MAE***	***MRE***	***max (RE)***	R^2
	$\gamma_{0_{RC}}$	K_{RC}				
Johanson model	0.267	4.599	0.016	2.2 %	6.4 %	83.1 %
Virtual Johanson model	0.283	4.857	0.017	2.4 %	7.4 %	80.0 %

Figure 4.9 reports the compression profiles of both the virtual Johanson model and the Johanson model derived from experimental RC data.

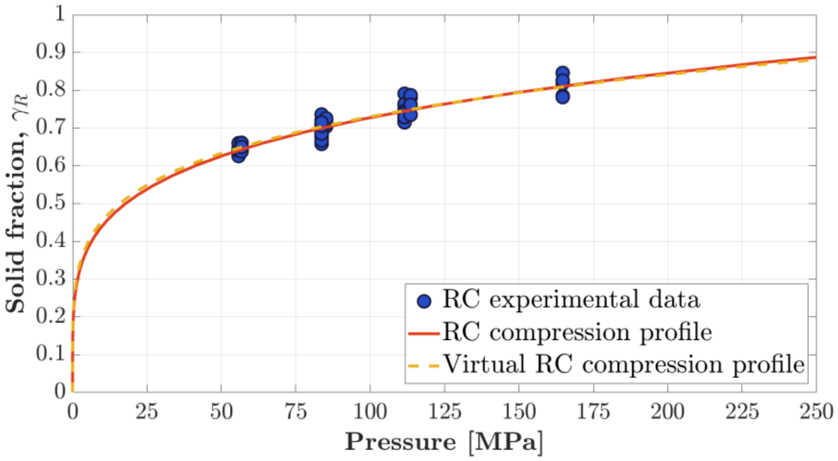

Figure 4.9. *RC and virtual RC compression profiles comparison for Compound A.*

The overlap of the two curves is almost complete and is due to the similarity between the parameters estimated by experimental data and the transfer methodology.

The validation method now involves predicting machine parameters, as detailed in Section §3.6.3 and illustrated in Figure 3.12.b. The input data in this scenario comes from the experimental RC dataset, which includes γ_R^{exp} values and the corresponding adjusted minimum roll gaps that were applied. The specific roll forces required to precisely produce the values of γ_R^{exp} are calculated by solving the inverse of the Johanson model using $\tilde{\gamma}_{0_{RC}}$ and $\widetilde{K}_{RC}$. Figure 4.8.b presents the parity plot displaying the comparison between the specific roll forces employed during experiments and those calculated. Once again, the datapoints exhibit an homogeneous distribution of both positive and negative errors. The mean absolute error between experimentally implemented and calculated specific roll forces is 0.80 kN/cm.

To summarise, the findings in this section highlight the greater accuracy of the prediction outcomes resulting from the proposed transfer methodology applied to Compound A. The application of this methodology at the usage stages would have successfully simulated this specific powder mixture without the requirement for an RC experimental campaign. Consequently 18 kg of material would have been saved, assuming 2.5 kg of powder blend for every 4 runs as reported by GSK. This huge amount becomes even more significant when considering the scarcity and cost of pharmaceutical compounds during their development stages.

4.2.2.2 Compound B

Section §4.1.2 reported the values of the 10 mm CS parameters $\gamma_{0_{CS}}$ and K_{CS} for Compound B, which yielded values of 0.298 and 5.100 for $\tilde{\gamma}_{0_{RC}}$ and $\tilde{K}_{RC}$, respectively. Both validation procedures are carried out and the results are reported in the parity plots in Figure 4.10.

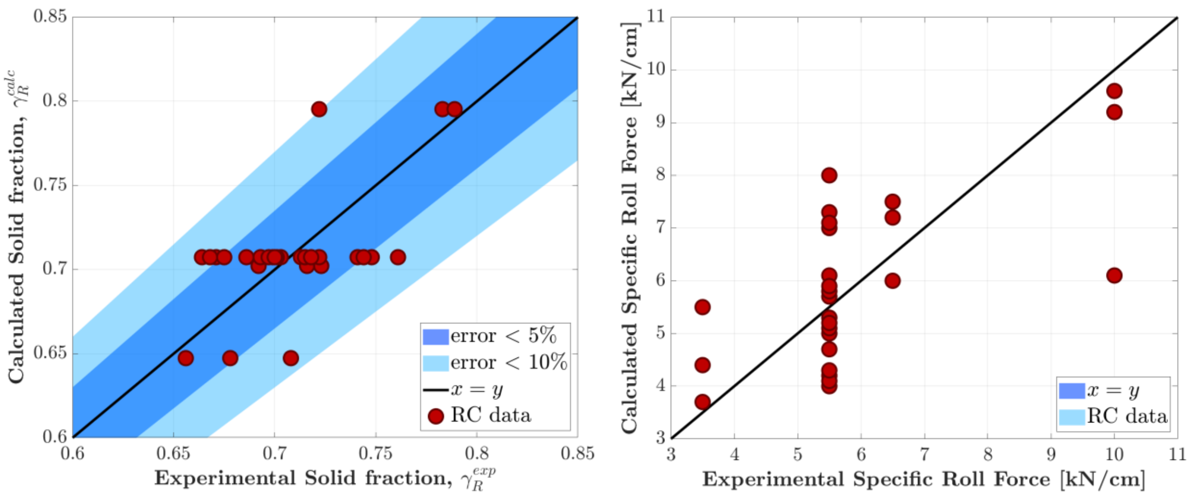

(a) (b)

Figure 4.10. *Validation parity for Compound A to evaluate differences between calculated and experimental: (a) ribbon solid fractions, (b) specific roll forces.*

As can be seen from Figure 4.10.a, one single data point exceeds the 10% threshold error band. While seven of the total thirty experiments, accounting for 23% of the dataset, have relative errors greater than 5%. This mismatch can be traced to both the inaccuracy of the developed virtual Johanson model and the significant variability inherent in the experimental campaign of Compound B, as reported in Table 4.2. Similarly, in the parity plot illustrated in Figure 4.10.b, which highlights the errors in specific roll forces, the model still demonstrates its capability to offer a reasonable prediction of the required machine parameters to achieve the targeted ribbon

SF. The average absolute error between experimental and estimated specific roll force measurements is equal to 0.94 kN/cm.

Table 4.9 summarises the parameters and diagnostic results of both the virtual Johanson models and those obtained from experimental data, similarly to the approach used for compound A.

Table 4.9. *Parameter values and diagnostic results of Virtual Johanson and Johanson model for Compound B.*

	Parameter values		***MAE***	***MRE***	***max (RE)***	R^2
	$\gamma_{0_{RC}}$	K_{RC}				
Johanson model	0.414	8.736	0.021	3.0 %	6.9 %	36.8 %
Virtual Johanson model	0.298	5.100	0.023	3.2 %	10.1 %	17.3 %

The discrepancy in parameter values is significant; however, the remaining outcomes of the model exhibit no excessive fluctuations. This is due to the high confidence interval values of Compound B parameter estimation. Figure 4.11 reports the compression profiles of both the virtual Johanson model and the Johanson model derived from experimental RC data.

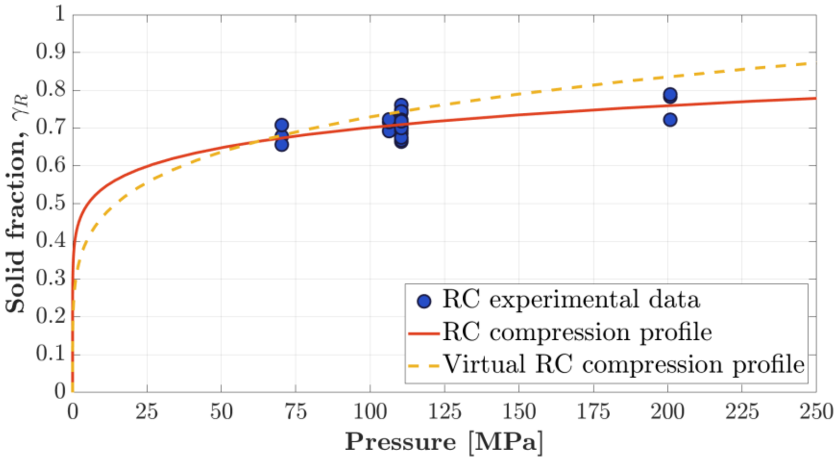

Figure 4.11. *RC and virtual RC compression profiles comparison for Compound B.*

Although the two compression profiles exhibit marked dissimilarities, both capture the compaction behaviour of Compound B on the RC. It's important to consider that the estimated pressure values, the x-axis, for each test point are influenced by the parameter K_{RC} utilized. Consequently, if the smaller K_{RC}, i.e., $\widetilde{K}_{RC}$ is employed, the RC datapoints in Figure 4.11 would shift leftward, aligning more closely with the compression profile of the virtual Johanson model.

From both Figure 4.10 and 4.11, another issue within the RC dataset of compound B is revealed. Specifically, two experimental points appear to be outliers. In fact, these datapoints, which are found at the higher and lower treatment levels, presents a SF of approximately 0.71 and 0.72, respectively. This is significant since the two treatment levels have radically different roller-specific forces, namely 3.5 and 10.0 kN/cm, while keeping the same minimum roll gap. If these two experiments, which are likely outliers, were excluded, the results of the transfer methodology would improve. In light of this, a scenario is presented wherein both the Johanson model and the validation of the virtual Johanson model are developed by omitting these two anomalous datapoints. The results are reported in Table 4.10.

Table 4.10. *Parameter values and diagnostic results of Virtual Johanson and Johanson model for Compound B, in the outlier exclusion scenario.*

	Parameter values		*MAE*	*MRE*	*max (RE)*	R^2
	$\gamma_{0_{RC}}$	K_{RC}				
Johanson model	0.343	6.223	0.019	2.6 %	6.8 %	49.3 %
Virtual Johanson model	0.298	5.100	0.020	2.8 %	7.1 %	46.6 %

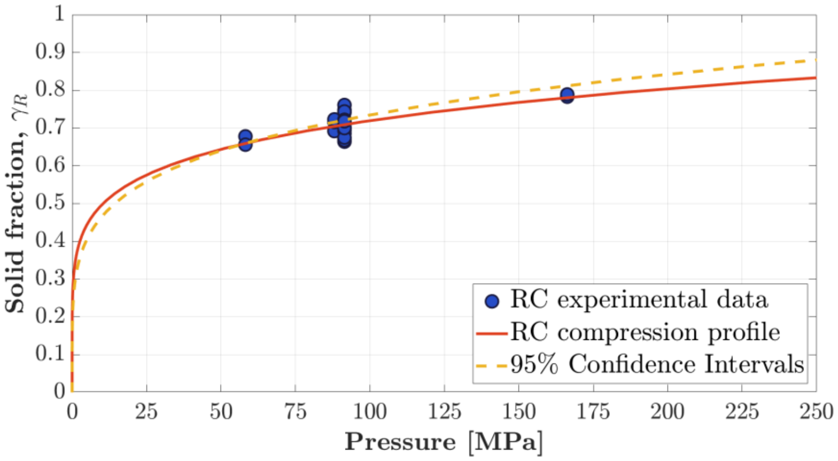

Figure 4.12. *RC and virtual RC compression profiles comparison for Compound B from which RC dataset the two presumed outliers have been removed.*

Table 4.10 and Figure 4.12 exemplify the impact of these two data points on the transfer outcomes. Even without excluding the two supposed outliers, the results of the transfer are decent and comparable with the Johanons model. But, by excluding them, a substantial improvement is experienced in the performance of the proposed transfer methodology.

In conclusion also for Compound B the proposed transfer methodology obtains accurate results in validation and would have been suitable for its implementation in its usage stage procedures. Just as observed with Compound A, in this particular scenario a total of around 6 kg of material may have been saved from the RC experimental campaign.

4.2.3 Validation using compactor simulator datasets with different diameters

With regard to each of the datasets analysed thus far, the transfer methodology demonstrated a remarkable level of accuracy. An analysis is now being conducted to determine how this methodology would perform when data from different datasets are used. In particular, the performance of the transfer methodology is investigated when "mixed datasets," i.e., datasets containing distinct experimental results from several compaction simulators (CS) with varying punch sizes, are used. These "mixed datasets" contain the same number of experiments as their 10 mm datasets counterparts. Within them, 50% of the observations are randomly selected from the 10 mm CS dataset, while the remaining 50% are drawn from either the 18 mm CS datasets (Formulations 2, 3, and 4) or the 21.8 mm CS dataset (Compounds A and B). This scenario was selected based on the practical experience gathered during the course of this Thesis project. It is not uncommon for experimental equipment to experience issues and become unavailable as a result. Different equipment layouts are frequently used, and having a model that can be applied to data coming from different instruments setup can provide additional value.

The validation processes presented in this Section are the same as those described in Section §3.6.3 and implemented in Section §4.2.2. The key difference is the use of different CS datasets as the initial points. As a result, the derived parameters $\gamma_{0_{CS}}$ and K_{CS} will differ intrinsically, resulting in differences in the Johanson virtual model parameters $\tilde{\gamma}_{0_{RC}}$ and $\tilde{K}_{RC}$. In this analysis for Compound B, the entirety of the RC dataset is incorporated into the validation process, without removing the two presumed outliers.

The model parameters and results are reported in Table 4.11, while the prediction errors for both the ribbon SF the specific roll force are shown graphically in Figure 4.13 as parity plots.

Table 4.11. *Parameter values and diagnostic results of Virtual Johanson and Johanson model using CS mixed datasets.*

Material		Parameter values		*MAE*	*MRE*	*max(RE)*	R^2
		$\gamma_{0_{RC}}$	K_{RC}				
Formulation 2	Johanson model	0.242	4.199	0.015	2.2 %	6.4 %	95.4 %
	Virtual Johanson model	0.283	4.810	0.015	2.3 %	7.0 %	94.7 %
Formulation 3	Johanson model	0.198	3.475	0.014	2.1 %	4.7 %	97.6 %
	Virtual Johanson model	0.231	3.977	0.018	2.7 %	4.8 %	96.0 %
Formulation 4	Johanson model	0.233	4.120	0.011	1.6 %	5.8 %	97.4 %
	Virtual Johanson model	0.264	4.564	0.024	4.0 %	9.4 %	89.6 %
Compound A	Johanson model	0.267	4.599	0.016	2.2 %	6..4 %	83.1 %
	Virtual Johanson model	0.291	4.984	0.019	2.7 %	8.2 %	74.6 %
Compound B	Johanson model	0.414	8.736	0.024	3.0 %	6.9 %	36.8 %
	Virtual Johanson model	0.288	4.924	0.024	3.3 %	9.8 %	8.7 %

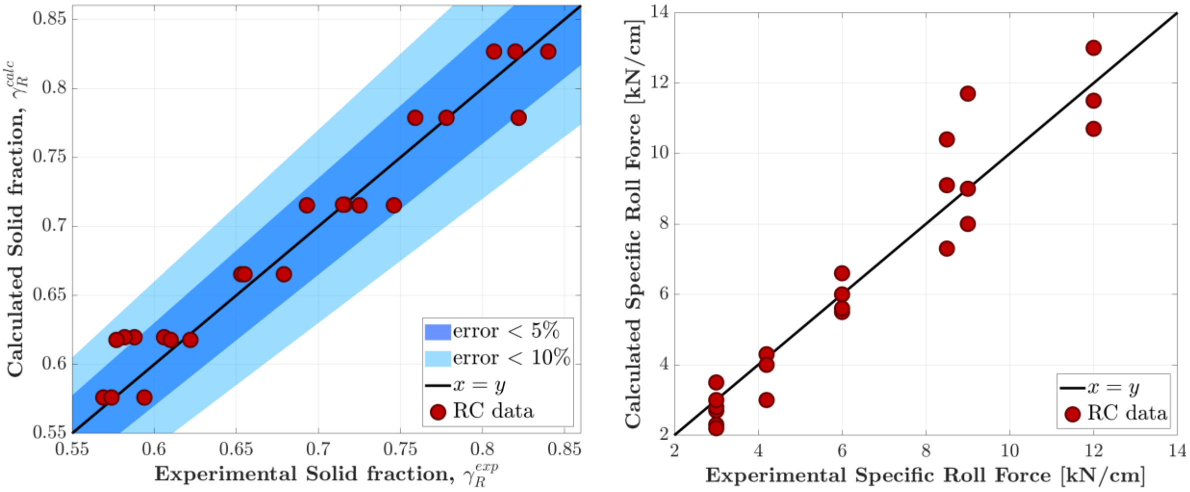
Calculated Solid fraction, γ_R^{calc}
Experimental Solid fraction, γ_R^{exp}
0.55
0.6
0.65
0.7
0.75
0.8
0.85
error < 5%
error < 10%
$x = y$
RC data
Calculated Specific Roll Force [kN/cm]
Experimental Specific Roll Force [kN/cm]
2
4
6
8
10
12
14
$x = y$
RC data

(a)

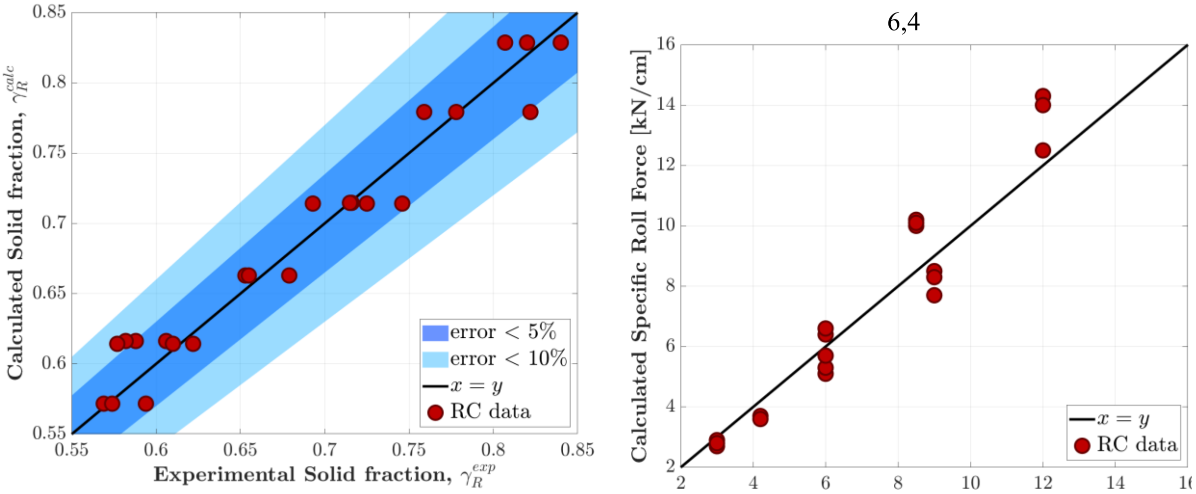
6,4
Calculated Solid fraction, γ_R^{calc}
Experimental Solid fraction, γ_R^{exp}
0.55
0.6
0.65
0.7
0.75
0.8
0.85
error < 5%
error < 10%
$x = y$
RC data
Calculated Specific Roll Force [kN/cm]
Experimental Specific Roll Force [kN/cm]
2
4
6
8
10
12
14
16
$x = y$
RC data

(b)

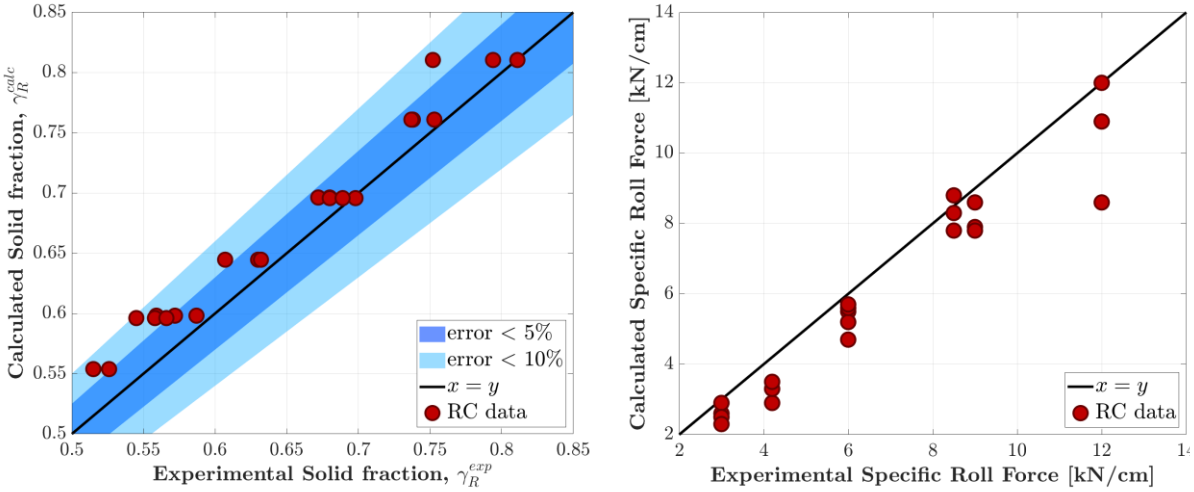
Calculated Solid fraction, γ_R^{calc}
Experimental Solid fraction, γ_R^{exp}
0.5
0.55
0.6
0.65
0.7
0.75
0.8
0.85
error < 5%
error < 10%
$x = y$
RC data
Calculated Specific Roll Force [kN/cm]
Experimental Specific Roll Force [kN/cm]
2
4
6
8
10
12
14
$x = y$
RC data

(c)

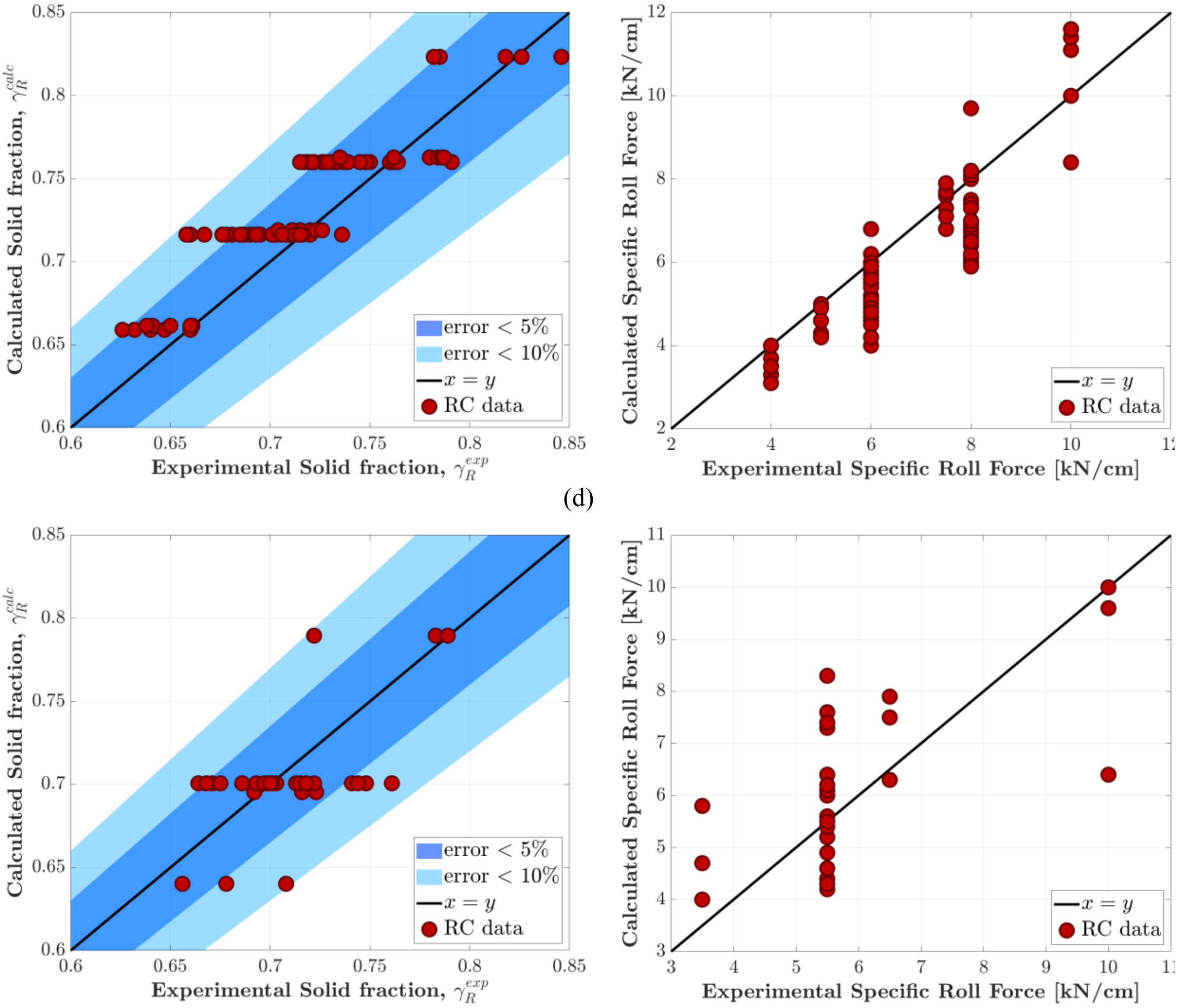

(d)

(e)

Figure 4.13. *Parity plots of the validation analysis performed utilizing CS mixed datasets of: (a) Formulation 2, (b) Formulation 3, (c) Formulation 4, (d) Compound A, (e) Compound B.*

The obtained transfer outcomes are really accurate over the entire variety of powder mixtures. However, in the case of Formulation 4 and the Compound A, there is a slightly decrease in performance where an heterogeneity of the error distributions can be noted in their parity plots. Such results were reasonably anticipated, as discussed in Section §4.1.2, where it was evident that the parameters $\gamma_{0_{CS}}$ and K_{CS} estimated using CS with varying diameters exhibited minimal disparity. Nonetheless, the results of our investigation clearly demonstrate that the proposed transfer methodology is still usable, although with some caution when working with data from other CS datasets.

This finding highlights a further advantage of the proposed transfer methodology, which contributes to its intrinsic value in line with its core objective of accelerating tablet production development stages. In circumstances where CS data might be scarce, the creation of a "mixed" dataset becomes a viable option, facilitating the augmentation of available data, broadening the experimental space and reducing the uncertainty associated with evaluated CS parameters.

4.3 Mix transfer model

A new model is introduced in consideration of the results demonstrated in the preceding section, where the effectiveness of the model calibrated using the four placebo formulations in the validation phase was established. This model was calibrated using all available powder mixes, with the exception of Compound C because of its criticalities. Following this approach, a model will be developed that includes calibration from six powder blends, allowing for an analysis of a wider variety of material characteristics. This will result in the achievement of a final transfer function that is simultaneously established across all powder blends, thereby obtaining the most optimal transfer possible for each. Inevitably, doing so will reduce the model's ability to describe the required transfer for placebo formulations. However, it is expected to improve performance when active formulations are taken into account.

The datasets employed for the calibration of this ultimate model are: RC-F1, CS10-F1, RC-F2, CS10-F2, RC-F3, CS10-F3, RC-F4, CS10-F4, RC-CA, CS10-CA, RC-CB and CS10-CB. The two presumed outliers of the RC Compound B dataset are removed in this analysis. Again, in light of the results presented in Figure 4.6, a linear function was utilised to express the mass correction factor in relation to the pressure exerted by the rollers. During the calibration phase, the influence of each powder mixture on the calculation of the objective function was weighed according to all the corresponding experimental data points, similarly to the placebo model. This ensured that the significance of each powder blend contribution was aligned, avoiding any undue impact from large RC datasets the one Compound A, with its eighty-seven experiments. The results of the calibration so performed are presented in Table 4.12, with the numerical values of the two parameters of the linear relationship and the respective confidence intervals.

Table 4.12. *Parameters values and 95% confidence intervals of the mass correction factor linear expression for the mix model.*

β_1		β_2	
Value	**95% CI**	**Value**	**95% CI**
-0.3015	0.044	0.0524	0.012

Furthermore, the correction of RC pressure values of the experimental data, yielded using these calibrated values of β_1 and β_2, is visualized in Figure 4.14, where the corrected datapoints are represented by empty dots.

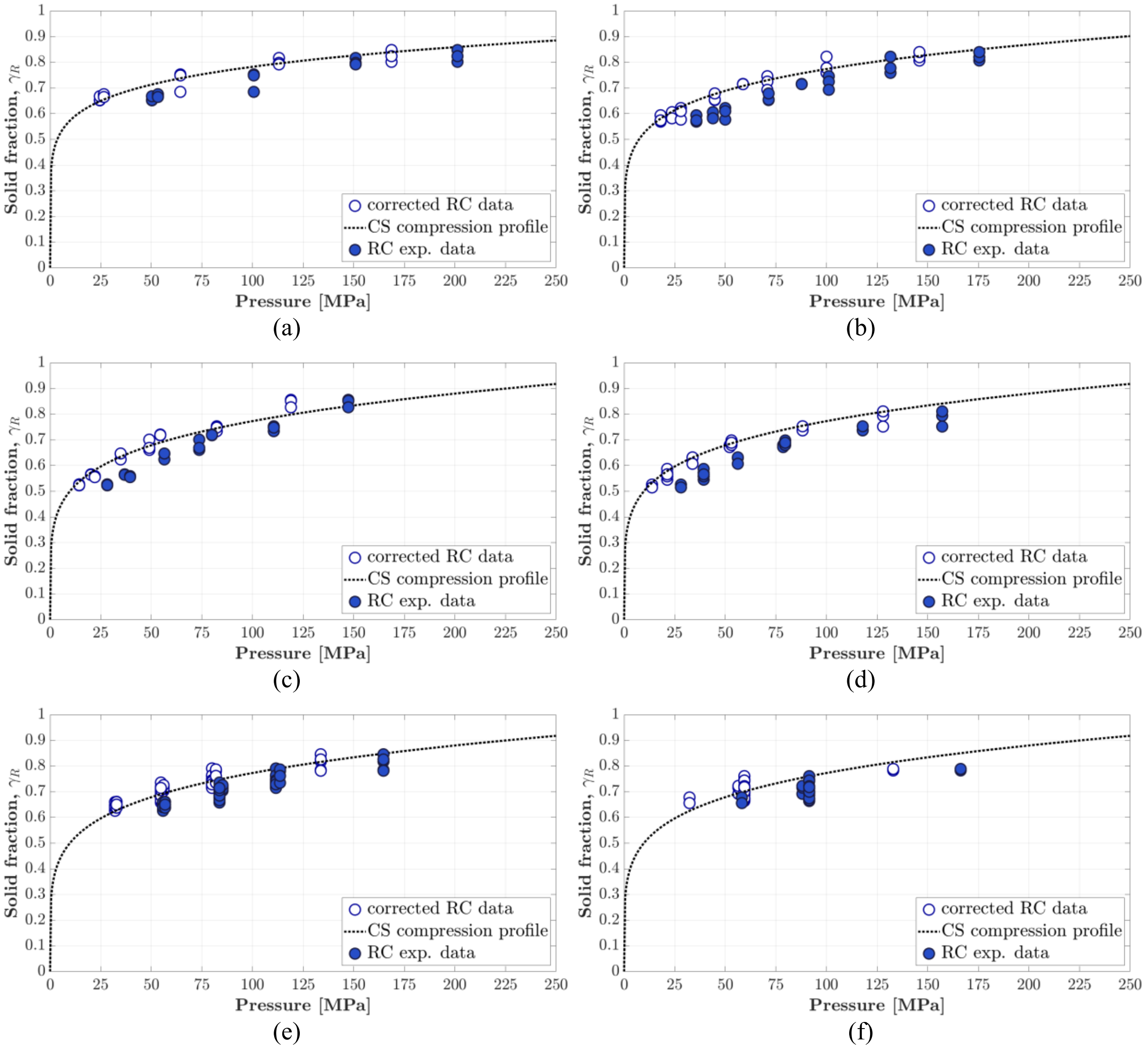

Figure 4.14. *Correction of the pressures of the RC experimental data resulting from the mix model calibration for: (a) Formulation 1, (b) Formulation 2, (c) Formulation 3, (d) Formulation 4, (e) Compound A, (f) Compound B.*

The model, in view of the reported MAE demonstrates to be effective for all the analysed powder mixtures. In conclusion the results reported in Table 4.12 represent the value of the linear function of f_0 proposed to be used in the future usage stage of the methodology, to retrieve the values of $\tilde{\gamma}_{0_{RC}}$ and $\widetilde{K}_{RC}$, starting from $\gamma_{0_{CS}}$ and K_{CS}, and applying (4.7) and (4.8). The corrected pressure values from the RC data show a remarkable closeness with the CS compression patterns. This notable agreement exists throughout the four placebo formulations and the two active compounds, demonstrating the effectiveness of using a single expression for the mass correction factor. Mean absolute and relative errors were computed for each material to quantify the differences observed during the calibration procedure between the pressures of the CS profile pressures and the ones of the corrected RC data. The results are reported in Table 4.13.

Table 4.7. *Pressure mean absolute and relative errors in the mix model calibration.*

Material	MAE [MPa]	MRE
Formulation 1	12.3	17.5 %
Formulation 2	7.6	14.9 %
Formulation 3	9.7	15.1 %
Formulation 4	5.0	12.9 %
Compound A	9.3	13.3 %
Compound B	12.3	22.9 %

4.4 Compound C analysis

As previously discussed, Compound C was excluded from the analysis in Section §4.2 due to the distinct nature of its available CS dataset, obtained from a different piece of equipment and employing varying pressure application modality. The objective of this section is to investigate the applicability and results of expanding the performed previous analysis to include Compound C as well. Compound C also stands out because of its distinctive attribute of containing a high API content (about 87% w/w). Pre-consolidation relative densities and compressibility constants for both RC and CS datasets have already been estimated and reported, as in Sections §4.1.1 and §4.1.2. The resulting compression profiles are together reported and in Figure 4.14.

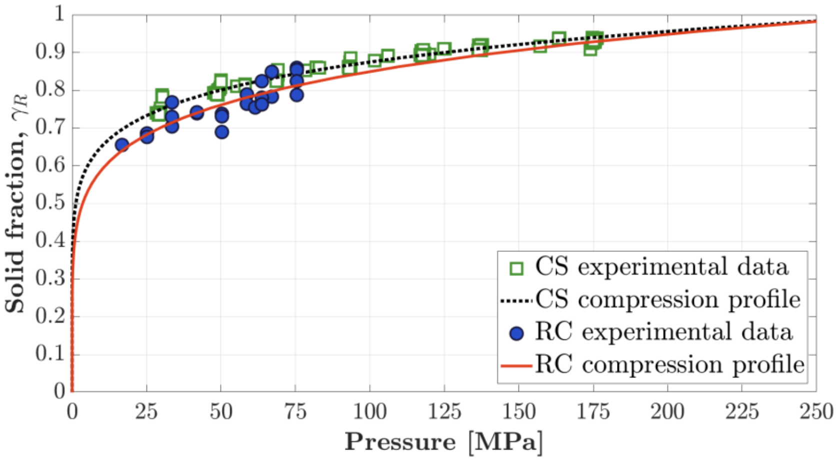

Figure 4.14. *Comparison between RC and CS compression profiles for Compound C.*

Again, the CS compression profile underestimates the pressure necessary to obtain the same ribbon solid fraction in comparison to the RC compression profile. In fact, both $\gamma_{0_{CS}}$ and K_{CS} present values greater compared to $\gamma_{0_{RC}}$ and K_{RC}. This result aligns with the findings from all other powder mixtures investigated in this Thesis, except for Compound B.

The investigation is now on establishing how the calibrated transfer methodology with all the materials applies to the experimental results obtained for Compound C. Employing (4.7) and (4.8), virtual Johanson parameter values of 0.360 and 5.567 are obtained, respectively. Subsequently, these values are utilized to solve the Johanson model, both directly and inversely, yielding calculated ribbon SF values and calculated specific roll forces. The resulting comparisons with the experimental ones are visually presented through parity plots in Figure 4.15.

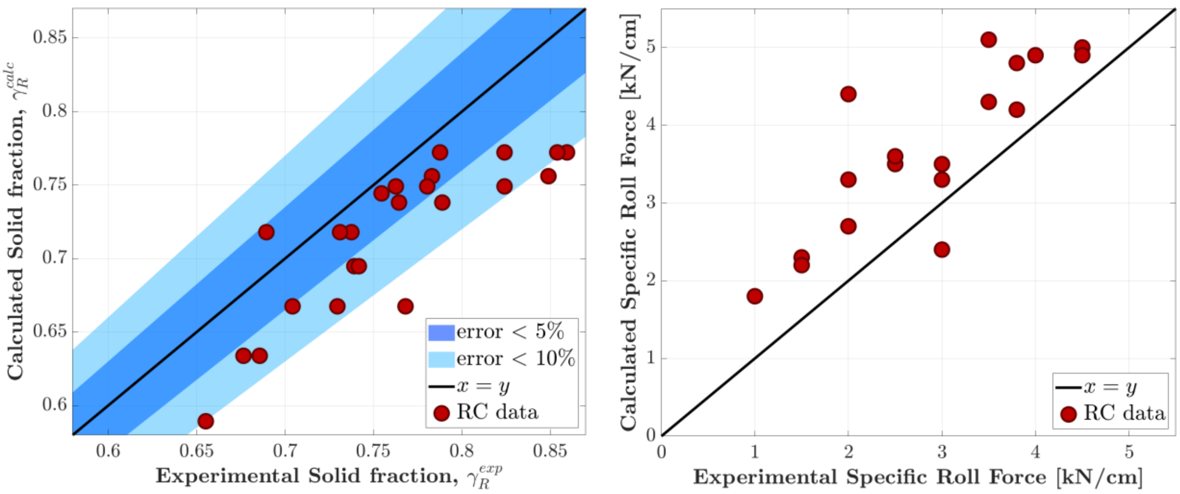

(a) (b)

Figure 4.15. *Validation parity for Compound C to evaluate differences between calculated and experimental: (a) ribbon solid fractions, (b) specific roll forces.*

The results are worse in this instance, where 14 datapoints, of the total 23, presents a relative error greater than 5%., while there are 4 datapoints with a relative error greater than 10. Additionally, the error distribution is skewed, with predominantly positive residuals, where γ_R^{exp} is greater than γ_R^{calc} for all cases except for one. These negative outcomes are also present in Figure 4.15.b, where machine parameter predictions fail to align precisely with the experimental ones and are not homogeneous distributed. The parameters and the diagnostic results of Johanson models employing virtual parameters and those derived from experimental data are presented in Table 4.12:

Table 4.12. *Parameter values and diagnostic results of Virtual Johanson and Johanson model for Compound C.*

	Parameter values		***MAE***	***MRE***	***max (RE)***	R^2
	$\gamma_{0_{RC}}$	K_{RC}				
Johanson model	0.410	6.314	0.024	3.1 %	10.6 %	70.6 %
Virtual Johanson model	0.360	5.567	0.046	6.0 %	13.0 %	7.8 %

Also the model diagnostic results of these two models differ significantly. This discrepancy is evident when the compression profiles of the Johanson and virtual models are compared visually in Figure 4.16.

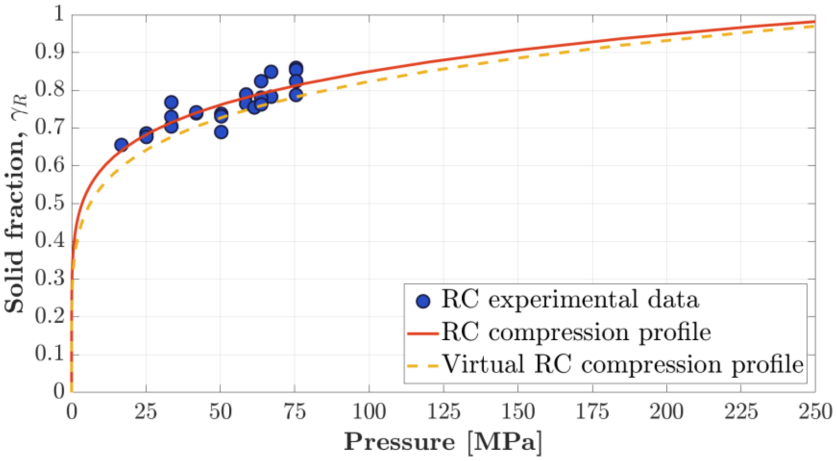

Figure 4.16. *RC and virtual RC compression profiles comparison for Compound C.*

The application of the transfer methodology to the CS curve yields a compression profile that consistently overestimates the pressure in comparison to the RC profile across the entire range of experimental pressures. Consequently, the SFs computed by the virtual Johanson model are predicted to be higher than the corresponding experimental values, as previously discussed.

Considering the entirety of the presented findings, the transfer methodology is not satisfactory and acceptable in the case of Compound C. The outcomes point to two potential reasons for Compound C anomalous performances. A possible reason could be the use of different piece of equipment for investigating the material compaction behaviour on the CS. Aside from the differences in machinery, the manner in which pressure was applied differs from previous procedures used to the material used to calibrate and validate the transfer model. Alternatively, the composition of Compound C might be the root cause. Compound C, in particular, has large API percentages, which could potentially lead to divergent flow properties and compaction behaviours. As a result, this instance needs the inclusion of alternate transfer model values in order to provide a more precise representation of this compound's characteristics.

Hence, in order to properly evaluate the aforementioned conclusions, an experimental campaign of Compound C on the Phoenix® CS with a 10 mm diameter and employing punch compression through a sinusoidal profile should be performed. Subsequently, the proposed and calibrated transfer methodology could be applied to these experimental outcomes. Following the suggested validation procedure, it could be possible to determine whether the results of the virtual Johanson model outperform the data shown in Table 4.12.

If the results improve, aligning more closely with the Johanson model derived from experimental data, a plausible inference could be drawn: the proposed transfer methodology is effective even for powder blends with high API content. However, it's noteworthy that the model would exhibits a degree of dependence on the specific instrumentation employed and the method of pressure application of the punches. Conversely, If the results remain unsatisfactory, an alternative conclusion could be drawn: the transfer methodology possesses inherent limitations attributed to material composition. As a result, its efficacy may be compromised when dealing with powder blends with increased APIs content.

4.5 Effect of composition on Johanson model parameter values

The final objective is to investigate how the composition of pharmacological blends can impact and, as a result, determine different values for Johanson model parameters. The materials selected for this aim are the four placebo formulations, each containing different weight fraction of MCC PH 102, Anhydrous Lactose, and Mannitol 200 SD. However, a limitation arises with Formulation 4, as it is the only blend containing mannitol, thereby precluding an assessment of how its content may impact the values of $\gamma_{0_{\mathrm{RC}}}$ and K_{RC}. Consequently, in order to conduct an exhaustive analysis, a literature search was conducted to source relevant data and results related to the same excipients. These data were collected from equivalent pharmaceutical grades to ensure consistency in material qualities, particularly in terms of average nominal diameter, which can affect compaction behaviour and flowability properties.

Pérez Gago et al. (2018) performed an experimental campaign carried out using the same Gerteis Mini-Pactor® on a placebo formulation made up entirely of Mannitol 200 SD. The design of the experimental campaign and the results are shown in Table 4.13 (Pérez Gago et al., 2018).

Table 4.13. *Results of the experimental campaign performed by Pérez Gago et al. (2018) for Mannitol 200 SD on the Gerteis Mini-Pactor®.*

Material	Specific roll force [kN/cm]	Roll gap [mm]	Solid fraction [-]
Mannitol 200 SD	4.0	1.5	0.723
	4.0	3.0	0.696
	4.0	1.5	0.718
	4.0	3.0	0.710
	8.0	1.5	0.779
	8.0	3.0	0.767
	8.0	1.5	0.757
	8.0	3.0	0.770
	6.0	2.25	0.756
	6.0	2.25	0.744
	6.0	2.25	0.755

Utilizing these experimental data and the parameter estimation procedure of Section §3.4, the values of the Johanson model parameters, which are $\gamma_{0_{\mathrm{RC}}} = 0.468 \pm 0.068$ and $K_{RC} =$

10.44 ± 3.694, were estimated. Furthermore, based on the findings of Patel et al. (2010), the value of the compressibility constant for MCC PH 102 was calculated and equal to $K_{RC} = 3.1$. Hence, a fairly detailed demonstration of the effect of different excipient composition on the estimation of Johanson parameters can now be developed. The initial step was to examine at a binary excipient blend, specifically MCC PH 102 and Anhydrous Lactose. Figure 4.17 shows the values of $\gamma_{0_{RC}}$ and K_{RC}, along with their respective confidence intervals, as function of the weight fraction of the lactose in the blends.

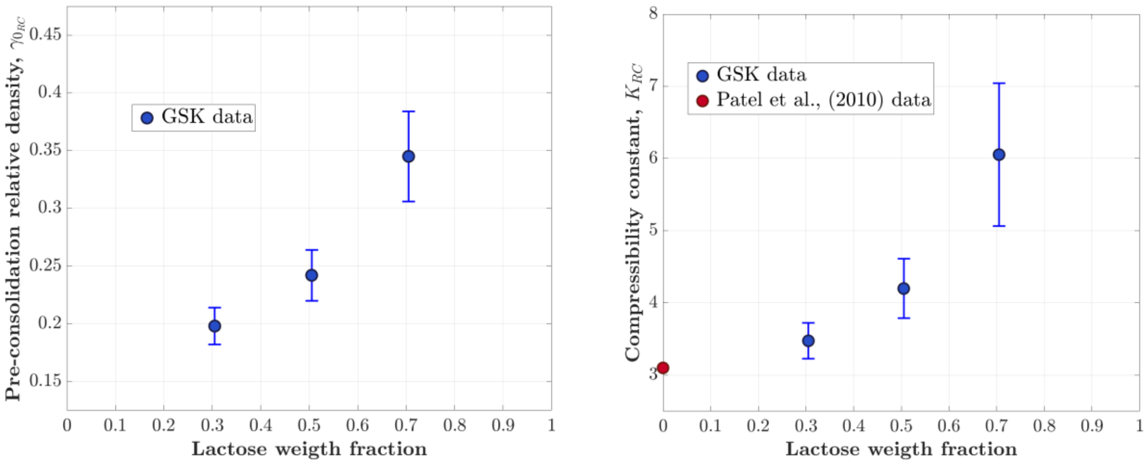

(a) (b)

Figure 4.17. *Effect of the blends composition, in the binary placebo formulation of MCC and anhydrous lactose, on the Johanson parameter values: (a)* $\gamma_{0_{RC}}$*, (b)* K_{RC}*.*

Similarly, in Figure 4.18, the values of the parameters $\gamma_{0_{RC}}$ and K_{RC}, as the weight fraction of mannitol varies with respect to the MCC.

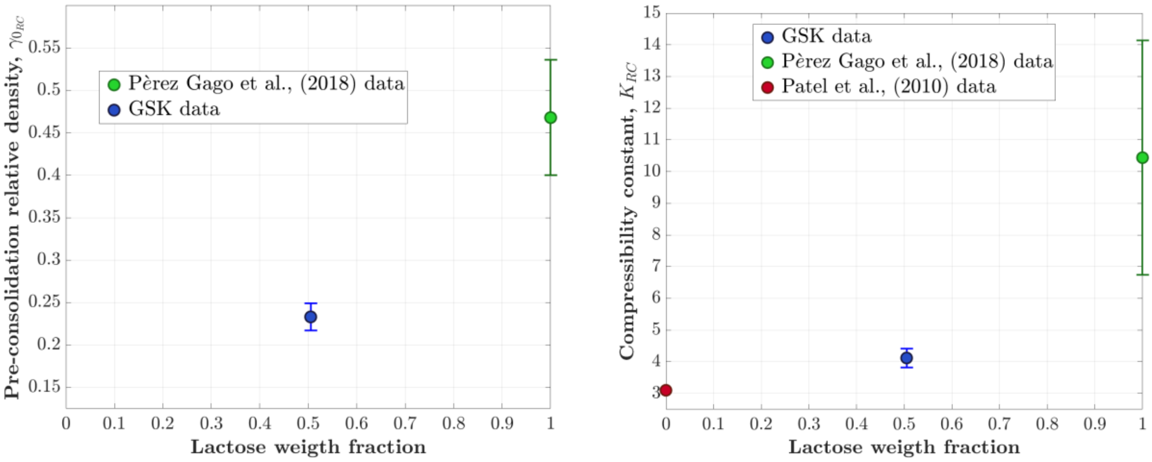

(a) (b)

Figure 4.18. *Effect of the blends composition, in the binary placebo formulation of MCC and mannitol, on the Johanson parameter values: (a)* $\gamma_{0_{RC}}$*, (b)* K_{RC}*.*

Powder blends characterized by elevated levels of mannitol and lactose, both of which exhibiting brittle deformation tendencies, present elevated values of $\gamma_{0_{RC}}$ and K_{RC}. Conversely, a higher content of MCC, which is characterised by its plastic behaviour, results in lower values of the Johnson model parameters. The observed trend indicates that as the MCC concentration of a blend increases, the estimated pressure required to produce the same ribbon SF decreases in comparison to blends with elevated levels of mannitol or lactose. The difference depends on the different compression profiles given by $\gamma_{0_{RC}}$ and K_{RC}, where a lower value of K_{RC} results in a steeper curve.

Furthermore, Figures 4.17 and 4.18 indicate that the relations between the values of $\gamma_{0_{RC}}$ and K_{RC} and the excipient weight fractions are not linear. Indeed, up to 50% MCC compositions, the values of both Johanson model parameters maintain a degree of proximity between powder blends. However, as MCC concentrations decrease further, there is a significant increase in the values of $\gamma_{0_{RC}}$ and K_{RC}.

Conclusions

The objective of this thesis was to provide a methodology able to explain and relate the discrepancies between the empirical results obtained from a compactor simulator and a roller compactor. The method ought to determine a correlation between the different pressures observed across the two pieces of equipment, for the same values of ribbon solid fraction. This methodology would enable gathering all necessary information required for the properly set the RC operating conditions, based solely on the CS experimental data. Consequently, significant material and cost savings can be achieved during the drug development process.

In order to reach these targets, the study has been carried out as follows.

First, the roll compaction process was modelled using Johanson (1965) model. The calibration of the Johanson model parameters was carried out for each material utilised in this study, based on the available experimental results. The parameter estimation was conducted by employing a maximum likelihood estimation approach. RC compression profiles were defined using the two Johanson model parameters. In a similar manner, the CS compression profiles were also established. Second, a transfer methodology was developed to account for the differences between CS and RC compression profiles. This methodology is based on the mass correction factor f_0 theory (Bi et al., 2014). Based on the obtained findings, an algebraic material-independent relationship between f_0 and the roller pressure was developed. The values of the two coefficients in this relationship were determined through a calibration procedure utilising experimental data obtained from four different placebo powder formulations. The model was subsequently validated by employing two active powder compounds, resulting in very accurate property predictions. Third, the model was validated using CS datasets acquired with punches of different sizes than the calibration data. The validation findings once again shown a high level of accuracy in terms of prediction. This section of the study demonstrates the applicability of the methodology in emergency scenarios, utilising data obtained from multiple experimental campaigns. Fourth, all the six materials were used to calibrate a final model, with the aim to be implemented in the operational stage to reduce materials consumption during drug developing phases. In conclusion, the analysis of a seventh material was conducted employing the transfer methodology. In this specific case, the predicted outcomes are deemed unsatisfactory. However, this may be due to the difference modality and equipment employed to gather the CS experimental data compared to calibration.

One of the primary challenges encountered in this Thesis was related to the definition and coding of the parameter estimate algorithm for the Johanson model. The latter was executed using an iterative optimisation process in Matlab®. Later, the optimal methodology for linking

RC and CS experimental data had to be determined. The most effective technique has been identified in the mass correction factor theory, which is also supported by physical concepts. Some issues have been identified during the analysis of the RC dataset of material, whereby the significant variability of the experimental data has resulted in a considerable level of uncertainty in the analysis.

The validation analysis focused both on the analysis of the predictive results in terms of both the ribbon solid fraction and the machine parameters. In both instances, the errors observed between the estimated and experimental values were found to be limited and uniformly distributed around zero. All errors relative to the predicted ribbon solid fraction were determined to be within the maximum threshold of relative error, which was set at 10%. Given the composition of the four placebo formulations, an analysis of the effect of excipient concentrations on Johanson parameter values was performed. The study revealed that large amounts of anhydrous lactose and mannitol, both characterised as brittle materials, lead to great values of them. Conversely, the higher the microcrystalline cellulose composition, the lower the Johanson parameter values.

One of the limits of the study is related to the fact that the proposed transfer methodology has been formulated as material independent. The values of parameters of the f_0 expression are determined by obtaining the best simultaneous transfer for all the calibration material. The effectiveness of this approach was shown to be significant across all six materials examined, exceeding the typical number of materials analysed in existing literature. This finding is noteworthy considering the significant variations in the compositions and characteristics of the powder mixtures. Nevertheless, it is important to note that the methodology employed in this work may not yield desirable results when applied to materials that exhibit a significantly distinct physical response across the two scales.

Hence, a potential opportunity to improve the proposed transfer method in the future would involve examining materials with physical compositions and properties beyond the six powder blends evaluated. Such an approach would enable the determination of the overall effectiveness of the proposed methodology. The execution of this implementation should follow the same procedure as the collection of the calibration experimental data, in order to avoid introducing additional variability caused by using different equipment or applying pressure in different modes. When investigate materials comparable to those discussed in this Thesis, it is suggested to proceed with the implementation of the methodology during the usage phase. This involves exclusively establishing the RC machine parameters based on the CS experimental results and the mass correction factor.

Nomenclature

Symbols (latin letters)

SRF = Specific roll force
D = Roll diameter
S = Roll gap
RS = Roll speed
K = Compressibility constant
R = Roll radius
V_{α} = Specific volume of the layer corresponding to the angular position θ
V_{θ} = Specific volume of the layer corresponding to the nip angle α
ΔL = Arc-length segment
W = Roll width
P_{max} = Maximum roller surface pressure at the minimum roll gap
R_f = Total roll force
F = Force factor
K_{RC} = Compressibility constant estimated from roller compactor experimental data
K_{CS} = Compressibility constant estimated from compactor simulator experimental data
$\widetilde{K}_{RC}$ = Compressibility constant estimated using the mass correction factor transfer methodology
f_{θ} = fraction of material delivered to angle θ
f_0 = Fraction of material delivered to angle $\theta = 0$
P_{CS} = Maximum pressure applied by the compactor simulator
$\mathcal{L}$ = Likelihood function
ℓ = Log-likelihood function
$\mathbf{H}$ = Hessian matrix

Greek letters

θ = Angular roll position
α = Nip angle
γ = Solid fraction

ρ_E = Envelope density
ρ_T = True density
ε = Porosity
ω = Roll rotation frequency
δ_E = Effective angle of internal friction
ϕ_W = Angle of wall friction
ν = Acute angle between major principal axis and tangent to roll surface
μ = Friction coefficient
σ_α = Mean normal stress at nip angle α
σ_θ = Mean normal stress at angular position θ
ρ_α = Powder density in the layer corresponding to the angular position θ
ρ_θ = Powder density in the layer corresponding to the nip angle
γ_R = Ribbon solid fraction
γ_0 = Pre-consolidation relative density
$\gamma_{0_{\mathrm{RC}}}$ = Pre-consolidation relative density estimated from roller compactor experimental data
$\gamma_{0_{\mathrm{CS}}}$ = Pre-consolidation relative density estimated from compactor simulator experimental data
$\tilde{\gamma}_{0_{RC}}$ = Pre-consolidation relative density estimated using the mass correction factor transfer methodology
$\sigma_{intra-run}$ = Standard deviation of the measured solid fraction of the intra runs samples

Acronyms

RC = Roller compactor
CS = Compactor simulator
SF = Solid fraction
API = Active pharmaceutical ingredient
FEM = Finite element methods
DEM = Discrete element methods
MCC = Microcrystalline cellulose
SD = Spray dried
MgSt = Magnesium stearate
SEM = Scanning electron microscope
MLE = Maximum likelihood estimation
SE = Standard error
MRE = Mean relative error
MAE = Mean absolute error

Appendix

A.1 Roller compactor datasets

Table A.1.1. *RC experimental dataset of Formulation 1.*

Material	Dataset ID	Run no.	Specific roll force [kN/cm]	Roll gap [mm]	Solid fraction [-]
Formulation 1	RC-F1	1	3.0	2	0.652 0.653 0.668
		2	6.0	2	0.685 0.753 0.749
		3	9.0	2	0.817 0.798 0.792
		4	12.0	2	0.802 0.848 0.824
		5	4.2	4	0.670 0.676 0.665

Table A.1.2. *RC experimental dataset of Formulation 2.*

Material	Dataset ID	Run no.	Specific roll force [kN/cm]	Roll gap [mm]	Solid fraction [-]
Formulation 2	RC-F2	1	3.0	2	0.588 0.606 0.582
		2	6.0	2	0.716 0.715 0.715
		3	9.0	2	0.759 0.822 0.778
		4	12.0	2	0.807 0.820 0.840
		5	4.2	4	0.577

					0.622 0.610
		6	8.5	4	0.746 0.725 0.693
		7	3	4	0.569 0.594 0.574
		8	6	4	0.653 0.655 0.679

Table A.1.3. *RC experimental dataset of Formulation 3.*

Material	Dataset ID	Run no.	Specific roll force [kN/cm]	Roll gap [mm]	Solid fraction [-]
Formulation 3	RC-F3	1	3.0	2	0.564 0.566 0.564
		2	6.0	2	0.661 0.701 0.669
		3	9.0	2	0.753 0.734 0.748
		4	12.0	2	0.856 0.852 0.827
		5	4.2	4	0.556 0.559 0.555
		6	8.5	4	0.721 0.718 0.719
		7	3	4	0.527 0.523 0.524
		8	6	4	0.646 0.624 0.647

Table A.1.4. *RC experimental dataset of Formulation 4.*

Material	**Dataset ID**	**Run no.**	**Specific roll force [kN/cm]**	**Roll gap [mm]**	**Solid fraction [-]**
Formulation 4	RC-F4	1	3.0	2	0.559 0.572 0.587
		2	6.0	2	0.680 0.672 0.672
		3	9.0	2	0.738 0.737 0.753
		4	12.0	2	0.794 0.752 0.811
		5	4.2	4	0.545 0.558 0.566
		6	8.5	4	0.680 0.698 0.689
		7	3.0	4	0.515 0.526 0.515
		8	6.0	4	0.630 0.632 0.607

Table A.1.5. *RC experimental dataset of Compound A.*

Material	**Dataset ID**	**Run no.**	**Specific roll force [kN/cm]**	**Roll gap [mm]**	**Solid fraction [-]**
Compound A	RC-CA	1	4.0	2	0.632 0.647 0.626
		2	6.0	2	0.703 0.660 0.690
		3	8.0	2	0.750 0.760 0.750
		4	4.0	2	0.660 0.640 0.640
		5	6.0	2	0.710 0.695 0.693

6	8.0	2	0.748
			0.762
			0.791
7	8.0	2	0.729
			0.738
			0.722
8	8.0	2	0.764
			0.733
			0.726
9	8.0	2	0.731
			0.745
			0.727
10	6.0	2	0.690
			0.702
			0.693
11	6.0	2	0.720
			0.708
			0.736
12	6.0	2	0.715
			0.716
			0.708
13	6.0	2	0.708
			0.709
			0.714
14	6.0	2	0.701
			0.681
			0.687
15	6.0	2	0.716
			0.667
			0.693
16	6.0	2	0.678
			0.676
			0.686
17	8.0	2	0.717
			0.719
			0.721
18	8.0	2	0.715
			0.733
			0.734
19	8.0	2	0.737
			0.739
			0.729
20	5.0	3	0.641
			0.641
			0.638
21	7.5	3	0.720
			0.715
			0.704
22	10.0	3	0.780
			0.735
			0.784

		23	14.5	3	0.818 0.785 0.782
		24	6.0	2	0.658 0.667 0.685
		25	5.0	3	0.661 0.660 0.650
		26	7.5	3	0.723 0.711 0.726
		27	10.0	3	0.786 0.787 0.762
		28	14.5	3	0.846 0.826 0.826
		29	6.0	2	0.712 0.706 0.715

Table A.1.6. *RC experimental dataset of Compound B.*

Material	**Dataset ID**	**Run no.**	**Specific roll force [kN/cm]**	**Roll gap [mm]**	**Solid fraction [-]**
Compound B	RC-CB	1	5.5	2	0.703 0.664 0.671
		2	5.5	2	0.668 0.686 0.713
		3	3.5	2	0.678 0.656 0.708
		4	10.0	2	0.722 0.783 0.789
		5	6.5	3	0.692 0.716 0.723
		6	5.5	2	0.741 0.748 0.715
		7	5.5	2	0.761 0.718 0.693
		8	5.5	2	0.718

			0.701
			0.699
9	5.5	2	0.697
			0.675
			0.744
10	5.5	2	0.722
			0.700
			0.718

Table A.1.7. *RC experimental dataset of Compound C.*

Material	Dataset ID	Specific roll force [kN/cm]	Roll gap [mm]	Solid fraction [-]
Compound C	RC-CC	2.0	2	0.704
		3.0	2	0.737
		4.0	2	0.783
		1.5	2	0.686
		1.0	2	0.655
		2.0	2	0.730
		2.5	2	0.739
		3.0	2	0.689
		2.0	2	0.768
		3.0	2	0.731
		4.5	2	0.788
		3.5	2	0.789
		2.5	2	0.742
		1.5	2	0.676
		3.8	2	0.780
		3.5	2	0.764
		4.0	2	0.849
		3.8	2	0.824
		4.5	3	0.755
		3.8	2	0.763
		4.5	2	0.859
		4.5	2	0.854
		4.5	2	0.824

A.2 Compactor simulator datasets

Table A.2.1. *10 mm Phoenix® CS experimental dataset with of Formulation 1.*

Material	Dataset ID	Pressure [MPa]	Solid fraction [-]
Formulation 1	**CS10-F1**	19.722	0.617
		18.296	0.609
		17.685	0.608
		18.615	0.613
		17.736	0.610
		33.868	0.678
		30.660	0.668
		34.034	0.682
		34.759	0.681
		34.874	0.684
		49.249	0.728
		45.773	0.712
		45.060	0.713
		47.619	0.713
		48.982	0.722
		82.722	0.771
		87.713	0.776
		93.328	0.791
		89.407	0.764
		83.053	0.783
		106.952	0.803
		106.774	0.807
		98.205	0.768
		111.981	0.783
		102.840	0.790
		137.026	0.822
		138.465	0.827
		138.898	0.805
		137.866	0.814
		140.897	0.827
		168.501	0.836
		169.417	0.857
		166.909	0.839
		164.999	0.829
		159.270	0.846
		189.598	0.817
		188.007	0.833
		186.530	0.830
		187.153	0.821
		192.628	0.856

Table A.2.2. *10 mm Phoenix® CS experimental dataset with of Formulation 2.*

Material	Dataset ID	Pressure [MPa]	Solid fraction [-]
Formulation 2	**CS10-F2**	22.536	0.584
		22.536	0.592
		23.720	0.599
		23.708	0.590
		23.568	0.600
		41.113	0.672
		42.119	0.680
		40.336	0.672
		42.972	0.675
		42.679	0.672
		65.381	0.724
		67.533	0.735
		68.742	0.737
		66.158	0.716
		66.323	0.742
		91.317	0.775
		100.331	0.766
		99.886	0.777
		98.943	0.799
		99.274	0.789
		135.027	0.813
		146.155	0.837
		142.463	0.827
		142.896	0.817
		132.328	0.781
		166.476	0.836
		176.293	0.855
		175.656	0.859
		164.426	0.828
		178.508	0.837
		210.785	0.860
		214.566	0.852
		215.789	0.879
		219.850	0.896
		211.243	0.854

Table A.2.3. *10 mm Phoenix® CS experimental dataset with of Formulation 3.*

Material	Dataset ID	Pressure [MPa]	Solid fraction [-]
Formulation 3	CS10-F3	22.384	0.558
		23.135	0.567
		23.504	0.565
		23.542	0.566
		23.351	0.566
		52.903	0.701
		54.444	0.695
		53.947	0.699
		53.196	0.700
		54.011	0.692
		68.488	0.725
		70.346	0.728
		69.774	0.737
		69.188	0.730
		67.431	0.741
		95.544	0.765
		99.440	0.780
		98.536	0.781
		100.675	0.781
		101.044	0.785
		151.172	0.832
		153.171	0.836
		152.878	0.833
		157.627	0.844
		157.334	0.838
		188.516	0.865
		186.046	0.855
		198.944	0.869
		191.623	0.857
		195.570	0.861
		43.074	0.671
		43.188	0.672
		43.303	0.668
		42.004	0.661
		42.437	0.657

Table A.2.4. *10 mm Phoenix® CS experimental dataset with of Formulation 4.*

Material	Dataset ID	Pressure [MPa]	Solid fraction [-]
Formulation 4	CS10-F4	23.797	0.566
		25.057	0.580
		24.408	0.578
		23.644	0.569
		23.415	0.573
		40.222	0.653
		40.374	0.655
		39.687	0.648
		40.018	0.653
		38.757	0.620
		49.580	0.675
		51.528	0.691
		48.943	0.683
		48.510	0.684
		51.286	0.693
		68.347	0.730
		69.748	0.728
		67.354	0.730
		69.481	0.726
		67.189	0.728
		102.483	0.774
		95.671	0.773
		103.005	0.777
		98.001	0.770
		98.714	0.765
		144.271	0.794
		154.864	0.819
		154.266	0.835
		154.571	0.832
		153.693	0.822
		178.317	0.839
		193.023	0.848
		184.123	0.828
		189.929	0.846
		190.693	0.854

Table A.2.5. *10 mm Phoenix® CS experimental dataset with of Compound A.*

Material	Dataset ID	Pressure [MPa]	Solid fraction [-]
Compound A	CS10-CA	17.723	0.572
		20.270	0.585
		15.444	0.554
		18.615	0.584
		18.908	0.580
		40.222	0.665
		41.482	0.657
		48.765	0.683
		44.283	0.684
		50.840	0.707
		64.846	0.733
		60.835	0.721
		58.964	0.719
		74.625	0.741
		66.094	0.740
		82.875	0.753
		75.478	0.737
		77.910	0.751
		81.360	0.755
		89.560	0.762
		91.584	0.765
		108.060	0.771
		104.724	0.768
		101.006	0.788
		98.982	0.777
		145.111	0.814
		142.335	0.811
		143.087	0.820
		162.656	0.815
		148.587	0.810

Table A.2.6. *10 mm Phoenix® CS experimental dataset with of Compound B.*

Material	**Dataset ID**	**Pressure [MPa]**	**Solid fraction [-]**
Compound B	CS10-CB	27.999	0.628
		29.807	0.623
		30.927	0.629
		32.557	0.623
		31.984	0.627
		63.331	0.735
		57.716	0.733
		64.464	0.725
		61.434	0.741
		67.354	0.743
		81.194	0.758
		92.514	0.779
		92.577	0.763
		87.892	0.762
		91.406	0.762
		119.277	0.814
		115.597	0.815
		129.807	0.815
		112.898	0.795
		109.282	0.802
		153.056	0.838
		126.191	0.823
		121.684	0.813
		124.014	0.818
		132.773	0.832
		173.772	0.843
		166.132	0.845
		162.402	0.838
		164.273	0.858
		188.070	0.857
		225.083	0.867
		249.504	0.866
		244.309	0.866
		228.865	0.864
		206.876	0.864
		52.979	0.724
		52.496	0.716
		46.359	0.682
		49.542	0.692
		51.859	0.721

Table A.2.7. *18 mm Phoenix® CS experimental dataset with of Formulation 2.*

Material	Dataset ID	Pressure [MPa]	Solid fraction [-]
Formulation 2	CS18-F2	18.983	0.586
		18.922	0.586
		20.331	0.594
		19.173	0.587
		18.564	0.584
		115.662	0.824
		116.515	0.828
		122.734	0.828
		112.580	0.830
		116.097	0.833

Table A.2.8. *18 mm Phoenix® CS experimental dataset with of Formulation 3.*

Material	Dataset ID	Pressure [MPa]	Solid fraction [-]
Formulation 3	CS18-F3	23.191	0.565
		21.413	0.559
		21.227	0.558
		22.694	0.561
		18.855	0.543
		22.011	0.563
		20.678	0.552
		22.034	0.562
		19.346	0.554
		20.026	0.552
		47.605	0.684
		54.343	0.687
		54.001	0.690
		54.018	0.693
		48.813	0.686
		143.112	0.844
		145.084	0.852
		142.074	0.836
		139.707	0.850
		145.650	0.840
		128.507	0.837
		122.333	0.835
		140.774	0.850
		131.690	0.845
		133.615	0.844

Table A.2.9. *18 mm Phoenix® CS experimental dataset with of Formulation 4.*

Material	Dataset ID	Pressure [MPa]	Solid fraction [-]
Formulation 4	CS18-F4	21.276	0.575
		20.853	0.565
		20.942	0.570
		20.667	0.568
		19.804	0.562
		19.429	0.561
		20.258	0.569
		18.376	0.565
		21.077	0.567
		19.918	0.566
		44.831	0.675
		40.386	0.675
		40.451	0.671
		38.963	0.669
		38.751	0.666
		111.623	0.790
		112.420	0.787
		108.854	0.788
		108.801	0.781
		105.765	0.776
		106.952	0.779
		117.421	0.791
		109.951	0.792
		107.640	0.782
		110.929	0.789

Table A.2.10. *21.85 mm Phoenix® CS experimental dataset with of Compound A.*

Material	Dataset ID	Pressure [MPa]	Solid fraction [-]
Compound A	CS21-CA	26.061	0.647
		27.074	0.645
		31.013	0.662
		30.397	0.647
		27.208	0.649
		25.752	0.634
		28.245	0.643
		29.360	0.649
		30.912	0.641
		30.619	0.650
		31.685	0.646
		30.432	0.642
		31.677	0.636
		31.893	0.634
		33.232	0.658
		25.080	0.633
		30.301	0.646
		26.216	0.639
		30.965	0.650
		27.464	0.643
		29.349	0.643
		25.194	0.623
		30.131	0.646
		31.163	0.643
		32.710	0.650
		34.915	0.658
		35.123	0.657
		65.040	0.748
		56.040	0.731
		67.670	0.748
		61.101	0.743
		63.163	0.753
		62.854	0.748
		63.915	0.745

Table A.2.11. *21.85 mm Phoenix® CS experimental dataset with of Compound B.*

Material	Dataset ID	Pressure [MPa]	Solid fraction [-]
Compound B	CS21-CB	45.428	0.696
		37.337	0.671
		41.692	0.669
		49.180	0.700
		43.009	0.685
		40.678	0.681
		42.249	0.683
		49.375	0.704
		43.118	0.688
		44.031	0.691
		36.385	0.669
		41.228	0.673
		37.483	0.677
		36.603	0.654
		40.998	0.670
		36.654	0.641
		34.560	0.639
		42.908	0.670
		37.427	0.660
		42.150	0.665
		41.924	0.670
		38.310	0.660
		45.591	0.667
		57.584	0.709
		67.385	0.725
		48.218	0.682
		47.727	0.674
		44.423	0.679
		41.382	0.680
		38.443	0.657
		42.734	0.671
		42.937	0.669
		48.796	0.673
		47.164	0.682
		44.695	0.678
		39.179	0.673
		47.295	0.691
		41.540	0.655

Table A.2.12. *11.28 mm Styl'One® CS experimental dataset with of Compound C.*

Material	Dataset ID	Pressure [MPa]	Solid fraction [-]
Compound C	CS11-CC	28.934	0.735
		29.435	0.737
		29.234	0.735
		48.657	0.791
		48.757	0.788
		48.958	0.793
		68.481	0.828
		68.581	0.825
		68.481	0.825
		92.809	0.863
		93.510	0.864
		93.010	0.862
		117.138	0.895
		117.338	0.893
		117.539	0.895
		136.861	0.908
		136.861	0.908
		136.361	0.905
		174.005	0.909
		175.607	0.928
		175.106	0.932
		29.435	0.740
		29.435	0.737
		29.335	0.736
		48.757	0.790
		48.958	0.787
		48.657	0.789
		68.881	0.827
		68.481	0.827
		68.481	0.824
		93.210	0.863
		93.010	0.858
		93.010	0.858
		116.938	0.893
		117.438	0.890
		117.539	0.892
		137.362	0.906
		136.461	0.907
		136.561	0.907
		174.806	0.925
		174.606	0.926
		175.006	0.931
		28.367	0.737

47.489	0.793
55.365	0.811
78.326	0.853
101.620	0.878
120.041	0.895
157.119	0.917
28.934	0.735
48.290	0.794
58.035	0.816
81.997	0.862
106.125	0.892
125.248	0.910
163.493	0.938
29.001	0.740
48.424	0.790
58.135	0.813
83.031	0.860
106.092	0.891
124.814	0.910
163.292	0.937
29.635	0.752
49.792	0.808
69.115	0.844
93.343	0.874
118.306	0.898
137.529	0.921
176.341	0.938
29.635	0.743
49.392	0.803
69.081	0.841
93.443	0.876
117.639	0.898
136.995	0.912
175.707	0.936
29.435	0.741
48.991	0.800
68.547	0.839
93.277	0.872
117.906	0.898
137.662	0.921
175.006	0.939
30.269	0.788
49.992	0.827
69.015	0.854
93.477	0.884
117.205	0.905

136.494	0.920
174.673	0.940
29.435	0.743
49.024	0.798
68.581	0.841
93.377	0.873
117.872	0.896
137.162	0.917
175.240	0.938
30.302	0.782
49.959	0.823
69.048	0.854
93.544	0.885
117.906	0.907
137.028	0.917
174.673	0.937

References

Amini, H. and Akseli, I. 2020. A first principle model for simulating the ribbon solid fraction during pharmaceutical roller compaction process. *Powder Technol*. **368**, pp.32–44.

Bano, G., Dhenge, R.M., Diab, S., Goodwin, D.J., Gorringe, L., Ahmed, M., Elkes, R. and Zomer, S. 2022. Streamlining the development of an industrial dry granulation process for an immediate release tablet with systems modelling. *Chem. Eng. Res. Des.* **178**, pp.421–437.

Bi, M., Alvarez-Nunez, F. and Alvarez, F. 2014. Evaluating and modifying Johanson's rolling model to improve its predictability. *J. Pharm. Sci.* **103**(7), pp.2062–2071.

Bindhumadhavan, G., Seville, J.P.K., Adams, M.J., Greenwood, R.W. and Fitzpatrick, S. 2005. Roll compaction of a pharmaceutical excipient: Experimental validation of rolling theory for granular solids. *Chem. Eng. Sci.* **60**(14), pp.3891–3897.

Cantor, S.L., Augsburger, L.L., Hoag, S.W. and Gerhardt, A. 2008. Pharmaceutical granulation processes, mechanism, and the use of binders *in*: *Pharmaceutical Dosage Forms: Tablets*. Informa London, pp.261–302.

Davies P 2009. Oral Solid Dosage Forms *In*: M. Gibson, ed. *Pharmaceutical Preformulation and Formulation*. CRC Press, pp.367–430.

Farber, L., Hapgood, K.P., Michaels, J.N., Fu, X.Y., Meyer, R., Johnson, M.A. and Li, F. 2008. Unified compaction curve model for tensile strength of tablets made by roller compaction and direct compression. *Int. J. Pharm*. **346**(1–2), pp.17–24.

Greene, W.H. 2012. *Econometric analysis* 7th ed. UpperSaddle River, NJ 07458, US: Prentice Hall.

Guo, Y., Wu, C.-Y. and Thornton, C. 2010. The effects of air and particle density difference on segregation of powder mixtures during die filling. *Chem. Eng. Sci*. **66**(4), pp.661–673.

Inghelbrecht, S. and Remon, J.P. 1998. Reducing dust and improving granule and tablet quality in the roller compaction process. *Int. J. Pharm*. **171**(2), pp.195–206.

Johanson, J.R. 1965. A Rolling Theory for Granular Solids. *J. Appl. Mech.* **32**(4), pp.842–848.

Keizer, H. Lou 2021. *Hybrid Modelling of Roll Compaction*. PhD thesis, Hamburg: Heinrich-Heine-Universität Düsseldorf.

Kleinebudde, P. 2004. Roll compaction/dry granulation: pharmaceutical applications. *Eur. J. Pharm. Biopharm*. **58**(2), pp.317–326.

Leuenberger, H. 1982. The compressibility and compactibility of powder systems. *Int. J. Pharm*. **12**(1), pp.41–55.

Liu, Y. and Wassgren, C. 2016. Modifications to Johanson's roll compaction model for improved relative density predictions. *Powder Technol.* **297**, pp.294–302.

Mansa, R.F. 2006. *Roller compaction of pharmaceutical excipients and prediction using intelligent software*. PhD thesis, Birmingham: University of Birmingham.

Mazel, V., Busignies, V., Diarra, H. and Tchoreloff, P. 2015. Lamination of pharmaceutical tablets due to air entrapment: Direct visualization and influence of the compact thickness. *Int. J. Pharm*. **478**(2), pp.702–704.

Miguélez-Morán, A.M., Wu, C.Y. and Seville, J.P.K. 2008. The effect of lubrication on density distributions of roller compacted ribbons. *Int. J. Pharm*. **362**(1–2), pp.52–59.

Moroney, K.M., Cronin, P., Adeleye, O.A., Schaller, B.E., Howard, M.A., Castro-Dominguez, B., Ramachandran, R. and Walker, G.M. 2020. An evaluation of the Johanson model for roller compaction process development for a high dose API. *Powder Technol.* **366**, pp.82–95.

Nagy, Z.K. and El Hagrasy, A. 2020. *Continuous pharmaceutical processing* (J. Litster, ed.). Cham, Switzerland: Springer.

Parikh, D.M. 2005. *Handbook of Pharmaceutical Granulation Technology* 2nd ed. 6000 Broken Sound Parkway NW, Suite 300: Taylor & Francis Group.

Pérez Gago, A., Reynolds, G. and Kleinebudde, P. 2018. Impact of roll compactor scale on ribbon density. *Powder Technol.* **337**, pp.92–103.

Perez-Gandarillas, L. 2016. *Dry granulation process and compaction behavior of granulated powders*. PhD thesis, Ecole des Mines d'Albi-Carmaux.

Pietsch, W.B. 2002. *Agglomeration Processes: Phenomena, Technologies, Equipment* 1st ed. Wiley-VCH.

Reimer, H.L. and Kleinebudde, P. 2019. Hybrid modeling of roll compaction processes with the Styl'One Evolution. *Powder Technol*. **341**, pp.66–74.

Reynolds, G., Ingale, R., Roberts, R., Kothari, S. and Gururajan, B. 2010. Practical application of roller compaction process modeling. *Comput. Chem. Eng.* **34**(7), pp.1049–1057.

Rowe, R.C., Sheskey, P. and Quinn, M. 2009. *Handbook of pharmaceutical excipients* 6th ed. Washington DC, US: Pharmaceutical Press and American Pharmacists Association.

Ruud, P.A. 2000. *An introduction to classical econometric theory*. Oxford, UK: Oxford University Press.

Salman, A.D., Hounslow, M. and Seville, J.P.K. 2006. *Granulation* 1st ed. Amsterdam, The Netherlands: Elsevier Science.

Schiano, S., Chen, L. and Wu, C.Y. 2018. The effect of dry granulation on flow behaviour of pharmaceutical powders during die filling. *Powder TechnoL.*. **337**, pp.78–83.

Shanmugam, S. 2015. Granulation techniques and technologies: recent progresses. *BioImpacts*. **5**(1), pp.55–63.

So, C., Leung, L.Y., Muliadi, A.R., Narang, A.S. and Mao, C. 2021. Simplifying Johanson's roller compaction model to build a "Virtual Roller Compactor" as a predictive tool – Theory and practical application. *Int. J. Pharm.* **601**.

Szappanos-Csordas, K. 2018. *Impact of material properties, process parameters and roll compactor design on roll compaction*. PhD thesis, Düsseldorf: Heinrich-Heine-Universität Düsseldorf.

Teng, Y., Qiu, Z. and Wen, H. 2009. Systematical approach of formulation and process development using roller compaction. *Eur. J. Pharm. Biopharm.* **73**(2), pp.219–229.

Thapa, P., Tripathi, J. and Jeong, S.H. 2019. Recent trends and future perspective of pharmaceutical wet granulation for better process understanding and product development. *Powder Technol.* **344**, pp.864–882.

Toson, P., Lopes, D.G., Paus, R., Kumar, A., Geens, J., Stibale, S., Quodbach, J., Kleinebudde, P., Hsiao, W.K. and Khinast, J. 2019. Model-based approach to the design of pharmaceutical roller-compaction processes. *Int. J. Pharm. X.* **1**.

Yu, S. 2013. *Roll compaction of pharmaceutical excipients*. PhD thesis, Birmingham: University of Birmingham.

Zinchuk, A. V, Mullarney, M.P. and Hancock, B.C. 2004. Simulation of roller compaction using a laboratory scale compaction simulator. *Int. J. Pharm.* **269**(2), pp.403–415.